



**Synthesis and Characterisation
of B-TiO₂ Thin Films by
Atmospheric Pressure Chemical
Vapour Deposition and Plasma
Enhanced Chemical Vapour
Deposition: Functional Films for
Different Substrates.**

This thesis is submitted in partial fulfilment of the requirements for the
Degree of Doctor of Philosophy (Chemistry and Material Science)

Miguel Quesada-Gonzalez

Supervised by Prof. I. P. Parkin and Prof. C. J. Carmalt

University College London
Chemistry Department
Christopher Ingold Laboratories,
20 Gordon Street,
WC1H 0AJ

2018

I, Miguel Quesada-Gonzalez, confirm that the work presented in this thesis is my own. Where information has been derived from other sources, I confirm that this has been indicated in the thesis.

Abstract

Anatase, a form of titanium dioxide (TiO_2), is arguably the most studied wide band gap semiconducting photocatalyst. TiO_2 has many other applications, including water and air purification, self-cleaning surfaces and photovoltaic. However, for many applications, as well as for safety concerns related to the handling of nanoparticles, the simultaneous synthesis and deposition of photocatalytic TiO_2 thin films is highly desirable.

Numerous routes towards the simultaneous synthesis and deposition of anatase TiO_2 thin films have already been reported. Chemical vapour deposition (CVD) methods have successfully been implemented for the industrial production of photocatalytic TiO_2 thin films.

Nevertheless, the rather high temperature required in CVD does not allow the coating of heat sensitive substrates. Similarly, other photocatalytic TiO_2 deposition processes all possess significant drawbacks, such as the low-pressure environment required by physical vapour deposition (PVD) and the post-heating treatment or the large number of steps required by sol-gel approaches. In addition, most of the methods remain difficult to implement on complex shape substrates and/or non-conformal. The following research thesis reports on new functional coatings, based on boron-doped TiO_2 , which were deposited by APCVD and AP-PECVD on different matrices and substrates.

Boron, as a dopant for TiO_2 systems, has been used and reported to enhanced TiO_2 photocatalytic performance under UV light, as well as numerous scientific papers reported on the visible light response of boron-doped TiO_2 . However, in most of the cases the successful B- TiO_2 was synthesised in the form of powders, not thin films. Also, when B- TiO_2 thin films were synthesised, only substitutional boron-doped TiO_2 was previously reported, whereas, the higher stability and long-term life of interstitial boron vs substitutional has been proven and reported theoretically and experimentally.

The present thesis presents, to the best of our knowledge, for the first time, the synthesis of interstitial B-TiO₂ thin films, which, as synthesised by different techniques, were successfully deposited on thermo-sensitive substrates.

Acknowledgements

Firstly, I would like to thank my supervisors, Prof. I. P. Parkin and Prof. Claire J. Carmalt, for all their encouragement, support and guidance through my PhD.

Also, thanks go to Dr Nicolas D. Boscher for the long discussions, mentoring and advices while performing my research at LIST in Luxembourg.

I would like to make special thanks to Dr Carlos Sotelo-Vazquez, Dr Andreas Kafizas and Dr Raúl Quesada-Cabrera for the endless discussions and sharing all their knowledge and experience with me. Thank you to Dr Robert Palgrave and Dr Steven Firth for training and assistance to the SEM, Raman and XPS instruments.

Than you to Dr Kamal Baba, for all the support and training provided during my time in Luxembourg.

I would like to make also a special mention to Dr Caroline Knapp, for all the useful discussions which kept me going forward in many occasions.

A personal mention to all of my colleagues from both institutions, UCL and LIST, thank you for all of those reenergising coffee breaks, useful discussions and the companionship: Francesco, Nadia, Sacha, Valerie, Joe, Tom, Haphi, Diana, Paula, Nidal, Veneranda, Olivier, Dominique, Ula, Francois, Florian, Acerina and Lluís.

Finally, but not less important, I would like to thank my parents, Miguel e Isabel, my sisters, Isabel y Raquel and dearest friends: Rosa, Estefania, Marta, Andre, and Damien. Without their love and support, I would not have been able to complete this thesis.

List of Figures

- Figure 1.1** Graphic representation of the photocatalytic activation/reaction of anatase TiO₂ thin-film on the surface.
- Figure 1.2** Scheme of the models for the TiO₂ band gap changes when nonmetal doping.
- Figure 1.3** Photo of the APCVD rig built and used for this thesis.
- Figure 1.4** Classification of atmospheric plasmas.
- Figure 1.5** Schematic for the design of an APPJ reactor.
- Figure 1.6** Classification of atmospheric plasmas (scheme).
- Figure 1.7** Simplified scheme of the design of a semi-metallic MW torch.
- Figure 1.8** Photo of the MW AP-PECVD reactor employed for the synthesis of thin films in this thesis.
- Scheme 2.1** Schematic of the APCVD apparatus used to synthesize undoped and B-TiO₂ thin films.
- Figure 2.1** FTIR spectra of the B-TiO₂ sample coated with stearic acid upon UVA illumination (1.2 mW cm⁻²) on the B-TiO₂ film.
- Table 2.1** Table of experimental parameters for the films deposition by APCVD.
- Figure 2.2** Photo of pieces of all thin films synthesised by APCVD: (a) undoped TiO₂ and B-TiO₂; (b) sample A; (c) sample B and (d) sample C.
- Table 2.2** Microstrain (LY) calculated by Le Bail fitting (GSAS software), extracted from the XRD raw data of undoped and boron-doped samples.
- Figure 2.3** XRD patterns of B-TiO₂ thin films and an undoped TiO₂ sample (A = anatase and R = rutile); (b) Raman spectra of the B-TiO₂ samples, compared to the undoped anatase film and (c) Raman shift of the E_g band zoomed.
- Figure 2.4** (a) X-ray diffraction pattern of the powdery section in sample B-TiO₂ (C); (b) photograph of sample B-TiO₂ (C) with powdery deposition on top; (c) Photograph of sample B-TiO₂ (C) without powdery deposition on top.

- Table 2.3** Cell parameters and boron atomic concentration of the undoped and B-TiO₂ thin films in comparison to powder standards of anatase and rutile.
- Figure 2.5** Ti 2p environment surface XPS spectra of boron-doped TiO₂ thin films: (a) sample A, (b) Sample B and (c) sample C.
- Figure 2.6** B 1s XPS Surface spectra of B-TiO₂ samples: (a) B-TiO₂ (A); (b) B-TiO₂ (B) and (c) B-TiO₂ (C).
- Figure 2.7** B 1s XPS depth profiling spectra of: (a) B-TiO₂ (A); (b) B-TiO₂ (B) and (c) B-TiO₂ (C) thin films.
- Figure 2.8** In depth D-SIMS spectra: (a) sample B-TiO₂ (A); (b) sample B-TiO₂ (B); (c) B-TiO₂ (C).
- Figure 2.9** B 1s XPS spectra after the second (a) and third (b) run of the photocatalytic test with SA and cleaning of the samples, respectively.
- Figure 2.10** SEM images (top view) of: (a) Undoped TiO₂, (b) B-TiO₂ (A), (c) B-TiO₂ (B) and (d) B-TiO₂ (C).
- Figure 2.11** Cross-section SEM images of the undoped and B-TiO₂ samples: (a) undoped TiO₂; (b) B-TiO₂ (A); (c) B-TiO₂ (B); (d) B-TiO₂ (C).
- Figure 2.12** (a) Optical image with a tilt angle of the B-TiO₂ thin film on glass and (b and c) the corresponding SEM images from two different areas identified on the B-TiO₂ thin film, and (d) optical image of the undoped TiO₂ and (e) its SEM capture.
- Figure 2.13** (a) UV-visible spectra (transmittance) of the doped and undoped TiO₂ films, (b) graphical calculation (Tauc plot) of the optical band gap for all the boron-doped TiO₂ samples and (c) XPS valence band spectra of the doped samples as compared to the undoped.
- Figure 2.14** (a) Average Formal quantum efficiencies (FQE) obtained during photodegradation of stearic acid under UVA irradiation of selected B-TiO₂ films and undoped TiO₂ film, used as reference; (b) graphic representation of the evolution/relation between the B atom concentration versus the photoactivity (FQE) and average crystal size of the TiO₂ and B-TiO₂ films.
- Figure 2.15** The calculated density of states (DoS) (a) and band structure (b) of undoped anatase TiO₂.
- Figure 2.16** The transition level diagrams for B-TiO₂ under both Ti-rich/O-poor (left) and Ti-poor/O-rich (right) growth regimes.

- Table 2.4** Data extracted from the Hall Effect Electrical Measurements. (*) Data collected from reference 78.
- Figure 2.17** The partial charge densities of the charge states of V_{Ti} as viewed along the $\{010\}$ direction showing the localisation of holes (blue isosurfaces) in each example. The isosurfaces are plotted from 0 - 0.015 eV \AA^{-3} .
- Figure 2.18** The partial charge densities of B_i^0 (a), B_i^{1+} (b), B_i^{2+} (c), B_{Ti}^0 (d), B_o^0 (e) and B_o^{4-} (f) defect charge states as viewed along the $\{100\}$ direction displaying the localisation of holes and electrons (blue and orange isosurfaces respectively). The isosurfaces are plotted from 0-0.015 eV \AA^{-3} .
- Table 3.1** Experimental parameters of the AP-PECVD depositions.
- Figure 3.1** Schematic of the AP-PECVD apparatus set up for doping.
- Figure 3.2** AP-PECVD deposition on optical fibre: (a) photo of the microwave plasma reactor and PMMA optical fibre being coated, passing through the plasma; (b) simplified scheme of the plasma coating process; (c) photo of the illuminated PMMA optical fibre coated with B-TiO₂ (sample P5).
- Figure 3.3** Raman analysis of the samples deposited on Si wafers: (a) compilation of Raman spectra of boron-doped samples (P2, P3, and P4) compared to the undoped reference (P1), synthesised by one-step AP-PECVD; (b) Zoomed Raman shifting (E_g band) of the spectra.
- Figure 3.4** (a) Raman spectra of the undoped and boron-doped samples deposited on optical fibres (OFs); (b) XRD patterns of samples P1(undoped) and P3 (B-TiO₂) deposited on Si wafers.
- Figure 3.5** Typical XPS fitted spectra for TiO₂ on the surface of sample P1: (a) Ti 2p and (b) O 1s chemical environments.
- Figure 3.6** Surface XPS spectra in the Ti 2p environment of all samples deposited on Si wafers: (a) undoped (P1) and (b, c, and d) B-TiO₂ samples P2, P3, and P4. This graph does not show fitting of the spectra.
- Figure 3.7** B1s environment XPS surface spectra of B-TiO₂ samples deposited on Si wafers.
- Figure 3.8** D-SIMS elemental analysis spectra of boron-doped TiO₂ films deposited on Si wafers, for the selected elements (O, Ti, B, and Si): (a) spectra for sample P2; (b) spectra of sample P3; (c) spectra of sample P4 and (d) comparison of the normalised

ratio Ti/B for all samples, calculated from the counts of previous spectra.

- Figure 3.9** SEM analysis: Top view SEM images of all samples deposited on Si wafers, undoped (P1) and boron-doped (P2, P3, and P4) respectively (a, b, c and d); Cross-section SEM images of all samples (e, f, g, and h).
- Figure 3.10** SEM analysis of B-TiO₂ thin film deposited by AP-PECVD on optical fibre.
(sample P5): (a) Side view of the coated optical fibre with a tilted angle; (b) SEM cross-section image of P5.
- Figure 3.11** Representation of Tauc Plot for the calculation of the optical band gap of undoped and boron-doped TiO₂ samples, synthesised by AP-PECVD. P1 is the undoped TiO₂ sample.
- Figure 3.12** Photocatalytic test for all samples: (a) linear representation (Ln(C₀/C) vs irradiation (UV) time) of the degradation of MB; (b) Bar diagram as function of rate constant of the reaction (h⁻¹·cm⁻²) of degradation of MB. Sample P1 is the reference (undoped); samples P2-P4 are boron-doped TiO₂ samples.
- Figure 3.13** Photocatalytic test for P3 vs P1:(a) Linear representation of photodegradation of methylene blue (MB) for undoped TiO₂ and B-TiO₂ thin films as Ln(C₀/C) vs irradiation (UV) time for B-TiO₂ thin film, sample P3 compared to undoped TiO₂ sample, sample P1; (b) Bar diagram as function of rate constant of the reaction (h⁻¹·cm⁻²) of degradation of MB. Different bars corresponding to different consecutive cycles of photocatalysis are represented as 1^o, 2^o, and 3^o.
- Table 4.1** Experimental parameters of the AA-PECVD depositions.
- Figure 4.1** Schematic of the AA-PECVD setup for boron doping of TiO₂. Planar substrate was chosen for this representation. When the deposition was performed on optical fibre substrates, the polymeric optical fibre was passed through the reactor, as shown in figure 1 of chapter 3.
- Figure 4.2** (a) XRD patterns of boron-doped TiO₂ thin film samples (3, 4, 5 and 6 mol. % of boron in solution) compared to the undoped TiO₂ thin film, deposited on silicon wafers; (b) graphic representation of average crystal size vs the molar and atomic (%) concentration of boron in the solution of the precursor and in the resulting films, respectively.
- Figure 4.3** (a) Raman spectra of boron-doped TiO₂ thin film samples (3, 4, 5 and 6 mol. % of boron in solution) compared to the undoped TiO₂ thin film; (b) zoomed Eg band, showing the shifting of the peak for all of the samples.

- Figure 4.4** SEM images of (a) undoped TiO₂ and (b, c, d and e) B-TiO₂ thin films. 3%, 4%, 5% and 6% represent the mol. % of boron in solution, when preparing the precursor.
- Figure 4.5** SIMS analysis of undoped and boron-doped TiO₂ thin films synthesised by AP-PECVD: SIMS mapping, 10x10 μm², of the selected elements (O, Ti and B) for undoped TiO₂ (a) and boron-doped TiO₂ (b) thin films; (c) Depth profiling of the selected elements (O, Ti, B and Si) for the B-TiO₂ film; (d) SIMS mapping of boron (coloured scale) of a 20x20 μm² image of B-TiO₂ thin film.
- Figure 4.6** B 1s XPS spectra of: (a) B-TiO₂ (3%); (b) B-TiO₂ (5%) and (c) B-TiO₂ (6%). Dotted straight lines indicating the position of the peaks after deconvolution.
- Figure 4.7** (a) Transmittance spectra of B-TiO₂ thin films compared to undoped TiO₂ film; (b) zoomed transmittance/adsorption edge from previous graph and (c) Tauc plot for the calculation of the optical band gap (4%-6% B-TiO₂ samples).
- Figure 4.8** (a) average formal quantum efficiencies (FQE) obtained during photodegradation of stearic acid under UV irradiation of B-TiO₂ samples compared to undoped TiO₂ synthesised under the same conditions (reference); (b) visible light activity, given as rate of degradation of stearic acid (RSA), of selected B-TiO₂ (5%) film. The visible light test is presented for 3 consecutive cycles of photocatalysis.
- Figure 5.1** (a) Comparison of Raman spectra: W-TiO₂ films samples of different concentrations vs undoped TiO₂ synthesised and deposited on POFs under the same conditions; (b) inset of the Eg band shifting in Raman; (c) XRD patterns of W-TiO₂ thin films deposited on glass.

List of Abbreviations

AACVD	Aerosol-assisted chemical vapour deposition
APCVD	Atmospheric pressure chemical vapour deposition
% at.	Atomic percent
B.E.	Binding energy
AP-PECVD	Atmospheric pressure plasma enhanced chemical vapour deposition
AA-PECVD	Aerosol-assisted plasma enhanced chemical vapour deposition
CVD	Chemical vapour deposition
EDS	Energy dispersive x-ray spectroscopy
BG	Optical band gap
FQE	Formal quantum efficiency
FQY	Formal quantum yield
PVD	Physical vapour deposition
PXRD	Powder x-ray diffraction
SEM	Scanning electron microscopy
TCO	Transparent conducting oxides
T-R	Transmittance - reflectance
UV-vis	Ultra violet and visible light wavelength
Vo	A vacancy on an oxygen - site
WDS	Wavelength dispersive x-ray spectroscopy
XPS	X-ray photoelectron spectroscopy
XRD	X-ray diffraction
APPJ	Atmospheric Pressure Plasma Jet
MPT	Microwave plasma torch
MIPs	Microwave induced plasmas
DBD	Dielectric barrier discharge
ICP	Inductively coupled plasma
MPJ	Microwave plasma jet

List of Publications

- **Interstitial Boron-Doped TiO₂ Thin Films: The Significant Effect of Boron on TiO₂ Coatings Grown by Atmospheric Pressure Chemical Vapor Deposition.**

Quesada-Gonzalez, M.; Boscher, N. D.; Carmalt, C. J.; Parkin, I. P.
ACS Appl. Mater. Interfaces **2016**, 8 (38), 25024–25029. DOI:
10.1021/acsami.6b09560

- **On the apparent visible-light and enhanced UV-light photocatalytic activity of nitrogen-doped TiO₂ thin films**

Quesada-Cabrera, R.; Sotelo-Vazquez, C.; Quesada-Gonzalez, M.; Melian, E. P.; Chadwick, N.; Parkin, I. P.
J. Photochem. Photobiol. A Chem. **2017**, 333, 49–55. DOI:
10.1016/j.jphotochem.2016.10.013

- **Interstitial Boron-Doped Anatase TiO₂ Thin films on Optical Fibres: Atmospheric Pressure-Plasma Enhanced Chemical Vapour Deposition as the Key for Functional Oxide Coatings on Temperature-Sensitive Substrates.**

Quesada-González, M.; Baba, K.; Sotelo-Vázquez, C.; Choquet, P.; Carmalt, C. J.; Parkin, I. P.; Boscher, N. D.
J. Mater. Chem. A, **2017**, 5, 10836-10842. DOI: 10.1039/C7TA02029E

- **Significance of a Noble Metal Nanolayer on the UV and Visible Light Photocatalytic Activity of Anatase TiO₂ Thin Films Grown from a Scalable PECVD/PVD Approach**

Baba, K.; Bulou, S.; Quesada-Gonzalez, M.; Bulou, S.; Collard, D.; Boscher, N. D.; Choquet, P.
ACS Appl. Mater. Interfaces, **2017**, 9 (47), 41200–41209. DOI:
10.1021/acsami.7b10904

- **Deeper Understanding of Interstitial Boron-Doped Anatase Thin Films as A Multifunctional Layer Through Theory and Experiment.**

Quesada-Gonzalez, M.; Williamson, B. A. D.; Sotelo-Vazquez, C.; Kafizas, A.; Boscher, N. D.; Quesada-Cabrera, R.; Scanlon, D. O.; Carmalt, C. J.; Parkin, I. P.
J. Phys. Chem. C **2017**, DOI: 10.1021/acs.jpcc.7b11142

- **Patent: Device for performing atmospheric pressure plasma enhanced chemical vapour deposition at low temperature**

Baba, K.; Boscher, N. D.; Bulou, S.; Choquet, P.; Gerard, M.; Quesada-Gonzalez, M.
September 2016/ Patent: LU93221

Contents

Chapter 1	3
Introduction.....	3
1.1 Aim of this PhD Thesis	3
1.2 Why TiO ₂ thin films and how to improve them: doping	5
1.3 Boron-doped TiO ₂	9
1.4 Synthesis of doped-TiO ₂ : APCVD.....	11
1.4.1 Aerosol-assisted chemical vapour deposition (AACVD).....	13
1.5 AP-PECVD: an approach for thermo-sensitive substrates.	14
1.5.1 DC and low frequency discharges	16
1.5.2 RF discharges	16
1.5.3 Microwave induced plasmas (MIPs).....	18
1.6 Thesis structure: What lies ahead in this thesis?	21
Chapter 2	23
2.1 Introduction	23
2.2 Experimental Methodology	26
2.2.1 Atmospheric Pressure Chemical Vapour Deposition (APCVD)	26
2.2.2 Analytical Methods	28
2.2.3 Photocatalytic Test	29
2.3 Theoretical Methodology.....	30
2.3.1 Defect Formalism.....	31
2.3.2 Chemical Potential Limits	32
2.4 Results and discussion	33
2.4.1 Structure discussion	35
2.4.2 Boron doping	41
2.4.3 Morphology of the films.....	45
2.4.4 Functional properties of the films	50
2.4.5 Defect Thermodynamics:.....	54
2.4.5.1 Bulk electronic properties:	54
2.4.5.2 Defects:.....	55
2.4.5.3 B-Doping:.....	59
2.5 Conclusions:	62
Chapter 3.....	64

3.1 Introduction	64
3.2 Experimental Section.....	68
3.2.1 Atmospheric Pressure Plasma Enhanced CVD (AP-PECVD) setup .	68
3.2.2 Analytical techniques	71
3.2.3 Photocatalytic test	71
3.3 Results and discussion:	72
3.3.1 Synthesis of the samples: structure & morphology	72
3.3.2 Morphology of the films.....	81
3.3.3 Functionality of the samples:	83
3.4 Conclusions	88
Chapter 4	90
4.1 Introduction	90
4.2 Experimental Section.....	93
4.2.1 Aerosol-Assisted Plasma Enhanced CVD (AA-PECVD) configuration	
.....	93
4.2.2 Analytical Methods	96
4.2.3 Photocatalytic Test	97
4.3 Results and discussion	98
4.3.1 Structure and morphology	98
4.3.2 Functional properties.....	107
4.4 Conclusions.....	112
Chapter 5	113
5.1 Conclusions: summary of results	113
5.2 Future work: promising results.....	118
References	120

Chapter 1

Introduction

1.1. Aim of this PhD Thesis

The PhD thesis presented here reports on new functional coatings, based on boron-doped TiO₂, which were deposited by different techniques on matrices and substrates of a diverse nature. The purpose of the research can be defined as a combination of the improvement and the understanding of the deposition mechanisms as well as the development of a large range of multi-functional and intelligent surfaces on almost all types of solid surfaces. The new generation of thin films will be used mainly as photocatalysts and in water splitting. The techniques to be used to synthesise and achieve the project objectives are atmospheric pressure chemical vapour deposition (APCVD) and plasma-enhanced chemical vapour deposition (PECVD). These techniques were chosen due to the advantages which they present when compared to other techniques. They guarantee one step synthesis procedure and the possibility to easily adapt the whole process to an upscale industrial synthesis.

Nevertheless, when doping TiO₂, new challenges appear and are present when the dopant deposition parameters should be controlled to achieve the nature and chemistry of the dopant which is required for our purposes, keeping the properties, which are desirable and maintaining the stability of the dopant levels within the bulk and surface of the doped TiO₂ films.

The realisation of this thesis was directly connected to an international collaboration between University College London (UCL) and a core project called “PlasmOnWire” funded by the FNR in Luxembourg.

The PlasmOnWire project aims at developing functional and smart nanocomposite coatings from a new atmospheric pressure plasma process. Among the wide range of techniques used to grow nanocomposite films, atmospheric pressure plasma assisted chemical vapour deposition is a newly arising and promising environmentally friendly and easily up-scalable technology. Focus will concentrate on the understanding of the deposition mechanisms related to both heterogeneous and homogeneous reactions to tailor the thin films microstructure, composition and nanoparticles loading. The technical solutions and the product concepts will be chosen to be flexible. On changing the host matrix, the dopant and the plasma deposition conditions, it will be possible to develop a large range of multi-functional and intelligent surfaces on almost all solid surfaces. This project also aims at depositing nanocomposite coatings with an innovative in-line continuous atmospheric pressure deposition process to produce new functional and intelligent polymer fibres in an efficient way. This innovative deposition process will allow a wide range of new applications based on high-tech fibres (sensors, photocatalysis, sustainable hydrogen production) by simply changing the precursor (CVD), the nanoparticles (CVD, nebulizer), the process gas, and the plasma parameters. Potential impacts on health and the environment of the PlasmOnWire process are much lower than other competitive processes (wet chemistry, electrodeposition, sol-gel, etc) because the quantity of reactive materials and the energy used for the material deposition is much lower for plasma processes. A multi-disciplinary approach will be used, involving physics for the understanding of the plasma processes and plasmonic behaviour, engineering sciences for the development of a new in-line atmospheric pressure plasma process, chemistry of the deposition process and materials characterization to better understand and predict materials phenomena. During the first part of the project, the new active or smart materials will be prepared at laboratory scale and during the second part, it will be up-scaled on the CRP-GL plasma wire demonstration pilot (speed line 15 m/min and total cable length 200 m).

Several Luxembourgish companies producing or treating wires and fibres (ArcelorMittal Bettembourg, Textilcord Steinfort, Goodyear, Hyosung, etc) are potentially interested at short, mid or long-term of this sustainable and mass production deposition process.

While the PlasmOnWire project aims at improving the photocatalytic properties of AP-PECVD anatase TiO₂ thin films through the embedment of noble metal nanoparticles, the PhD project here reported has investigated the doping of the AP-PECVD anatase TiO₂ thin films by boron. Such approach is expected to provide a simpler and cost-effective solution for the improvement of the photocatalytic properties. Beyond the photocatalytic properties, an enhancement of the electrical conductivity was also targeted.

1.2 Why TiO₂ thin films and how to improve them: doping

Thin films of anatase titanium dioxide (TiO₂) have been extensively studied over the past decades because of their potential applications, such as self-cleaning,^{5,7} water splitting,⁸ gas sensing⁹ and solar-cell devices,¹⁰ due to the fact that they can be relatively easy synthesised causing a minor impact on the environment and resources, which make them interesting for any kind of up-scalable or industrial process of manufacturing.¹¹ Most of the TiO₂ thin-film research has been aimed at improving the self-cleaning properties of the anatase phase.¹² From the three semiconducting polymorphs of TiO₂, anatase, rutile and brookite; anatase TiO₂ is the leading material for self-cleaning applications due to its chemical inertness, mechanical robustness, durability to extended photocatalytic cycling, low cost and high photocatalytic activity.¹³

Thin films of TiO₂ have been demonstrated to decompose organic pollutants by being activated through UV light,⁵ bacteria,¹⁴ viruses¹⁵ and cancer cells.¹⁶ It has been commercially applied in self-cleaning windows and tiles, as well as in air/water purification systems.¹ The fundamental facets of photocatalysis on TiO₂ are still being rigorously investigated and have recently become quite well understood.² Anatase TiO₂ powders show a bandgap of ~3.2 eV, falling into the UV light region of the electromagnetic spectrum.⁷ When a photon with energy

greater than or equal to the bandgap energy is absorbed, a photo-excitation occurs, promoting an electron from the valence band to the conduction band. This creates an excited electronic state (e^-) and concomitant hole (h^+). These photo-generated electrons and holes migrate from the bulk to the lower energy material surface where they become temporarily trapped. Donor molecules (B) near the trapped holes, such as water, react to form radical species. Acceptor molecules (A), such as di-oxygen, react with trapped electrons to form super-oxide species. These highly reactive species then oxidise any organic species in contact with the TiO_2 surface into carbon dioxide, water and mineral acids. The time-scales in which each of these processes occur differ substantially.

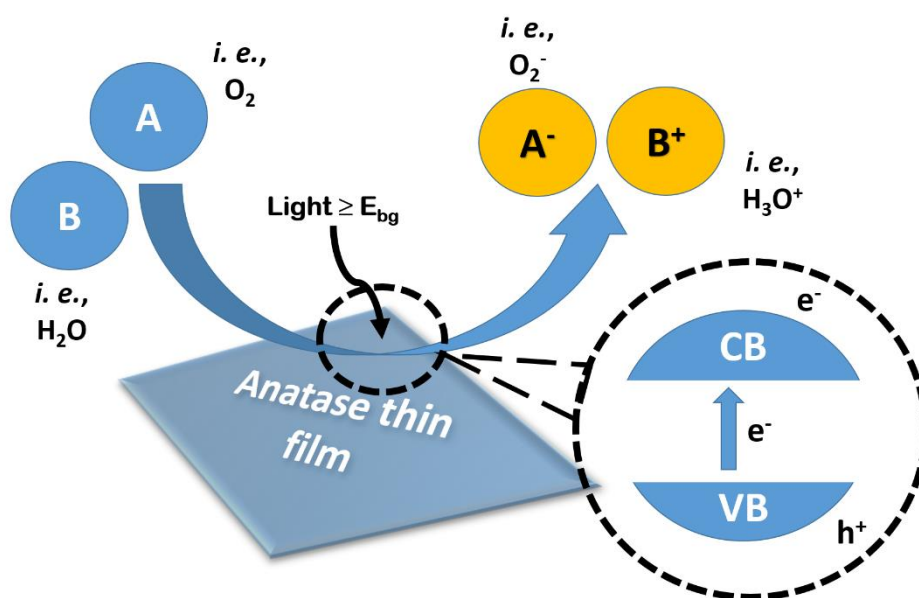


Figure 1.1 Graphic representation of the photocatalytic activation/reaction of anatase TiO_2 thin-film on the surface. A & B represent electron acceptor and donor molecules, respectively; the E_{bg} is the band gap of the semiconductor (~ 3.2 eV).

The general mechanism of photocatalysis in a semiconductor can be summarised as shown in **Figure 1.1**. The role of the charge carriers and oxygen on the overall reaction has been a source of debate.¹⁷ It has been postulated that charge carriers (generated in the photonic excitation) have a critical role in the oxidation of organic compounds on the TiO₂ surface, but it is mainly through the formation of highly reactive intermediates, such as hydroxyl radicals ($\bullet\text{OH}$), superoxide ions (O^{2-}) and hydroperoxyl radicals ($\bullet\text{OOH}$) that the reaction occurs efficiently.⁷ However, some research groups have claimed that the oxidation reaction is directly linked to formation of holes (h^+) rather than the radicals and ions formed during irradiation.

There is no evidence of a marked loss in semiconductor-sensitised photoactivity with extended use. The photocatalytic rates of any semiconductor thin film, under a steady photo-exciting flux of light, follow the kinetics proposed by the model Langmuir-Hinshelwood and are primarily dependent on four physical characteristics of the films:

(1) **the semiconductor bandgap energy**; determines the region of the photon excitation source that will be absorbed in generating separated electrons and holes.

(2) **the material thickness**; rules the fraction of the photon excitation source that can be absorbed.

(3) **the surface roughness**; determines the number of active sites on the surface for radical/ superoxide generation and the degree of organic contact.

(4) **the film crystallinity**; imposes the transport properties of the photo-generated electrons and holes to the film surface as well as the bandgap energy.

For the last century, researchers have tried many attempts to improve the TiO₂ thin-film self-cleaning function.¹¹ There are mostly three common methods that have been used for achieving this improvement: (a) coupling composites,^{14,18–21} (b) modifying the surface^{22–24} and (c) doping.^{25–29}

(a) When it comes to coupling composites, two main strategies are considered. One strategy involves coupling TiO₂ with a semiconductor of lower bandgap energy such as WO₃ (2.8 eV) or CdS (\approx 2.5 eV).¹⁹ In this case, photons incapable of photo-exciting TiO₂ can excite the lower bandgap energy material. Depending on where the band potential of the coupled semiconductor transforms TiO₂, either the photo-excited electron can move down into the conduction band of TiO₂ or

the hole can move up into the valence band of TiO₂. This increases the separation of the photo-generated electrons and holes and reduces recombination rates. The second coupling strategy involves coupling TiO₂ with a noble metal such as silver,¹⁴ gold³⁰ or platinum.³¹ Photo-generated electrons formed on the TiO₂ semiconductor can be trapped into the coupled metal's density of states (DOS), raising the Fermi level. This also increases the separation of the photogenerated electrons and delays recombination processes.

(b) Another common approach for improving the photocatalytic properties of TiO₂ is by modifying the surface. The modification consists of chemically binding molecules to the surface, such as phosphate²³ or carboxylate groups,²⁴ therefore, the susceptibility of the TiO₂ surface to attract or repulse specific organic compounds is altered. This can increase the selectivity of absorption at the surface-active sites as well as change the rate of photogenerated electron-hole surface capture and release. In some cases, the rate of hydroxyl radical formation can substantially increase, boosting photocatalytic oxidation processes.²³

(c) The most popular way of improvement of the TiO₂ photocatalytic performance is doping. One of the main challenges for the scientific and industrial community involved in photocatalytic research is to increase the spectral sensitivity of TiO₂-based photocatalysts to visible light. A major area of future research would be the development of new dopants, new method of dopant incorporation into TiO₂ structure as well as new application for environmental technology. Future and current works are dealing with visible light-activated TiO₂ functioning in the presence of solar irradiation. The most important challenge for the catalysis based on TiO₂ materials is the synthesis of stable TiO₂ with predictable photoactivity in a wide range of the light spectrum, UV and visible light.¹¹

The development of photocatalysts exhibiting high reactivity under visible light (> 400 nm) should allow the main part of the solar spectrum, even under poor illumination of interior lighting, to be used. Several approaches for TiO₂ modification have been proposed: metal-ion implanted TiO₂ (using transition metals: Cu, Co, Ni, Cr, Mn, Mo, Nb, V, Fe, Ru, Au, Ag, Pt),³²⁻³⁴ reduced TiO_x photocatalysts,^{35,36} and non-metal doped-TiO₂ (N, S, C, B, P, I, F)³⁰⁻³²

1.3 Boron-doped TiO₂

The current problem with doped TiO₂ might be the loss of photoactivity during recycling and long-term storage. It has been assumed that the efficiency of metal doped-TiO₂ under visible light strongly depends on the synthesis method used. In some cases, such doped photocatalysts showed no activity under visible light and/or lower activity in the UV spectral range compared to the non-doped TiO₂ because of high carrier recombination rates through the metal ion levels.²⁰ The main present problem with nonmetal-doped TiO₂ photocatalyst is that the photocatalytic activity under visible light is much lower than that under ultraviolet light.

Therefore, development of new and optimization of existing photocatalysts exhibiting activity upon visible light with surface characteristics of improved performance and of the high chemical and physical stability are critical for larger scale utilization of photocatalytic systems in commercial and industrial application. These materials together with the development of technically applicable self-aligning photo-catalytic coating systems adaptable to a broader type of substrates (polymers, fibres, ceramics, etc) will represent a ground-breaking step change in this field particularly in the economic viability of a range of potential processes.

There are mainly two types of dopants, n-type, extensively used in the production of solar cells, and the p-type, which contributes with extra hole energy levels.³⁷ Generally, when a non-metal, such as nitrogen, is used as a dopant, it raises the valence band maximum resulting in increasing photocatalytic activity of the TiO₂.³⁸ When doping with a cationic dopant, the conductivity increases and the resistivity decreases but usually in detriment of photocatalytic activity. The largest part of research in doping TiO₂ has been focused on the improvement of photoactivity performance by increasing the visible light absorption of Titania. To create a visible light responsive material, doping with non-metal has become the cusp of the field.^{11,12}

The different pathways of expanding the visible light response of TiO₂ by doping the band gap were suggested in the literature.^{2,39} These are shown in **Figure 1.2** and include: (1) a classic narrowing of the band gap produced by the combination of the nonmetal dopant and the pure TiO₂, (2) a model where oxygen-deficient TiO₂ generates empty levels close to the conduction band (CB), (3) a localized mid-gap level model induced by the nonmetal dopant and (4) a combination of the two previous models (oxygen vacancies and mid-gap).

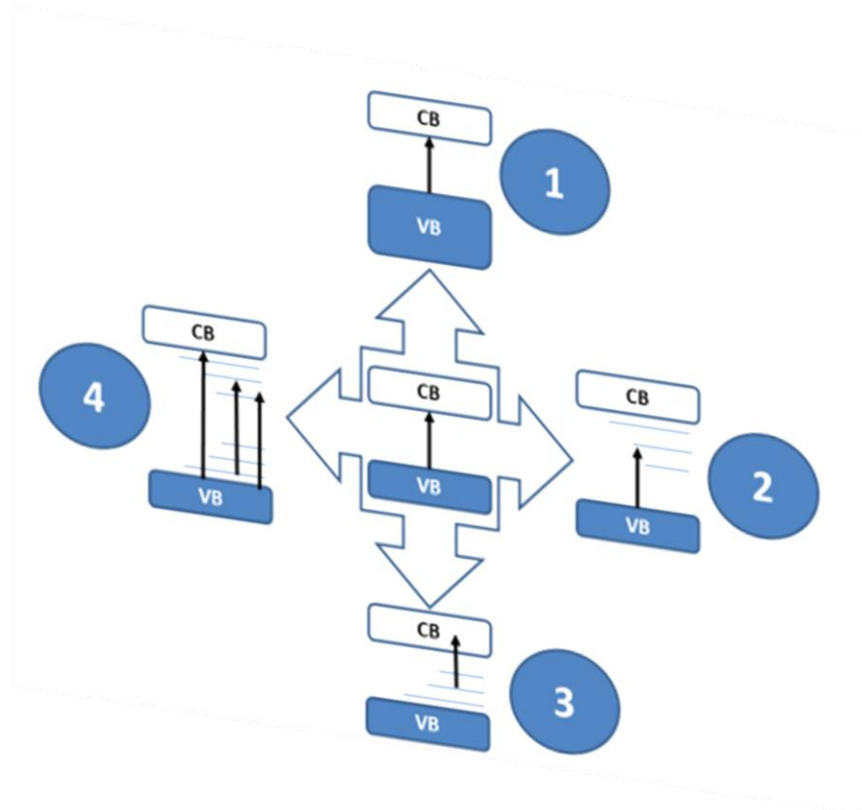


Figure 1.2. Scheme of the models for the TiO₂ band gap changes when nonmetal doping.

Boron doping of TiO₂ has attracted attention due to its inductive creation of electron acceptor levels.⁴⁰ When boron is doped into the TiO₂ lattice, boron atoms can occupy two different positions, an interstitial position and a substitutional position by filling up the oxygen vacancies. Some researchers observed a blue shift in the band edge of boron doped TiO₂ when boron occupies an interstitial site owing to quantization effects, which improve the photocatalytic activity by intense absorption in the UV range.⁴¹

In addition, to reach the red shift in the absorption edge, other studies have suggested that boron substituting oxygen in the TiO₂ lattice can create mid-gap

states and narrow the band gap enhancing the visible light absorption and consecutively increasing the photoactivity.^{42,43}

Comparing both, substitutional and interstitial sites, interstitial occupancies of B do not cause any significant change in the band gap, although there are suggestions that interstitial boron reduces Ti^{4+} to Ti^{3+} promoting separation of the photoexcited electron and hole pairs, dropping down their recombination.⁴⁴ Theoretically, the changes in the band gap when doping with boron are well defined correlating with the position which boron is occupying in the anatase lattice.⁴⁵

The reported methods of synthesis which can be used for the formation of TiO_2 thin films include the sol-gel method,³ hydrothermal method,⁴⁶ surface impregnation, electrochemical deposition,¹¹ physical⁴⁷ and chemical vapour deposition methods.⁴

Principally, the synthesis of boron-doped TiO_2 has been focused on the formation of powders by sol-gel, annealing and hydrothermal methods. Recently, B- TiO_2 thin films deposited by APCVD have been reported for the first time by Carmichael *et al.*⁴⁸ The boron dopant, incorporated in an O-substitutional position into the TiO_2 , did lead to remarkable rates of hydrogen production and more favourable photocurrent profiles when compared to non-doped samples.

1.4 Synthesis of doped- TiO_2 : APCVD

The reported methods of synthesis which can be used for the formation of TiO_2 include the sol-gel method, hydrothermal method, ion implantation, surface impregnation, chemical vapour deposition and electrochemical methods.⁴⁹

Atmospheric-pressure Chemical Vapour Deposition (APCVD) is the most commonly used approach of CVD (**Figure 1.3**), where pure precursor species are heated in a bubbler to form enhanced vapours, which are delivered by an inert carrier gas to the reaction chamber. These reactants, in the gas phase, chemically react when they pass through the reaction chamber, with the subsequent deposition of a solid product or thin-film on the surface of the selected substrate. The supply of the precursors to the reaction chamber is controlled by 3 parameters: (i) the vapour pressure of the precursor, (ii) operating temperature of the bubbler and (iii) the flow rate of the carrier gas (inert gas).

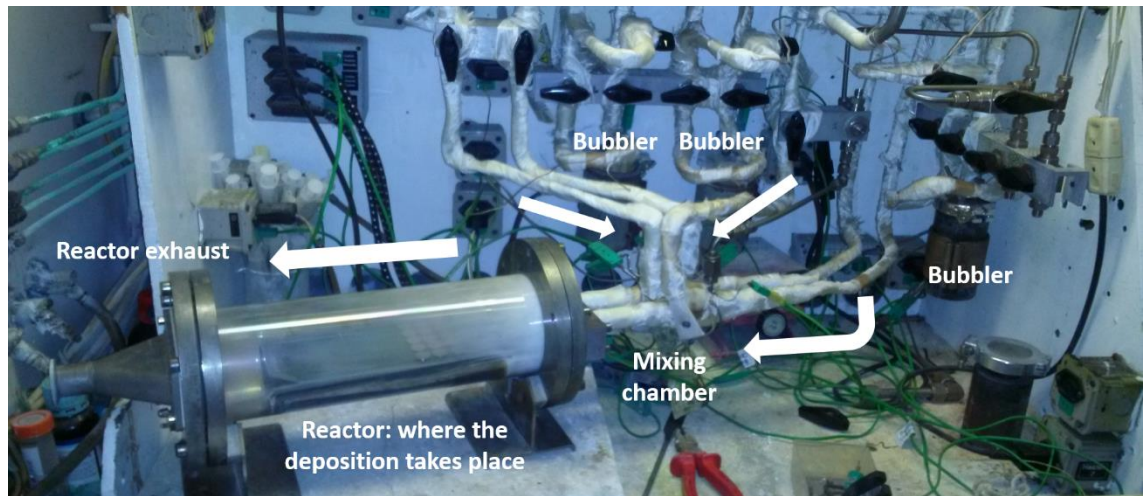


Figure 1.3. Photo of the APCVD rig built and used for this thesis

The selected precursor reactants should have a relatively high vapour pressure to facilitate the phase change transfer (from liquid to gas phase).

The APCVD method presents advantages over sol-gel routes since a calcination step is not required to obtain the crystalline anatase/rutile phases, which could affect drastically the nature and content of the dopant.⁵⁰

In APCVD to determine the gas flow, it is generally assumed that the gaseous species follow the ideal gas law:

$$\frac{N_p}{N_c} = \frac{P_p}{P_c} \quad \text{Eq. 1.1}$$

where N_p and N_c are the amount (moles) of precursor reactants and carrier gas, respectively; and P_p and P_c are the partial pressures of precursor reactants and carrier gas, respectively. If an APCVD system will only contain precursor and carrier gas species, it is commonly acknowledged that the total pressure (P_t) at the outlet of the bubbler is equal to the sum of the partial pressure of the precursor species (P_p) and the partial pressure of the carrier gas (P_c):

$$P_t = P_p + P_c \rightarrow P_c = P_t - P_p \quad \text{Eq. 1.2}$$

$$N_p = \frac{N_c \cdot P_p}{P_t - P_p} \quad \text{Eq. 1.3}$$

As previously mentioned APCVD works at atmospheric-pressure, therefore the total partial pressure (P_t) can be substituted by 760 mmHg. In APCVD processes the gas flow is measured in standard litre per minute (slm). Considering that one mole of gas is equivalent to 22.4 L, it can be concluded that dividing the carrier gas volume-flow rate, N_c , by 22.4 L would give the flow rate of the carrier gas (F_c) which is independent of temperature and pressure, and thus it can be used to calculate the flow rate of the precursor species (F_p):

$$F_p = \frac{F_c \cdot P_p}{22.4 \cdot (760 - P_p)} \quad \text{Eq. 1.4}$$

Hence, the above equation (**Eq. 1.4**) can be used to determine the flow rate of the precursor species transferred to the reaction chamber (F_p).

1.4.1 Aerosol-assisted chemical vapour deposition (AACVD).

For regular CVD processes, the precursor reactants are carried to the reaction chamber by heating a stainless-steel bubbler, where these precursors are placed, to create reactive vapours. Regardless of the advantages of APCVD, such as scalability and relative fast production of high quality coatings, there is a main limitation associated to this type of CVD; the availability of suitable chemical precursors, as the use of highly volatile chemicals are required.

Aerosol-assisted CVD was designed as a liquid-phase modification of CVD, where non-volatile precursors can be used. These non-volatile precursors are mixed with a solvent to produce a precursor-mist, which is transported to the reaction chamber by using an ultrasonic generator which creates the aerosol mist. Therefore, the major advantage of AACVD over conventional CVD

processes is the wider range of potential precursors that can be investigated, as they depend on their solubility rather than volatility.⁵¹

In addition, AACVD does not require heated lines to transport the precursor-mist and its cost is relatively low compared to conventional CVD processes.

1.5 AP-PECVD: an approach for thermo-sensitive substrates.

Plasma-Enhanced Chemical vapour deposition (PECVD) is a synthesis method where the substrate is exposed to one or more volatile precursors, in the presence of a plasma (a partially ionised gas, containing free electrons), which react or decompose on the surface to produce a deposit. The plasma enhances the rate of reaction on the substrate surface.³⁷ Plasma is an ionised gas. It is the fourth state of matter and constitutes more than 99% of the universe.

A plasma is generated by applying energy to a gas, inducing the reorganisation of the electronic structure of the species (atoms, molecules) and producing excited species and ions. In terms of classification, the atmospheric plasma sources are positioned near the glow discharges and the arcs (in between 10^{16} and 10^{20} m^{-3} , electron density).⁵²

The films typically deposited using PECVD are silicon nitride (Si_xN_y), silicon dioxide (SiO_2), silicon oxy-nitride (SiO_xN_y), silicon carbide (SiC), and amorphous silicon ($\alpha\text{-Si}$). Silane (SiH_4), the silicon source gas, is combined with an oxygen source gas to form silicon dioxide or a nitrogen gas source to produce silicon nitride.

Silicon dioxide and silicon nitride are dielectric (insulating) materials commonly used in the fabrication of electronic devices to isolate multiple conductive layers, capacitors, and for surface passivation. These films are also used for encapsulation to protect devices from corrosion by atmospheric elements such as moisture and oxygen.

Depending on the type of energy supply and the amounts of energy transferred to the plasma, the properties of the plasma change, in terms of electronic density or temperature. These two parameters distinguish plasmas into different categories, presented in **Figure 1.4**. The atmospheric plasma sources described

in this thesis are supposed to be positioned near the glow discharges and the arcs. The excitation frequency is important since it influences the behaviour of the electrons and the ions.

The atmospheric plasma sources can be classified regarding their excitation mode. Three groups are then highlighted: (I) the DC (direct current) and low frequency discharges; (II) the plasmas which are ignited by radio frequency waves; and (III) the microwave discharges (see **Figure 1.5**).

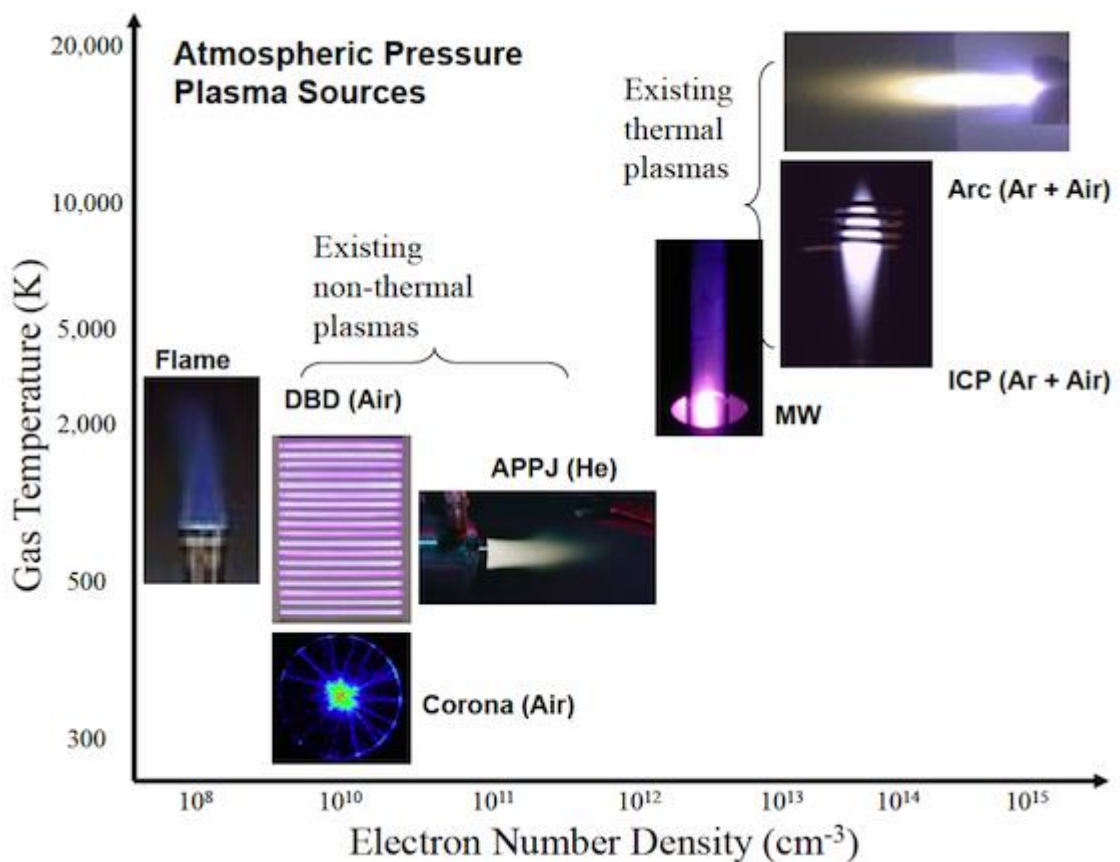


Figure 1.4. Classification of atmospheric plasmas. Figure taken from Los Alamos National Laboratory—Yongho Kim, ICOPS/BEAMS 2014 conference.

1.5.1 DC and low frequency discharges

Depending on their design, the DC and low frequency discharges can work either with a continuous or a pulsed mode. A pulsed working mode enables the injection of large energy amounts in the discharge while the system warming up is limited. On the other hand, a pulsed power supply is technically more complex than a DC source and compromises the reproducibility of the process.

1.5.2 RF discharges

PECVD reactors are often powered at frequencies lying between 1 MHz and 200 MHz, that is within the radio-frequency (RF) domain, *i. e.*, the helicon sources used for space plasma propulsion are also driven in the RF domain, usually at 13.56 MHz.⁵³ Frequencies around 13.56 MHz and its harmonics are popular choices, most other parts of the spectrum are allocated to telecommunications.

The RF PECVD reactors can work with a high or low power supply. The kind of power supply influences the properties of the plasma and thus its potential applications. An example of a high-powered RF reactor is the inductively coupled plasma (ICP) torch, where the generated plasma is initiated and maintained by an RF fed helical coil. The amount of power transferred to the plasma electrons by the bias supply is usually such that the RF power from the substrate-holder contributes only marginally to the plasma density, meaning that, it is the power supplied to the ICP coil that controls ion flux.⁵³

An example of a low-powered RF PECVD source is the called atmospheric pressure plasma jet (APPJ), which is a system that consists of two concentric electrodes. The plasma gas flows through the electrodes and the gas is ignited by supplying a voltage (between 100-150 V) to the inner electrode.⁵²

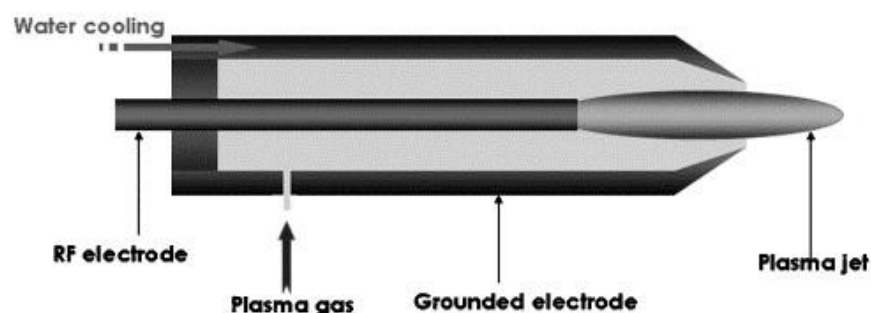


Figure 1.5. Schematic for the design of an APPJ reactor. Taken with permission from reference 51

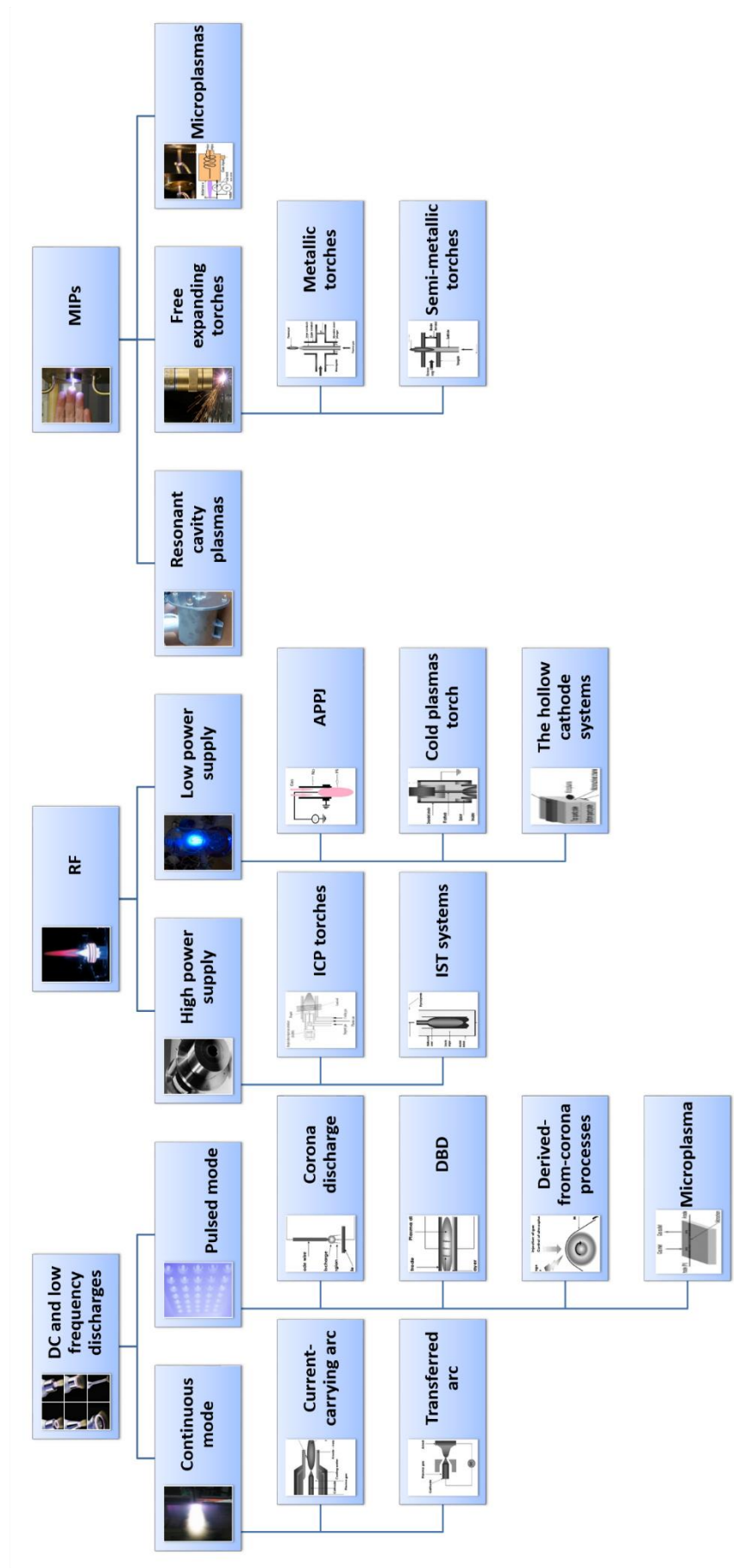


Figure 1.6. Classification of atmospheric plasmas. Adaptation from reference 51

1.5.3 Microwave induced plasmas (MIPs)

The main characteristic of microwave systems is that all work without electrodes and according to the same principle: microwaves are generated along the system and they transmit energy to the plasma gas electrons, being the source of ionisation. Elastic collisions between electrons and heavy particles occur. Due to the large mass of heavy particles, the collided electrons rebound whereas the heavy particles remain static. The electrons get kinetic energy so are accelerated and the heavy particles are slightly heated. After several elastic collisions, the electrons get enough energy to produce inelastic exciting or even ionising collisions. The gas is partially ionized and becomes plasma which supports microwave propagation ⁵⁴

Therefore, the microwave plasma reactors are all designed according to the same idea and they consist of: (a) a microwave power supply, with a circulator to protect the magnetron from the reflected power; (b) microwave equipment (wave guides, tuning system); (c) an ignition system to generate a spark; and (d) a gas injection. The atmospheric MIPs can be classified in three categories:

1.5.3.1 Resonant cavity plasmas.

The system contains a cavity which uses resonance phenomena to amplify the waves. The interior surfaces of the cavity reflect one type of wave. When a wave that is resonant with the cavity enters, it bounces back and forth within the cavity, causing a low-energy loss and a standing wave is then generated. As more waves enter the cavity, they combine with the standing wave and reinforce it, increasing its energy. This energy is used to initiate the discharge. The resonance frequency of the cavity strongly depends on its geometry parameters, especially on its radius. Thus, it is necessary to fit the geometry of the cavity with the frequency delivered by the microwave generator (2.45 GHz), to ensure the ignition of the plasma.

1.5.3.2 Free expanding torches.

Free expanding torches are called this way since the plasma source is created and flows in open air. Depending on the structure and components of the torches, a distinction can be made between the metallic and the semi-metallic torches.

The semi-metallic torches (**Figure 1.7**) are designed in a similar way to the metallic torches. The main difference is the propagation mode of the electromagnetic waves, as for the metallic one, the plasma gas flows in the inner coaxial line conductor and exits through a nozzle, whereas, for the semi-metallic one, there is no guide-to-coaxial line transition. In the semi-metallic torches, the plasma gas flows through a quartz tube. Instead of burning out on top of the nozzle, the discharge is initiated in the zone where the quartz tube intersects the rectangular wave guide ⁵⁵

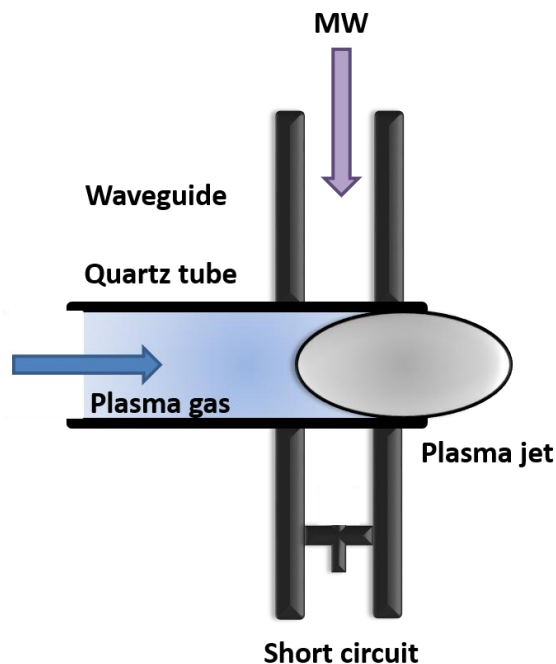


Figure 1.7. Simplified scheme of the design of a semi-metallic MW torch

1.5.3.3 MW Microplasmas.

MW Microplasmas is a low-powered, compact microwave induced plasma source. The MW microplasma or microstrip plasma consists basically of a planar microstrip line on fused silica, playing the role of dielectric substrate, and a big copper ground plate. It involves surface waves that propagate in a gas channel along the interface between the dielectric substrate and the plasma. The tiny size of the system limits the energy loss in the dielectric. This microstrip plasma technology has been mainly applied to atomic emission spectroscopy^{56,57}

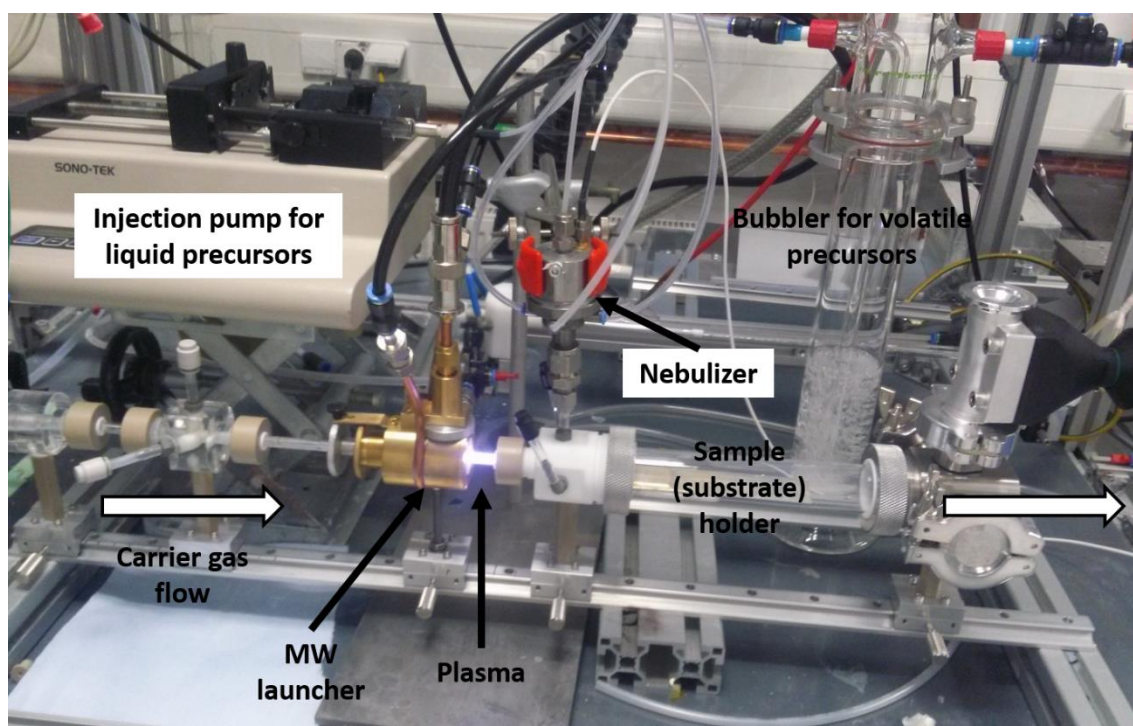


Figure 1.8. Photo of the MW AP-PECVD reactor employed for the synthesis of thin films in this thesis.

1.6 Thesis structure: What lies ahead in this thesis?

In this introductory chapter, an explanation of the purpose of this thesis and the structure of the project in which the research has been carried out, has been outlined and highlighted. In this chapter, the importance and the utility of the TiO₂ thin films were explained, as well as the efforts to improve its natural self-cleaning and photocatalytic properties. A global overview of the major methods and techniques employed for the synthesis of TiO₂ and doped-TiO₂ thin films was also provided, focusing mostly on the two techniques which were selected for the synthesis of the thin films during this PhD thesis. The selected techniques were APCVD and AP-PECVD

In the following chapter, **Chapter 2**, the synthesis and chemical modification of TiO₂ thin films by APCVD and the addition of boron species to its structure will be explored.

Followed by **Chapters 3 and 4**, where the synthesis, by AP-PECVD, and characterisation of boron-doped TiO₂ thin films will be discussed in detail and presented for two different approaches of PECVD.

The low-temperature deposition of photocatalytic crystalline metal oxide thin films and the simultaneous doping of the oxide, all in one-step synthesis, on polymeric temperature-sensitive substrates, represents a challenge for the scientific community. The one-step AP-PECVD approach, which will be presented in the following chapters, avoids the high substrate temperature and complex steps that are often encountered when synthesizing crystalline transition-metal oxides thin films via other techniques. The methodology presented here overcomes the challenge of forming crystalline transition-metal oxide coatings on polymer substrates from a dry and up-scalable method and allows simultaneously to dope the material which is being deposited.

The utility of our approach is demonstrated by coating a side glow polymer optical fibre (i.e. PMMA) with dense and crystalline boron-doped TiO₂ thin films. The photocatalytic activity of the anatase boron-doped TiO₂ coatings presented in this work is of interest for a wide range of applications, including air and water decontamination by optical fibres reactors. Our demonstration of a simple one-step and scalable deposition approach for creating highly efficient photocatalytic

B-TiO₂ coatings on polymer substrates represents a new achievement to the field due to the complex chemical nature of boron when used as dopant for TiO₂.

Finally, as a summary of the observations and results from all the experimental and theoretical data extracted, the conclusions will be summarised in **Chapter 5**, which presents as well possible future paths for further research in the field.

Chapter 2

Interstitial boron-doped TiO₂ synthesised by APCVD

2.1 Introduction

As previously discussed in Chapter 1, titanium dioxide (TiO₂) has been the most extensively studied photocatalytic material, among all known photocatalytic materials, due to its multifunctional applications from desirable properties.² There has been a large research drive into the degradation of organic pollutants leading to the industrial use of TiO₂ for the production of environmental, self-cleaning and photocatalytic technologies such as the Pilkington Activ™ Glass. In the last few decades, demanding efforts have been made combining theory and experimental work to fully understand the mechanisms of photocatalysis in TiO₂ polymorphs.^{5,7} TiO₂, however, presents some disadvantages, such as low conductivity and poor electron mobility, which limits its usage for optoelectronic devices, such as transparent conductive oxides (TCO).^{58,59} Even when donor doped with Nb or W, resistivities fail to reach those of doped SnO₂, In₂O₃, ZnO or BaSnO₃. Anatase TiO₂ possesses a wide band gap ($E_g \sim 3.2$ eV) making it a UV absorber reducing its efficiency as a photocatalytic material. To improve upon this and modify the morphology of TiO₂, acceptor doping with a non-metal or a transition-metal, has become one of the most widely studied areas of research in photocatalysis and material science.⁶⁰

Generally, it has been found that when TiO₂ is doped using an acceptor, such as nitrogen, the N 2*p* states sit slightly higher than the O 2*p* states at the valence band maximum (VBM) reducing the band gap and improving the efficiency towards visible light absorption. In contrast, the use of donor doping to modify the optical properties of TiO₂ results in an increase of the conductivity. However, this increase has been found detrimental for the photocatalytic performance of these doped TiO₂ materials. The majority of research on this has been in acceptor doping with non-metals such as S, N, C or B.⁶¹ The use of these dopants has been found beneficial to expand the photocatalytic activity of TiO₂ towards visible light. For instance, N-doped TiO₂ materials have shown visible light photoactivity, however, the use of this dopant is still a source of debate in both theory and experiment, due to the ambiguous assignment of N species by X-ray spectroscopy studies.^{62,26}

Boron doping of TiO₂ has attracted attention because of its enhanced photocatalytic activity under UVA light and visible light.^{25,45,63} Boron has been proved to be very efficient in band gap narrowing and in decreasing the recombination rates of charges.^{25,42,49} However, it is not well-understood which of these factors is more effective for photocatalytic performance. When boron is introduced within the TiO₂ lattice it can substitute both oxygen and titanium sites (B_O and B_{Ti} respectively) as well as being interstitially added (B_i), making it an amphoteric dopant. Experimentally a blue shift was observed in the band edge of B-TiO₂ when boron occupies an interstitial site indicative of a Moss-Burstein shift. The Moss–Burstein effect is the phenomenon of which the apparent band gap of a semiconductor is increased as the absorption edge is pushed to higher energies as a result of some states close to the conduction band being populated.²⁵ In addition, studies showing a red shift in the absorption edge are assigned to the presence of substitutional B. This has been postulated as the creation of mid-gap states acting as absorption centres enhancing the visible light absorption and photocatalytic activity.⁴⁵ In addition, it has also been reported that interstitial boron could reduce Ti⁴⁺ to Ti³⁺, promoting the separation of the photoexcited electron and hole pairs, which would be beneficial to suppress their recombination and enhance the photocatalytic activity of boron-doped TiO₂

materials.¹⁶ However, it should be noted that the excess of electrons in anatase TiO₂ is generally delocalized in the bulk, but can localize on the surface.⁵⁹

TiO₂ has been historically synthesised using a wide range of synthetic methods, including sol-gel,³ hydrothermal,⁴⁶ and electrochemical deposition,¹¹ as well as physical⁴⁷ and chemical vapour deposition (CVD) techniques.^{4,19} It is worth mentioning that the use of CVD methods, to synthesise TiO₂ materials, presents advantages over other methodologies, such as removing the need for a calcination/annealing step which can drastically affect the nature and content of the dopant,⁵¹ and ease of industrial scale up.

In the last few decades the synthesis of B-TiO₂ has been mainly focused on producing powders by sol-gel, annealing and hydrothermal methods.⁶³ It is worth mentioning that B-TiO₂ thin films synthesised using APCVD, have been reported for the first time by Carmichael et al.⁴⁸ In this work, the as-synthesised thin films showed the presence of substitutional boron, leading to remarkable rates of hydrogen production (24 $\mu\text{L cm}^{-2} \text{h}^{-1}$) and more favourable photocurrent profiles than that observed for undoped TiO₂ materials. In this chapter, interstitial boron-doped TiO₂ thin films were grown by APCVD on a float glass substrate. Boron, when occupying an interstitial position, was found beneficial to enhance the photocatalytic performance of B-TiO₂ thin films, as well as to increase their particle crystallite size, compared to undoped TiO₂ thin films.⁶⁴ The films showed higher rates of photoactivity together with higher chemical stability when compared to substitutional boron-doped TiO₂ films. This chapter reports the synthesis and characterisation of a series of interstitial B-TiO₂ thin films, using a one-step APCVD method, allowing the synthesis of boron-doped TiO₂ films with varying concentrations of boron. The impact that interstitial boron has on the morphology, structure and functional properties of B-TiO₂ thin films is shown experimentally and by theoretical methods.

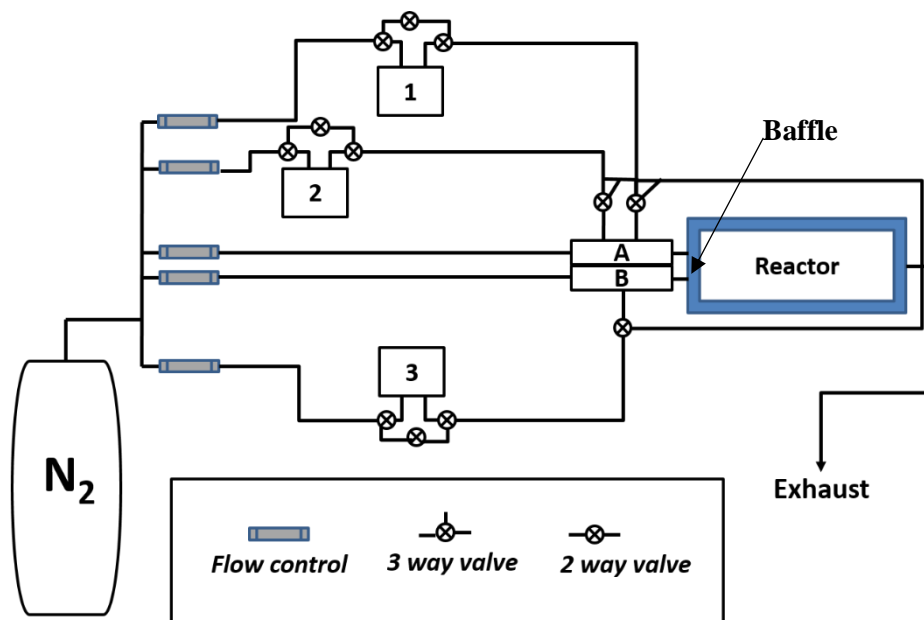
2.2 Experimental Methodology

All thin films used in this chapter, boron-doped and undoped, were synthesised using

APCVD processes. The chemicals were purchased from Sigma-Aldrich and Acros Organics. Titanium tetrachloride (TiCl₄, 99.9%), ethyl acetate (C₄H₈O₂, 99.8%), and triisopropyl borate (C₉H₂₁BO₃, 98%) were used as titanium, oxygen, and boron sources, respectively. Octadecanoic (stearic) acid (CH₃(CH₂)₁₅CH₂CHO₂, 98.5%) was used to test the photocatalytic performance of the as-synthesised thin films.

2.2.1 Atmospheric Pressure Chemical Vapour Deposition (APCVD)

All thin films, used in this chapter, were synthesised in a custom-built cold walled CVD reactor at atmospheric pressure, shown previously in Chapter 1 (**Figure 1.3**). The reaction chamber consisted of a quartz tube 330 mm in length and 105 mm in diameter and contained a graphite reactor bed, heated by three Whatman cartridges inserted into the block. The pipes of the CVD reactor were kept at 473 K. The precursors were heated independently in stainless steel bubblers in order to maintain the intended vapour pressures for each precursor. Nitrogen (supplied by BOC) preheated at 473 K was used as the carrier gas to lead the precursor vapours into stainless steel mixing chambers kept between 473-523 K, under controlled flow rate conditions (**Scheme 2.1**).



Scheme 2.1. Schematic of the APCVD apparatus used to synthesize undoped and B-TiO₂ thin films.

The flow and the temperature of the dopant precursor were varied, to evaluate the role of the dopant specie in the resulting morphology of the as-synthesised thin films. The mass flow rates of triisopropyl borate (C₉H₂₁BO₃) employed for the synthesis of B-TiO₂ (A), B-TiO₂ (B) and B-TiO₂ (C) were 0.1881 g·min⁻¹, 0.5644 g·min⁻¹ and 0.6530 g·min⁻¹, respectively. The temperature and mass flow values were constant for metal (TiCl₄) and oxygen (CH₃COOC₂H₅) precursors; 340 and 310 K and 6.4 × 10⁻³ and 3.04 × 10⁻³ g min⁻¹, respectively (table 1).

To produce a laminar flow into the reactor, a plain nitrogen flow was used to transfer the gas mixture through a triple baffle manifold. The reactor itself consisted of a graphite block (320 mm-long × 150 mm-width) contained within a quartz glass tube. The reactor was heated using three embedded Whatman heater cartridges and the temperature was controlled using Pt–Rh thermocouples.

Films were grown at 773 K on float glass substrates (89 × 225 × 4mm) supplied by the Pilkington NSG Group, which are pre-coated with a SiO₂ barrier layer to prevent ion diffusion from the glass into the film. The glass substrates were cleaned using distilled water, acetone (99%), isopropanol (99.9%) and dried in air prior to use.

2.2.2 Analytical Methods

To characterise the structure, morphology, stability and functionality of the films, several analytical techniques were employed: X-ray diffraction (XRD) patterns of the films were obtained using a Lynxeye XE Bruker-Axs D8 diffractometer. The instrument operates with a Cu X-ray source, monochromated (K α 1, 1.54 Å). Films were analyzed with a glancing incident angle (θ) of 1°. The Joint Committee on Powder Diffraction Standards (JCPDS) was used to determine the crystal structure adopted. The lattice parameters and average crystal size was determined using a Le Bail model using the GSAS-EXPGUI software suite.⁶⁵ Raman spectroscopy was carried out using a Renishaw 1000 spectrometer equipped with a 514-nm laser. The Raman system was calibrated using a silicon reference.

Characterisation of the chemical profile of the thin films was carried out by Dynamic Secondary Ion Mass Spectrometry (D-SIMS) in a Cameca SC-Ultra instrument in positive ion mode, by a bombardment with Cs⁺ ions, having an impact energy of 1.0 keV.

X-ray photoelectron spectroscopy (XPS) was used to determine the composition of the films and spectra were recorded on a Kratos Axis Nova spectrometer equipped with a monochromated Al K α X-ray source and delay line detector. Survey spectra were recorded with energy of 160 eV and higher resolution spectra were recorded at 80 eV. The analysis of the spectra and the fitting were performed by adjusting the position of the C 1s (adventitious carbon), tooled by the software CasaXPS.

A Filmetrics F20 single spot thin film machine was used to analyse film thicknesses. UV/visible spectroscopy was performed using a double monochromated PerkinElmer Lambda 950 UV/vis/NIR spectrophotometer in the 300–2500 nm range. Reflectance spectra were recorded for different positions in the range 300–2500 nm on a Helios double beam instrument standardized

relative to a silicon mirror, which allowed the thickness of the films to be also be determined *via* the Swanepoel method. Structural analysis of the powdery deposition was done by Powder XRD using a Bruker D4 Bragg–Brentano theta-2 theta reflection geometry machine equipped with Cu K_{α1+2} source powered at 40 kV, 30 mA coupled with a post-sample graphite monochromator and scintillation counter detector. The morphology of the films was studied by Scanning Electron Microscopy (SEM). The images were taken using JEOL 6301 (5 kV) and a JEOL JSM-6700F field.

The probe measurements (Hall Effect) were conducted at room temperature on an Ecopia HMS-3000 device in the Van der Pauw configuration.²⁷ Measurements were acquired at 0.58 T and a variable current of 0.1 μA to 1 nA on square-cut samples (≈1 x 1 cm). Silver paint (Agar Scientific) was used to form ohmic contacts, the integrity of which were tested prior to measurement.

2.2.3 Photocatalytic Test

The films synthesized in this work were photocatalytically evaluated by photodegradation of octadecanoic (stearic) acid (95%, Sigma-Aldrich). A thin layer of stearic acid was applied on the surface of samples by dip-coating using a stearic acid solution (0.05 M) in chloroform. The photocatalytic activity of the samples was measured under UVA (Vilber-Lourmat, 2 x 8 W, 365 nm, 2 mW cm⁻²) illumination. To monitor the degradation of the overlain stearic acid, a PerkinElmer RX-I Fourier transform infrared (FTIR) spectrometer was used (**Figure 2.1**).

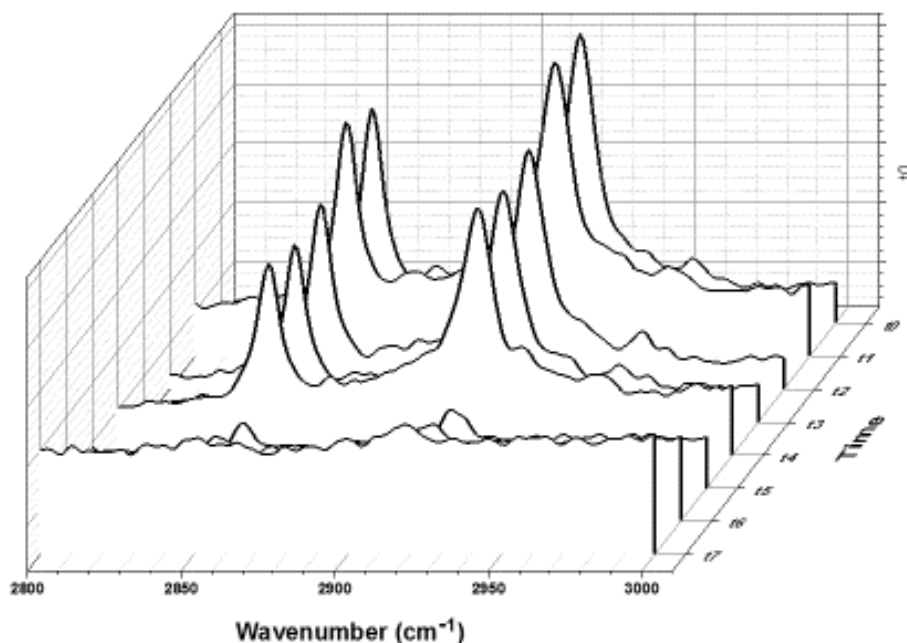


Figure 2.1. FTIR spectra of the B-TiO₂ sample coated with stearic acid upon UVA illumination (1.2 mW cm⁻²) on the B-TiO₂ film. Time is presented in hours: each cycle (t1, t2, etc) is equivalent to 2.5h.

2.3 Theoretical Methodology

For this section, as well as for the section 3.5, B. A. D. Williamson is thanked and acknowledged for the direct collaboration and useful discussions.

To build a connection between experimental characterisation and functional properties of the interstitial boron-doped TiO₂ thin films, computational analysis using ab-initio methods has been carried out on the intrinsic defects and boron incorporation in anatase TiO₂. These calculations have been carried out using the Vienna Ab-initio Simulation Package, VASP,^{66–69} a periodic boundary, plane-wave density functional theory (DFT) code. The projector-augmented wave method (PAW)⁷⁰ was employed to describe the interactions between the core electrons and the valence electrons of each species (Ti:[Ar], O:[He] and B:[He]).

In this study the hybrid DFT functional, HSE06 (Heyd-Scuzeria-Ernzerhof)^{71,72} was used to obtain detailed electronic and geometric results of boron-doped TiO₂. Hybrid functionals are less restrained by the short falls of standard DFT functionals, which fail to describe the self-interaction error and thus underestimate band gaps resulting in an inaccurate interpretation of the defect chemistry of a system. Hybrid functionals have consistently displayed increased accuracy over standard DFT calculations when describing both, the geometry and electronic structure for a range of semiconductors and insulators.^{59,73–83}

The HSE06 has been shown to provide a good description of all polymorphs of TiO₂.^{59,84–90}

A geometry optimization was carried out on the fundamental anatase TiO₂ cell, allowing the lattice vectors, angles, volume, and atoms to relax until the forces on all the atoms were less than 0.01 eV atom⁻¹. In order to achieve an accurate merging of the total energy and electronic structure, a 700 eV plane wave energy cutoff and a Γ -centred 7 × 7 × 5 k-point lattice were used.

All the defect states calculated in this chapter were simulated using a 3 × 3 × 1 supercell containing 108 atoms using a Γ -centred k-point mesh of 2 × 2 × 2 combined with a plane wave cutoff of 450 eV. Only the ions within the supercells were allowed to relax with the lattice vectors whereas angles were kept immovable. All the defect calculations were spin-polarised, and the systems were deemed to be converged when the forces on all the atoms were less than 0.01 eV atom⁻¹. The limiting phases were calculated using plane-wave energy cutoffs of 700 eV and Γ -centred k-point meshes of 6 × 6 × 3 and 8 × 8 × 8 for B₂O₃ and Ti₂O₃ respectively.

2.3.1 Defect Formalism

The formation energy of a defect in charge state ‘q’ is defined as:

$$\Delta H_f(D, q) = (E^{D,q} - E^H) \pm \sum_i n_i E(E_i + \mu_i) + q(E_{Fermi} + \varepsilon_{VBM}^H + \Delta E_{pot}) + q^2 E_{corr}^{IC} + E_{corr}^{BF} \quad \text{Eq. 2.1}$$

$E^{D,q}$ and E^H refer to total energies of the defective cell in charge state 'q' and the host cell respectively. E_i refers to the elemental reference energy (where 'i' is Ti_(s), O_{2(g)} or B_(s)) and μ_i is the associated chemical potential. n refers to the number of electrons taken away from or added to the external reservoir. In this work the Fermi level (E_{Fermi}) ranges from the valence band maximum (VBM) (0 eV) to ~1.7 eV above the conduction band minimum (CBM). ε_{VBM}^H refers to the eigenvalue of the VBM in the host material and ΔE_{pot} corresponds to the correction that is applied to account for the difference between the potential of the host and the defective supercells. Two more corrections are applied to account for the finite size effects of the supercell; the first is an *image charge correction* E_{corr}^{IC} which corrects for the interaction of the charged defect and its own periodic images considering the long ranged nature of the Coulomb interaction.^{91,92} The *image charge correction* implemented herein uses the scheme formalised by Hine and Murphy⁹³ which utilises the dielectric tensor. Lastly there is a *band filling correction* (E_{corr}^{BF}) by Lany and Zunger^{94,95} which is applied to shallow defects to account for the high defect concentrations present in supercell calculations.

2.3.2 Chemical Potential Limits

The chemical potentials in **Equation 2.1** (μ_i) can reflect the equilibrium growth conditions which can then be varied to simulate the experimental partial pressures defining the extremes of *n*-type and *p*-type defect formation. Under equilibrium conditions the chemical potentials are relative to the formation enthalpy of anatase:

$$\mu_{Ti} + 2\mu_O = \Delta H_f^{TiO_2} = -9.14 \text{ eV}$$

Eq. 2.2

Due to the requirement that TiO₂ is to be thermodynamically stable towards Ti₂O₃, a further restraint is imposed on the chemical potentials making the *Ti-rich/O-poor* boundary limited by:

$$2\mu_{Ti} + 3\mu_O = \Delta H_f^{Ti_2O_3} = -14.76 \text{ eV}$$

Eq. 2.3

The obtained results positively compare with room-temperature experimental values (-9.73 eV and -15.76 eV for TiO₂ and Ti₂O₃ respectively⁹⁶).

This results in the 'extreme' set of growth conditions:

Ti-rich/O-poor (*n*-type favourable) where the chemical potentials are limited by the formation of Ti₂O₃:

$$\mu_{Ti} = -2.11 \text{ eV} ; \mu_O = -3.51 \text{ eV} \quad \text{Eq. 2.4}$$

And for *Ti-poor/O-rich* (*p*-type favourable) conditions where the chemical potentials are limited by the formation of O_{2(g)}:

$$\mu_{Ti} = -9.14 \text{ eV} ; \mu_O = 0 \text{ eV} \quad \text{Eq. 2.5}$$

To determine the solubility of the boron species, a limitation via the formation of a secondary phase, B₂O₃ is applied and is calculated to be:

$$2\mu_B + 3\mu_O = \Delta H_f^{B_2O_3} = -13.09 \text{ eV} \quad \text{Eq. 2.6}$$

(The experimental formation energy at room temperature is determined to be -13.20 eV⁹⁶)

Therefore, under *Ti-poor/O-rich* and *Ti-rich/O-poor* conditions $\mu_B = -6.55 \text{ eV}$; $\mu_B = -1.27 \text{ eV}$ respectively

Finally, the thermodynamic transition levels show the evolution of a defect from charge state *q* to *q'* at a certain Fermi level position, and they have been estimated by:

$$\varepsilon_D \frac{q}{q'} = \frac{\Delta H_f(D,q) - \Delta H_f(D,q')}{q' - q} \quad \text{Eq. 2.7}$$

Experimentally these transition levels can be seen by such techniques as deep level transient spectroscopy (DLTS).

2.4 Results and discussion

The results and the discussion presented here is based on the selection of the most representative samples for the selected experimental conditions. Previous to the final depositions, several depositions using different temperature and flow rates were performed, and no deposition or powdery deposition appeared. When the temperature of the bubbler containing boron isopropoxide was lower than 70 Celsius degree and the mixing chamber A lower than 200 Celsius degree, the deposition was not taking place. Only some areas where covered with TiO₂ but XPS didn't show B in these areas covered by the coating. When the optimal temperatures for the bubbler and the mixing chamber were found, the next parameter to experiment with was the flow rate of boron isopropoxide. When the flow rate was higher than 0.7 L·min⁻¹, *i. e.*, mostly powdery deposition on top of the glass was obtained.

Interstitial boron-doped TiO₂ thin films with various boron concentrations were produced by one-step APCVD. The concentration of boron in the films was controlled and increased by varying the temperature of the bubbler and the mass flow rate. The experimental parameters are given in Table 2.1. In all depositions, robust transparent thin films were deposited along the glass substrate (**Figure 2.2**). Nevertheless, upon the use of a high mass flow rate of boron, *i.e.* sample C, the as-synthesised thin-film was produced alongside a powdery deposition on top of some areas of the substrate (**Figure 2.4b and c**). The white powdery crystalline-like deposition was easily removed using water or acetone. This special case will be discussed in more detail below (**Figure 2.4**).

Sample	Mixing chamber A [K]	Mixing chamber B [K]	Ti Bubbler [K]	O Bubbler [K]	B Bubbler [K]	B Flow [L/min]
Undoped	N/A	523	340	312	N/A	N/A
Sample A	473	523	340	309	364	0.1
Sample B	473	523	340	311	363	0.3
Sample C	473	523	340	310	348	0.7

Table 2.1. Table of experimental parameters for the films deposition

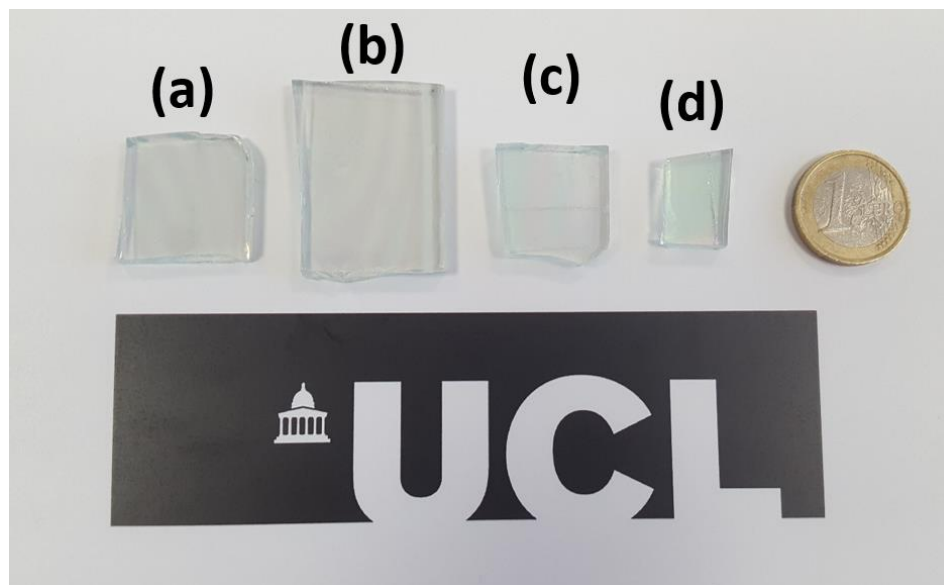


Figure 2.2. Photo of pieces of all thin films synthesised by APCVD: (a) undoped TiO₂ and B-TiO₂; (b) sample A; (c) sample B and (d) sample C.

2.4.1 Structure discussion

As previously mentioned in section 2.2, X-ray diffraction (XRD) and Raman spectroscopy analyses were used to determine the crystal structure of TiO₂ in all interstitial boron-doped TiO₂ and undoped thin films grown by APCVD (see **Figure 2.3**). The lattice parameters were determined from XRD patterns using a Le Bail model tool by GSAS, and compared with literature powder standards of anatase and rutile TiO₂⁹⁷

All as-synthesised thin films showed the presence of anatase TiO₂ crystal structure (**Figure 2.3a**). However, in the case of sample C, this B-TiO₂ film showed an additional peak at $2\theta = 27.7^\circ$, assigned to the presence of rutile TiO₂. Comparing peak counts, and based on the Le Bail fitting of the XRD data, tool by GSAS, it can be concluded that the rutile component accounts for around $\sim 15\%$ of this sample. As it can be seen, there are substantial differences in preferred growth, in particular, in the (103), (004), (112) and (211) planes (observed at approximately $2\theta = 36^\circ, 37^\circ, 38^\circ$ and 55° respectively).

Nevertheless, comparing functional properties of materials with varying concentrations of a dopant, grain sizes, and morphology is challenging. The

microstrain is known to potentially modify catalytic properties by changing the energy dispersion of specific states.⁹⁸

The microstrain can potentially modify the catalytic properties of TiO₂. Microstrain (LY) is defined in GSAS as:

$$S = 100\% \cdot \frac{\pi}{18000} \cdot LY ; LY = \sqrt{GU - GUI} \text{ "GU" accounts for the instrumental contribution.}$$

Extracted from XRD data, and accounted for any changes in LY(microstrain), the following table, table 2, shows the microstrain in all as-synthesised samples. Undoped TiO₂ and sample C showed no strain (LY = 0). Samples A and showed some strain.

Sample	LY		Strain (%)	
	Anatase	Rutile	Anatase	Rutile
Undoped	0	n/a	0	n/a
Sample A	16.7	n/a	0.29	n/a
Sample B	6.4	n/a	0.11	n/a
Sample C	0	0	0	0

Table 2.2. Microstrain (LY) calculated by Le Bail fitting (GSAS software), extracted from the XRD raw data of undoped and boron-doped samples.

The data showed that there is a low level of microstrain in sample A (0.29%) and B (0.11%). Hence the changes in the functional properties, which will be discussed in section 2.4.4, are due mostly to the doping levels and the grain morphology changes, induced as well for the doping levels, with a minor contribution of microstrain.

Raman spectroscopy was performed to confirm the presence of anatase, as well as the possible effect of boron in the spectra. **Figure 2.3b** shows the Raman spectra of all boron-doped TiO₂ thin films (samples A, B and C) and the spectrum of the undoped TiO₂ sample synthesised under the same conditions.

In all Raman spectra, characteristic vibrational bands for anatase were found, with a major contribution of the E_{g1} mode, found at ~144 cm⁻¹ in the undoped TiO₂ thin film synthesised by APCVD in one step.⁹⁹

As mentioned previously, thanks to the changes which the insertion of boron causes in the structure of anatase TiO₂, specially in the characteristic band (E_g), a shifting could be observed. In **Figure 2.3c**, can be observed a closer view of the characteristic E_{g1} vibrational band of anatase. In the case of boron-doped samples B and C, no significant shifting was observed. However, in the case of sample A, when comparing the position of the main peak to the one of the undoped TiO₂ sample, B-TiO₂ (A) showed a shift, the E_g band was found at ~149 cm⁻¹. The shifting of this band in TiO₂, when doping with foreign elements, has been previously observed and reported.^{100,101} The shifting will be discussed more in detail below.

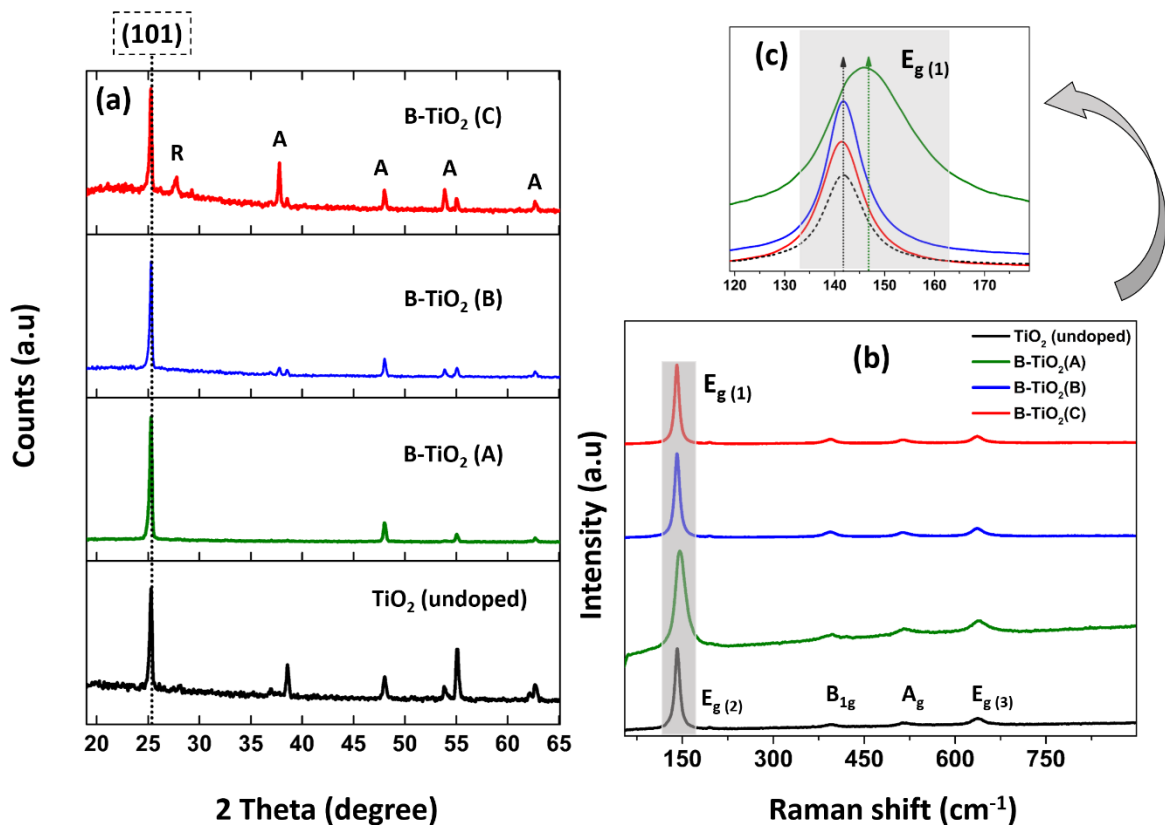


Figure 2.3. XRD patterns of B-TiO₂ thin films and an undoped TiO₂ sample (A = anatase and R = rutile); (b) Raman spectra of the B-TiO₂ samples, compared to the undoped anatase film and (c) Raman shift of the E_g band zoomed. Black dotted arrow (left) indicates the position of the undoped TiO₂ and dotted green arrow (right) the position of the E_g band for B-TiO₂: (A).

As previously mentioned, the use of Le Bail refinement allowed us to investigate the average crystal size of the different as-synthesised thin films, investigated in this chapter (**Table 2.3**). It was found that samples A and B showed average crystal sizes approximately double than that of undoped TiO₂ thin films.

XRD analysis showed that the B-TiO₂ samples consisted of anatase TiO₂, and also suggested the addition of the boron dopant in an interstitial position. Indeed, the lattice parameter *c* (**Table 2.3**) of B-TiO₂, was shown to be larger than the ones of the reference TiO₂ sample. Surprisingly, the unit cell volume in sample B was similar to the undoped TiO₂ film synthesised under the same conditions. The extension of the *c*-axis and the expansion of the unit cell volume, except for sample B, can be explained by the interstitial incorporation of boron in the TiO₂ lattice.^{45, 64}

As previously mentioned, the use of high amounts of the boron dopant resulted in the presence of a white powdery coating covering certain areas of the substrate glass. These certain areas of sample B-TiO₂ (C) were analysed by scratching the powdery coatings and investigating them using XRD analysis (**Figure 2.4a**). The collected XRD pattern of the powder matched with a mixture of two crystalline phases, anatase and a crystalline form of boric acid known as “sassolite”. Sassolite (H₃BO₃) is placed within the triclinic – pinacoidal crystal classification system and appears as colourless or white pseudo-hexagonal crystals.⁴⁰

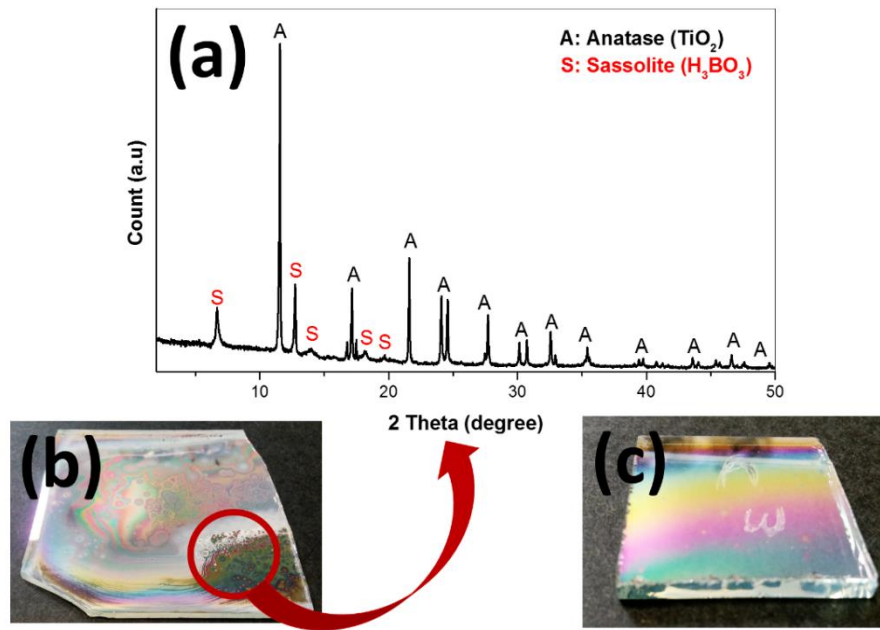


Figure 2.4. (a) X-ray diffraction pattern of the powdery section in sample B-TiO₂ (C); (b) photograph of sample B-TiO₂ (C) with powdery deposition on top; (c) Photograph of sample B-TiO₂ (C) without powdery deposition on top.

The presence of boric acid (sassolite), as a by-product, during the synthesis of the films (specifically for sample C) could explain why the increase of the average crystal size of TiO₂ was not as noticeable as in the case of the other samples. This is probably because of changes in the pH of the mixture of components in the gas phase making the solubility of TiO₂ nanoparticles and the nucleation rates susceptible to change. As previously reported by Sabyrov *et al.*,¹⁰² the generation of smaller initial nanoparticles of anatase TiO₂ in acidic conditions and at high temperatures increased and induced the phase transformation rate of rutile TiO₂. The rutile phase found in sample C could be attributed to this effect. In addition, it is worth mentioning that this effect was previously observed during the synthesis of S-doped TiO₂ films. Pore *et al.*¹⁰³ reported a similar effect for the synthesis of S-TiO₂ films, using atomic layer deposition (ALD) methods. In this work, the authors found that sulfur had a large impact on the TiO₂ growth, inducing the presence of a rutile crystal phase.

The as-synthesised samples were also investigated using Raman spectroscopy, which also corroborated the presence of the pure anatase TiO₂ phase in all B-

TiO₂ thin films.⁹⁷ It can be observed in **Figure 2.3c** that no shifting of the band E_g could be observed for samples B and C, whereas sample A showed a blue shift. This blue shift means that frequency of phonons interacting with the incident photon increased.¹⁰⁴

Sample	phase	a [Å]	b [Å]	c [Å]	V [Å ³]	τ (nm)	[B] (atom %)
Standards	anatase	3.7848	3.7848	9.5124	136.26	-	N/A
	rutile	4.5941	4.5941	2.9589	62.45	-	
Undoped	anatase	3.7885	3.7885	9.5205	136.13	44.63	0.0
B-TiO₂ (A)	anatase	3.7832	3.7832	9.5322	137.65	87.43	0.8-1.0
B-TiO₂ (B)	anatase	3.7811	3.7811	9.5087	135.94	79.51	2-3.0
B-TiO₂ (C)	anatase	3.8003	3.8003	9.5361	137.72	50.26	4-5.0
	rutile	4.5298	4.5298	2.9598	60.73	31.21	

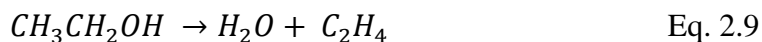
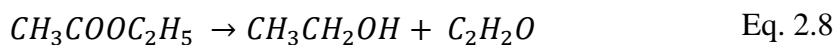
Table 2.3. Cell parameters and boron atomic concentration of the undoped and B-TiO₂ thin films in comparison to powder standards of anatase and rutile.

Additionally, as observed below and discussed in section 2.3.2, in **Table 2.3**, samples A and B showed relatively low doping levels of boron (between 1 and 3 % at.), whereas sample C presented the highest doping levels (between 4 and 5 % at.).

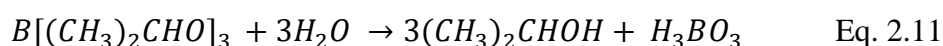
Therefore, by combining the data obtained by XRD, Raman spectroscopy and XPS studies (see below) it could be summarised that: (i) boron has been doped within the anatase phase interstitially (ii) when the mass flow of the dopant is too high the rutile phase appears and a powdery phase-mixture of TiO₂ and H₃BO₃ (sassolite) was deposited along with the film as by-products, which can be found in some areas of the substrate (glass).

A possible mechanism for the formation TiO₂ from the reaction of TiCl₄ and ethyl acetate was previously described by Evans *et. al.*¹⁰⁵ This involves the ethyl acetate first decomposing to produce oxidant species such as ethanol (**Equation 2.8**), which in turn dehydrates evolving water and ethane (**Equation 2.9**). With

water present, the surface reaction may proceed by a simple hydrolysis reaction with TiCl₄ (**Equation 2.10**):



In the case of the boron doped TiO₂ films formed herein, the formation of boric acid was observed, which may be produced from the reaction of triisopropyl borate and water – formed from the breakdown of ethyl acetate:



Therefore, boron doping in TiO₂ likely occurs from the reaction of boric acid and TiCl₄ or *via* a direct reaction of triisopropyl borate and TiCl₄.

2.4.2 Boron doping

XPS and D-SIMS analyses were performed to study the presence of boron in the films and elucidate its position within the TiO₂ lattice, The Ti 2*p* peaks, located at binding energies of 458.9 eV and 464.6 eV were identified as Ti-O bonds of Ti⁴⁺ in TiO₂.¹⁰⁶ No other Ti⁴⁺ environment or reduced Ti³⁺ species were detected in samples A and B (**Figure 2.5a and b**). Nevertheless, in the case of sample C, a small peak at ~ 457 eV appeared and was attributed to the presence of reduced Ti³⁺ on the surface (**Figure 2.5c**). It has been also suggested that boron in interstitial site reduces Ti⁴⁺ to Ti³⁺ to facilitate separation of photoexcited electron and hole pairs and slow down their recombination.²⁵ Recently, it was shown by N. Patel *et al.*⁴⁵ that when synthesising B-TiO₂ powders at a concentration of ~ 1% at. of B, experimentally, Ti³⁺ was observed by XPS. Surprisingly, in the films described in this thesis, no signal of Ti³⁺ on the surface was detected in the thin B-TiO₂ films unless a concentration of B ~ 5% at. of was achieved (sample C). The O 1*s* peak, located at 530.4 eV, is also consistent with the formation of TiO₂.

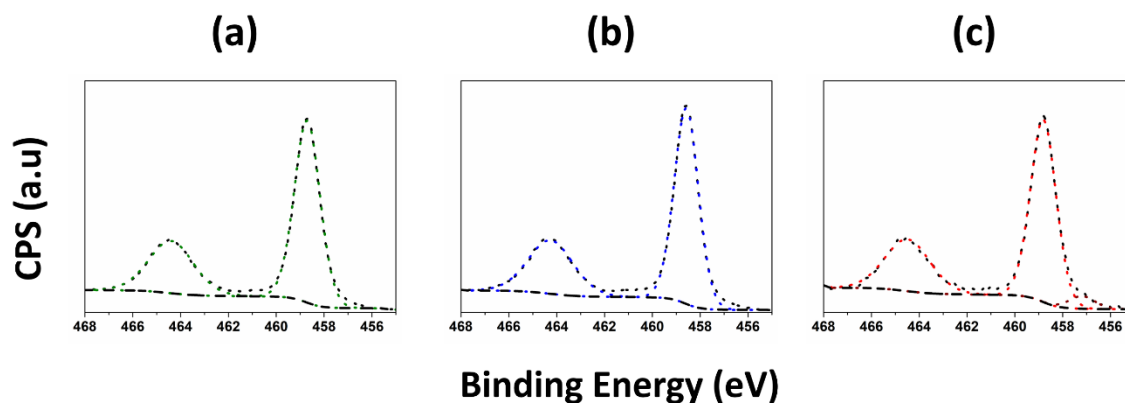


Figure 2.5. Ti 2p environment surface XPS spectra of boron-doped TiO₂ thin films: (a) sample A, (b) Sample B and (c) sample C. Black dashed lines represent the background; black dotted lines represent the experimental raw CPS data; colourful dotted lines (green, blue, red and dark red) represent the fitted components for Ti 2p environments.

The total boron concentration of the B-TiO₂ films was found to be in the range of 1-5 at.%. However, the assignment of the chemical environment of boron has been a constant source of debate in the literature.^{25,42,45,63} It has been commonly acknowledged that B 1s peaks at 190–191 eV are attributed to substitutional boron which replaces oxygen sites (B_o) and peaks in the range 191–192 eV correspond to interstitial boron (B_i).¹⁰⁷ Boron can also be found in various other forms, including cationic B³⁺ in B₂O₃ and anionic B²⁻ in TiB₂, with a characteristic B 1s peak lying at 193.1 eV and 187.5 eV respectively.^{63,107} It can be observed in **Figure 2.6** that the XPS (**Figure 2.6 and 2.7**) and D-SIMS data (**Figure 2.8**) data showed the presence of boron both in the surface and through the bulk (in-depth profile) in all as-synthesised thin films.

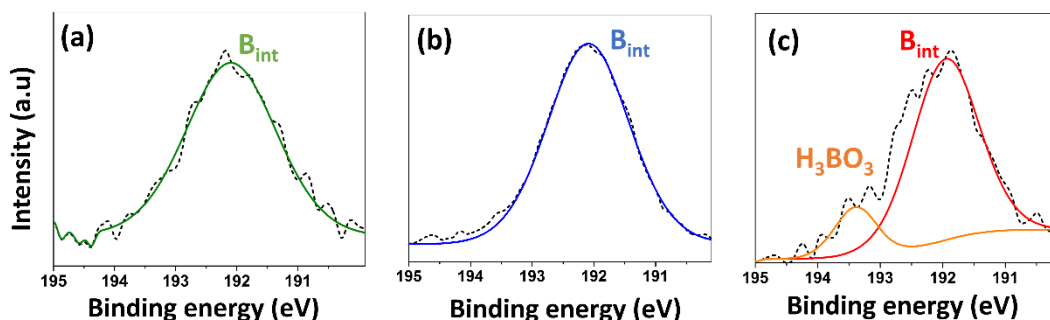


Figure 2.6. B 1s XPS Surface spectra of B-TiO₂ samples: (a) B-TiO₂ (A); (b) B-TiO₂ (B) and (c) B-TiO₂ (C); Dashed black lines represent the raw data (CPS) in XPS.

The surface XPS data was analysed and deconvoluted (**Figure 2.6a, b & c**), showing the presence of the B 1s environment located between 191.6-192 eV, at 191.8 eV, 192 eV and 191.5 eV for samples A, B & C respectively. These peaks were attributed to interstitial boron (B_i). In addition, a small peak at 193.5 eV (**Figure 2.6c**) can be clearly observed, which could be attributed to the presence of boric acid on the surface of the B-TiO₂ thin films. This phenomenon has been previously observed and described.⁶⁴ The XPS of sample C supports the data extracted from XRD of the powdery deposition found on some areas of the B-TiO₂ film, by showing the presence of H₃BO₃ (sassolite) chemical environment. Depth profile XPS analysis showed the presence of a single B environment, located at ~191.7 eV, which could be exclusively attributed to interstitial boron. Therefore, it could be concluded that H₃BO₃ species were only present, as a by-product, at certain areas of the surface of sample C, and it may appear due to the gas phase reaction process, as described above (**Equation 2.11**). A depth profile D-SIMS study was also performed (**Figure 2.8**), corroborating the presence of boron not only in the surface but also within the bulk. Throughout the film, both the titanium and oxygen levels were constant, whereas the boron doping level varied somewhat.

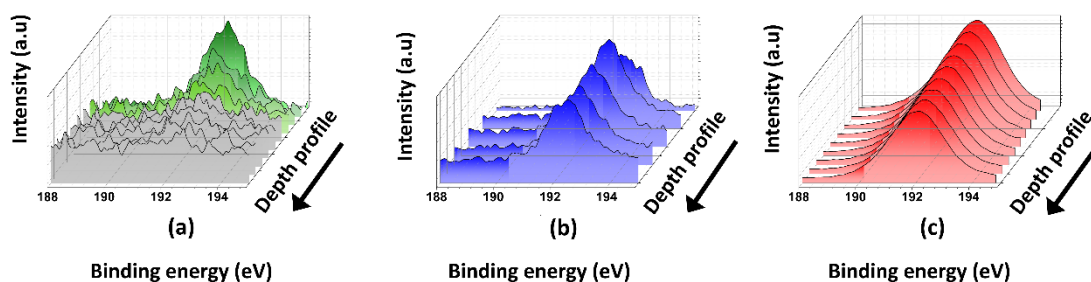


Figure 2.7. B 1s XPS depth profiling spectra of: (a) B-TiO₂ (A); (b) B-TiO₂ (B) and (c) B-TiO₂ (C) thin films.

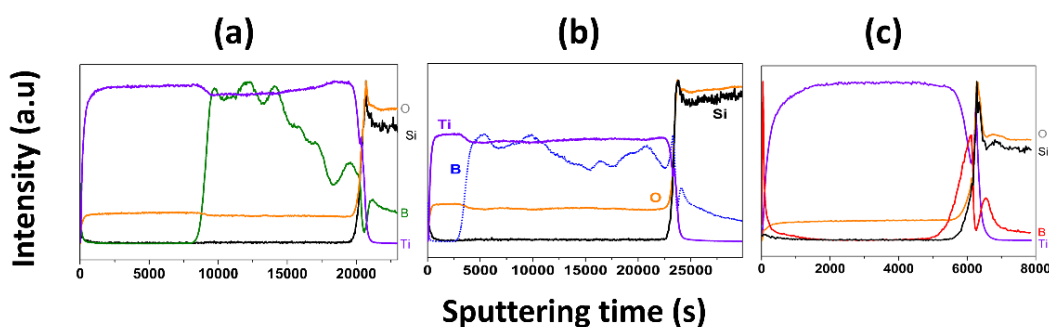


Figure 2.8. In depth D-SIMS spectra: (a) sample B-TiO₂ (A); (b) sample B-TiO₂ (B); (c) B-TiO₂ (C); green, blue and red lines, represent the signal for B obtained when bombarding (sputtering) the samples A, B and C with Cs⁺ ions, respectively.

The stability and lifetime of the interstitial boron dopant, used in this chapter, within the TiO₂ structure was demonstrated by the XPS analysis. Sequential XPS tests were carried out in the same position of sample B-TiO₂ (C) before and after the photocatalytic tests. XPS surface analysis showed a stable concentration of boron (ca. 4% at..) in the coating surface, even after sequential cleaning steps (repeated after every photocatalytic test performed, three total tests, **Figure 2.9**) using chloroform and UVA light (365 nm) irradiation during 48 h. In addition, the core-level of the B 1s environment (**Figure 2.6a and b**) revealed, after deconvolution, a dominant peak at 191.7 eV, which could be assigned to the interstitial boron (placed between 191-192 eV), according to different works previously reported in the literature.^{43,45} It is worth noting that the peak assigned to B₂O₃ completely disappears, upon comparison of the core-level of the B 1s

environment before and after the photocatalytic test (**Figure 2.6c**). This effect was also observed for boric acid present in the B-TiO₂ thin films. This could be attributed to the dissipation of both species during the cleaning process. Therefore, the cycling of the B-TiO₂ thin films could be corroborated by the XPS results, the constant photocatalytic performance and the unaltered thin film morphology after the stearic acid degradation test. This stability of interstitial occupancy of boron in the TiO₂ lattice vs substitutional has been reported and studied previously.^{45,64}

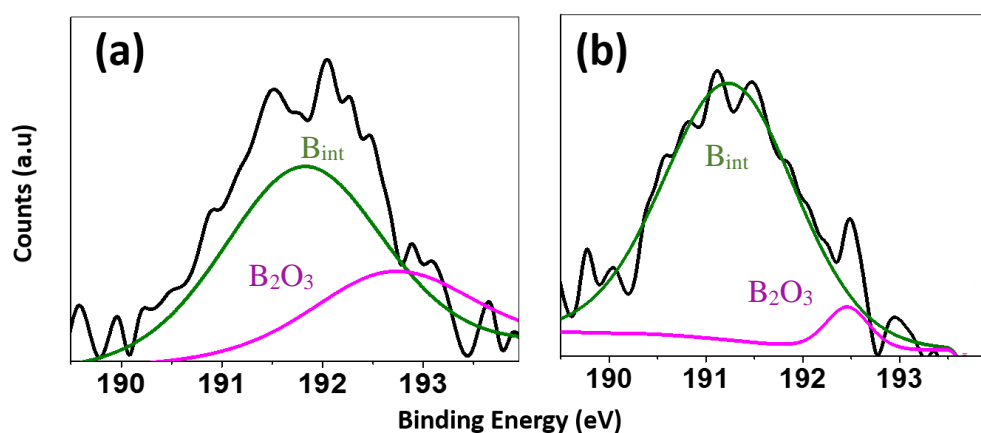


Figure 2.9. B 1s XPS spectra after the second (a) and third (b) run of the photocatalytic test with SA and cleaning of the samples, respectively.

2.4.3 Morphology of the films

The morphological structure of the thin films was studied using Scanning Electron Microscopy (SEM). All different B-TiO₂ thin films deposited in this chapter showed a varying morphology (**Figure 2.10**), which could be attributed to the different level of boron doping observed in the different as-synthesised thin films.

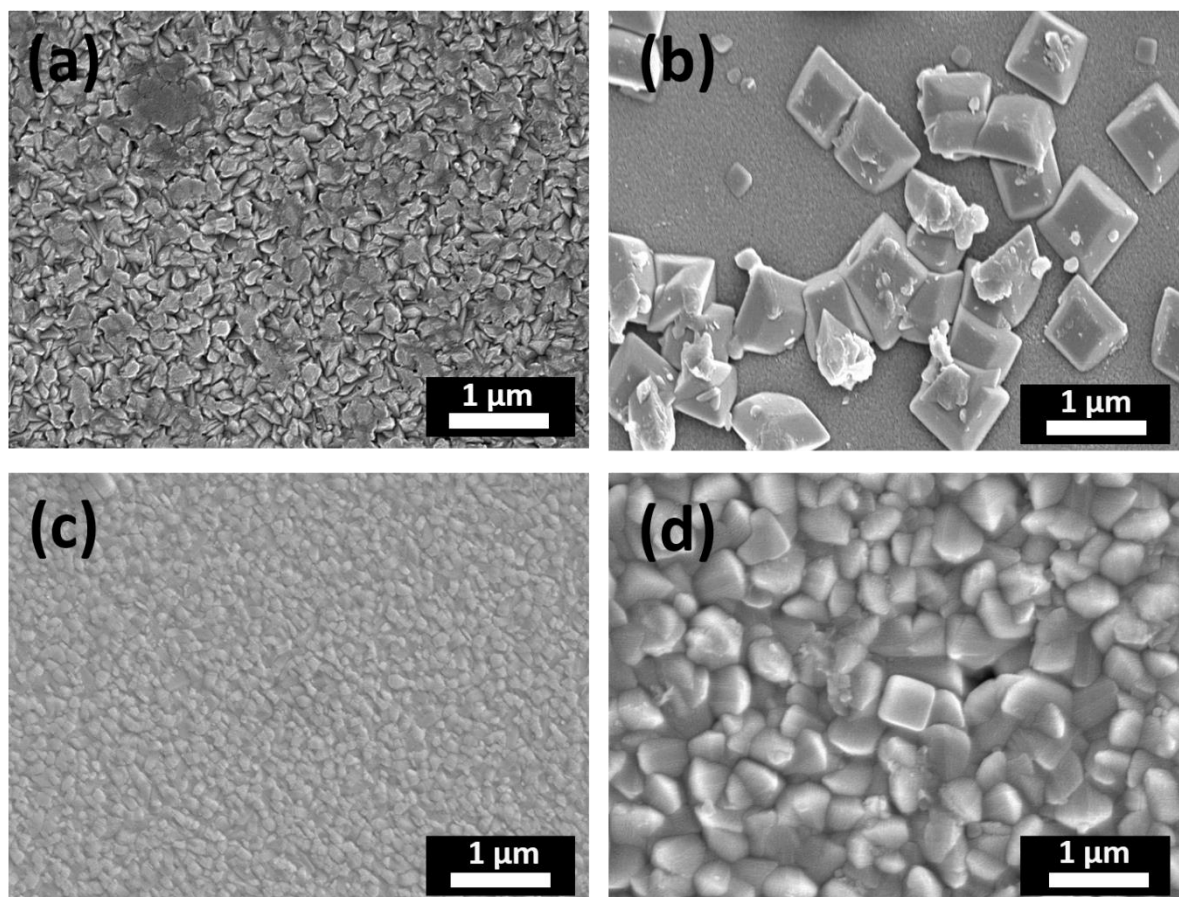


Figure 2.10. SEM images (top view) of: (a) Undoped TiO₂, (b) B-TiO₂ (A), (c) B-TiO₂ (B) and (d) B-TiO₂ (C).

SEM studies clearly showed a different morphology between all as-synthesised boron-doped and undoped TiO₂ thin films (**Figure 2.10**), used in this chapter. In addition, it is worth mentioning that SEM analysis of the B-TiO₂ samples revealed the presence of 3 different morphologies which correspond to the macroscopic aspect variation observed on the substrate. A typical SEM image of the undoped TiO₂ film showed well defined shell-shaped aggregated particles, with sizes ranging from 120 nm to 230 nm. However, there was a significantly larger average particle size when B was added to the lattice of TiO₂ (i.e. 290 nm to 500 nm). This effect can be clearly observed in **Figure 2.10b**, where sample A showed agglomerations of big particles (ca. 1 μm to 2.3 μm) with a more defined prism-like and cubic shape deposited on top of a uniform coating of smaller agglomerations of particles. Both type of deposited particles were well adhered

to the substrate forming a bilayer-like structure of B-TiO₂ as reported previously.⁶⁴ In contrast, sample B and C showed smaller particle size, where sample B exhibited a well-defined and uniform film composed of cubic-shaped particles (ca. 160 nm) and sample C (**Figure 2.10d**) showed prism-shaped and well aggregated particles with sizes in the range of 290 nm to 500 nm. Comparing the different surface morphologies of B-TiO₂ with that of undoped TiO₂ film (**Figure 2.10**), the final concentration of boron incorporation has a significant role in the agglomeration of the doped-TiO₂ nanoparticles along the substrate.

Further morphological studies of the as-synthesised thin films were carried out by using SEM cross-section analyses (**Figure 2.11**). This study showed that both the undoped and boron-doped TiO₂ thin films described in this work were relatively hard and strongly adhered along the entirety of the glass substrate. It can be clearly observed in **Figure 2.11** that sample A was comprised of a the multilayer-like morphology, where agglomerations of larger particles of B-TiO₂ (cubic shape) can be found on top of a uniform layer of smaller particles. The thicknesses of the films were found to be in the range between 420 nm and 650 nm.⁶⁴

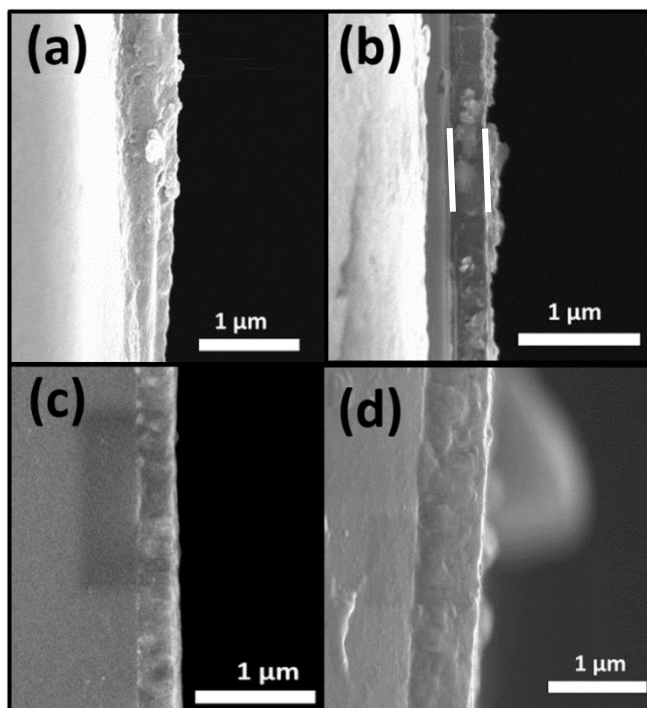


Figure 2.11. Cross-section SEM images of the undoped and B-TiO₂ samples: (a) undoped TiO₂; (b) B-TiO₂ (A); (c) B-TiO₂ (B); (d) B-TiO₂ (C).

Apart from the SEM images, preliminary macroscopic observations of the boron-doped thin films, especially in the case of sample A, under tilt angle, showed undoubted differences in the surface of the samples when compared to the undoped TiO₂ thin-film (**Figure 2.12a and d**). The undoped TiO₂ coating exhibits different lines of interference colours, expressing thickness differences along the length of the substrate (**Figure 2.12d**). On the other hand, a combination of these lines and concentric circles of interference colours were observed on the B-TiO₂ thin film (**Figure 2.12a**). SEM observations confirm the existence of morphology discrepancies between the B-TiO₂ (**Figure 2.12b and c**) and TiO₂ coatings (**Figure 2.12e**). In addition, SEM analyses of the B-TiO₂ sample revealed the presence of two different morphologies, which correspond to the macroscopic aspect variation shown in **Figure 2.12a**. **Figure 2.12b** shows prism-shaped and well aggregated particles with sizes in the range of 290 to 500 nm, whereas the agglomerations of bigger particles (ca. 1 μm to 2.3 μm) with a more defined prism-like and cubic shape, deposited on top of a uniform coating with smaller

agglomerations of particles, were observed in the concentric circles zones (**Figure 2.12c**). When comparing the two different surface morphologies identified on the boron-doped TiO₂ film (**Figure 2.12b and c**) with the surface morphology of the undoped TiO₂ film (**Figure 2.12e**) deposited under the same conditions, the effect of the addition of the boron precursor on the morphology of the films is obvious. Indeed, the typical SEM image of the TiO₂ film shows shell-shaped aggregated particles with sizes in the range from 120 to 230 nm, which contrasts with the significantly larger average particle size of the B-TiO₂ sample (i.e. 290 to 500 nm). The formation of concentric circles might be explained due to zones where the gas phase reaction between precursors was prevailing along the glass substrate and the 3D growth of clusters is promoted as the reaction take place more in the gas phase than directly on top of the substrate (2D growth).

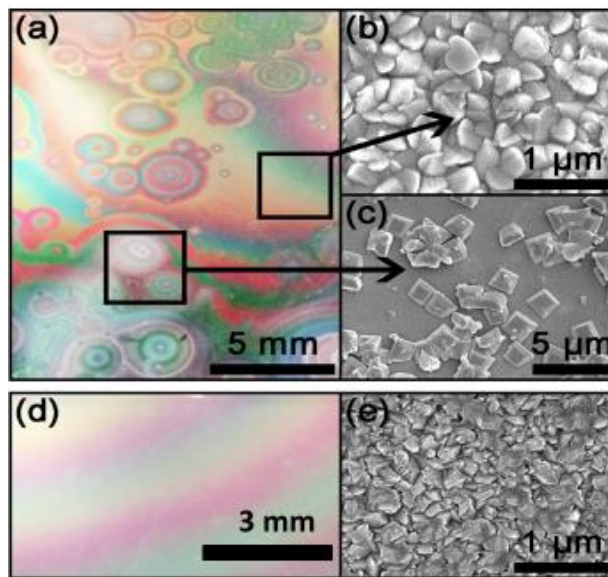


Figure 2.12. (a) Optical image with a tilt angle of the B-TiO₂ thin film on glass and (b and c) the corresponding SEM images from two different areas identified on the B-TiO₂ thin film, and (d) optical image of the undoped TiO₂ and (e) its SEM capture.

2.4.4 Functional properties of the films

With the purpose of utilizing a wider range of the solar spectrum in the photocatalytic application of TiO₂, the role of nonmetal elements in modifying the optical properties of TiO₂ has been the subject of extensive work in the past few years.^{26,39}

The use of cationic dopants with a higher oxidation state than Ti⁴⁺ do not reduce the visible light response of anatase TiO₂. Instead, they act as electron donors, injecting electrons into the conduction band, and can transform anatase into a transparent conducting oxide (TCO).²⁹

This transformation normally occurs with a blue shift of the optical absorption and a dramatic reduction in resistivity, with typical donor dopants being Nb, Ta, and W.^{29,59,108} The use of TiO₂-based materials for TCO applications presents advantages compared to indium-based TCO materials, such as high refractive index, high transmittance in the infrared region, and high chemical stability as well as a significant reduction in the production cost.⁵⁹

In this chapter, the undoped TiO₂ thin films displayed high optical transparency. The incorporation of low B concentrations (sample A, ~1 atom %) resulted in films with zones of concentric circles on the substrate evidenced by a red shift transmission (~316nm to 348nm) compared to the undoped TiO₂ thin films (**Figure 2.13a**). Tauc plot analysis (**Figure 2.13b**) showed a slight shift in absorption into the blue region for these TiO₂ samples, with band gap energies estimated around 3.28 eV compared to the experimental value for undoped films (~3.45 eV). Surprisingly, highly doped B films (Samples B and C) showed a smaller shift and the corresponding band gap energies, 3.36 and 3.43 eV respectively, were comparable with the values for undoped TiO₂.

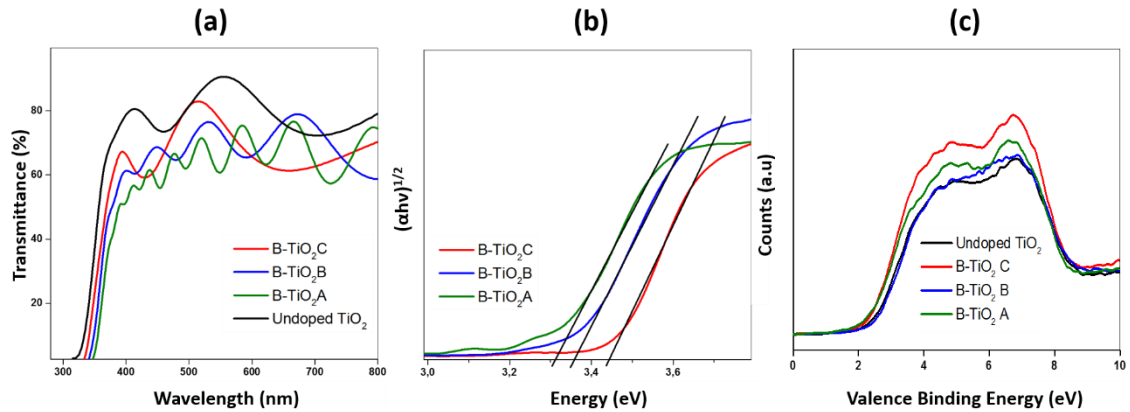


Figure 2.13. (a) UV-visible spectra (transmittance) of the doped and undoped TiO₂ films, (b) graphical calculation (Tauc plot) of the optical band gap for all the boron-doped TiO₂ samples and (c) XPS valence band spectra of the doped samples as compared to the undoped.

These results are similar to phosphorus doped TiO₂ thin films by C. Sotelo-Vazquez *et al.*,¹⁰⁹ where it was reported a small shift (blue shift in their case) when the concentration of the dopant (phosphorus) was lower than 1% at., and no noticeable shift occurs when the concentration was higher than 1 at.%. Valence band XPS (VB-XPS) shows the valence band edge relative to the Fermi level for the undoped and boron-doped TiO₂ samples (**Figure 2.13c**), corroborating the band gap shifts. It was found that sample B had a spectral line shape similar to undoped TiO₂. Therefore, it could be assumed that sample B (~2-3 atom % B) did not show a change in the optical properties compared to that of the undoped film. In contrast, samples A and C, showed similar line shapes with a decrease in the band gap.

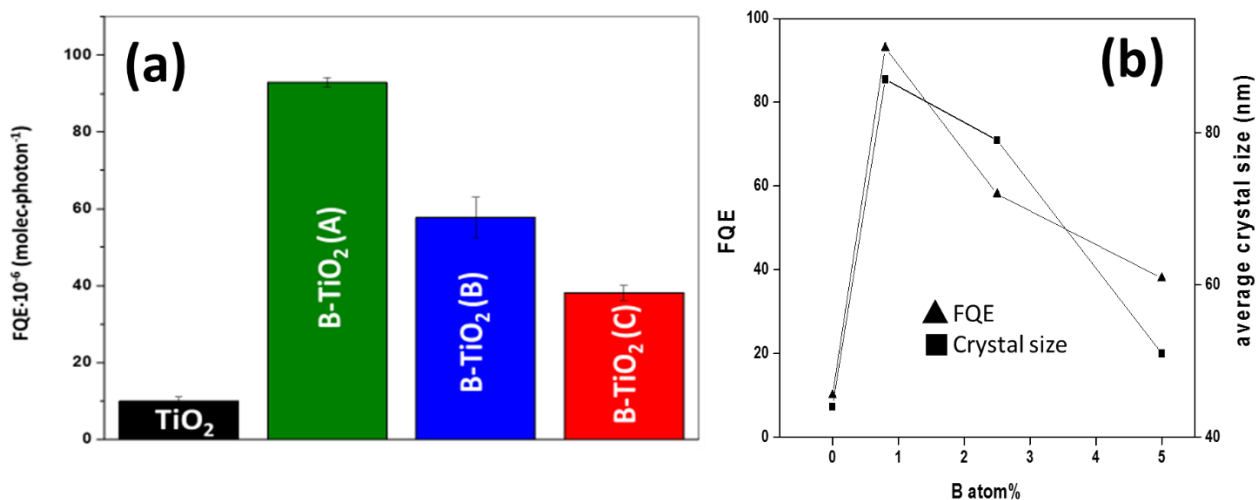


Figure 2.14. (a) Average Formal quantum efficiencies (FQE) obtained during photodegradation of stearic acid under UVA irradiation of selected B-TiO₂ films and undoped TiO₂ film, used as reference; (b) graphic representation of the evolution/relation between the B atom concentration versus the photoactivity (FQE) and average crystal size of the TiO₂ and B-TiO₂ films.

To investigate the influence of boron doping on the photocatalytic properties of TiO₂, tests were performed and evaluated on the degradation of stearic acid under UVA irradiation (2 mW·cm⁻²).¹¹⁰ The increased crystallinity of the B-TiO₂ samples, induced by the interstitial incorporation of boron, contributes to superior functional properties of the film in comparison to undoped TiO₂.^{45,63,64} The photocatalytic degradation of stearic acid (CH₃(CH₂)₁₆CO₂H) was recorded using FTIR, following the disappearance of characteristic C–H modes of the acid (2958 cm⁻¹, 2923 cm⁻¹, and 2853 cm⁻¹). The photocatalytic rates were estimated from a linear regression of the initial steps (30–40%) of the curve of the integrated area vs illumination time.¹¹⁰ In **Figure 2.14a**, the corresponding rates were expressed as formal quantum efficiencies (FQE) defined as molecules of stearic acid degraded over incident photons (molecule/photon).

Figure 2.14a shows a bar chart of the FQEs in the photocatalytic degradation of stearic acid, under UV light (~365 nm). All the B-TiO₂ samples showed higher photocatalytic activities in comparison to undoped anatase with the highest presented in sample A. As the incorporation of boron increases the photocatalytic activity of the samples decreases. There is a correlation between the

concentration of interstitial boron within the film and the average crystalline size, as seen by XRD (**Table 2.3**). From our results, higher photocatalytic activity is attainable when the incorporation of boron is ~1% at. and is exclusively interstitial, and when the B-TiO₂ nanoparticles agglomerate resulting in bigger particles. The conductivity of the doped films were analysed using a Hall Effect probe and are displayed in **Table 2.3**.

Sample	Hall effect probe			Resistance ^(*)
	n (cm ⁻³)	μ (cm ² V ⁻¹ s ⁻¹)	ρ (Ω cm)	R (KΩ)
B-TiO ₂ (A)	-3.24 x 10 ¹⁵	172.40	112	150
B-TiO ₂ (B)	-3.82 x 10 ¹⁷	8.17	20	90
B-TiO ₂ (C)	-9 x 10 ¹³	0.08	9.5 x 10 ⁵	120
Nb:TiO ₂ ^(*)	-8.3 x 10 ¹⁸	3.4	0.22	--
F:TiO ₂ ^(*)	-46	26	5.2	--

Table 2.4. Data extracted from the Hall Effect Electrical Measurements. (*) Data collected from reference 78.

As the resistivity was close to the detection limits that can be measured by the Hall Effect device, the derived charge carrier densities and mobilities were liable to have large associated errors. A high resistivity and small range of mobility of the charge carriers was measured. It was found that the lowest resistivity was found for Sample B (20 Ω cm), whilst the highest was for Sample C (9.5 x 10⁵ Ω cm). Comparing these values to Nb:TiO₂ and F:TiO₂, the measured values of resistance (ρ) for B-TiO₂ are much higher. *Ab-initio* DFT calculations were carried out to aide the understanding of the functional properties of B-TiO₂.

2.4.5 Defect Thermodynamics:

As described previously in **section 2.3**, to explain more in detail the experimental results and to find an explanation for the origin of such multifunctionality which interstitial boron-doped TiO₂ films showed, theoretical calculations based on all the experimental data collected were carried out. Dr David O. Scanlon and Mr Benjamin A. D. Williamson are acknowledged for the elaboration of the theoretical calculations as well as for further discussion in the interpretation of the experimental data.

2.4.5.1 Bulk electronic properties:

The density of states (DoS) and band structure for anatase TiO₂ are presented in **Figure 2.15a and b** respectively. The DoS shows that the VBM is predominantly made up of O *2p* states mixed with some negligible Ti *p* and *d* states. On the other hand, the CBM is mostly made up of Ti *d* states alongside a minimal amount of O states. These results are consistent with other DFT calculations on TiO₂ polymorphs.^{86,111} **Figure 2.15b** shows that anatase is an indirect band gap material ($E_g^{\text{ind}} = 3.35$ eV) with the VBM occurring at the X high symmetry point and the CBM at Γ . The direct band gap at Γ has a magnitude of 3.64 eV. These results are consistent with other theoretical calculations using HSE06,^{112,113} however the consensus in experiment places the band gap at ~3.2 eV.⁸⁶ Higher levels of theory such as the GW (Green's function) approximation which place the band gap around 3.6-3.8 eV,¹¹⁴⁻¹¹⁷ the overestimation is generally thought to be excitonic effects or the difficulties in the convergence of the screened interaction of localized systems.¹¹⁵⁻¹¹⁷

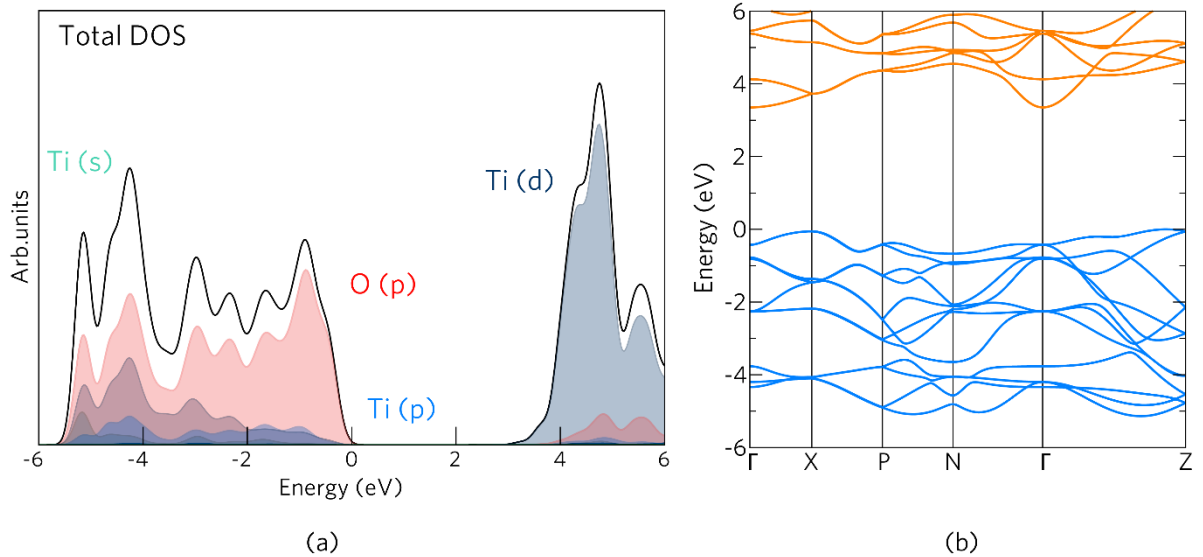


Figure 2.15. The calculated density of states (DoS) (a) and band structure (b) of undoped anatase TiO_2 . In each diagram the valence band maximum (VBM) is set to 0 eV. In (b) the valence bands are depicted as blue lines and the conduction bands as orange lines.

2.4.5.2 Defects:

The transition level diagrams for boron-doped TiO_2 under both *Ti-rich/O-poor* and *Ti-poor/O-rich* conditions (**Figure 2.16**) will be described in this section.

Intrinsic defects:

Previous theoretical studies have shown that the dominant acceptor and donor defects in anatase are the titanium vacancy (V_{Ti}) and the oxygen vacancy (V_{O}).^{88,90,118–121} Under *Ti-rich/O-poor* conditions, V_{O} acts as a *resonant donor* with a low formation energy (for V_{O}^0 , $\Delta H_{\text{f}} = \sim 1.19$ eV) with the 2+ charge state dominant across the entirety of the band gap. This is in contrast to most wide band gap binary oxides such as ZnO ,^{76,122–124} SnO_2 ,^{124–127} In_2O_3 ,^{84,124,128–131} and BaSnO_3 ¹³² where V_{O} is a “negative-U” defect modulating from the 2+ to

the neutral charge state in the band gap. Under *Ti-poor/O-rich* conditions, V_o has a higher formation energy ($\Delta H_f = \sim 4.71$ eV). These results are consistent with other theoretical studies carried out on anatase.^{90,118,133,134}

V_{Ti} is a *deep* acceptor under both growth regimes with the 1-/0 transition level occurring at ~ 0.87 eV above the VBM. The formation energies of the neutral charge state occur at ~ 14.26 eV and ~ 7.23 eV for *Ti-rich/O-poor* and *Ti-poor/O-rich* conditions respectively, meaning that the formation of V_{Ti} near the VBM is highly unfavorable and will be seen in negligible quantities. Under *Ti-poor/O-rich* conditions (*p*-type favourable), V_{Ti}^{4-} begins compensating the donor defects ~ 2.28 eV above the VBM. Our calculations show that all charge states of V_{Ti} are shown in the band gap. Multiple pictures of V_{Ti} are seen in the theoretical literature on anatase. Phattalung et al.¹³⁵ found using LDA (Local Density Approximation) that V_{Ti} is a quadruple *shallow* acceptor, however, LDA is known to be inadequate in describing the band gap and correct localization of holes and electrons. Applying a Hubbard-like “U” value (which incorporates an occupation penalty scheme), Morgan et al. show that V_{Ti} is a *deep* acceptor (2-/0 transition occurs ~ 0.85 eV above the VBM). In this study, however, it is shown that there is no 0/1- transition level and the formation energy is ~ 2.5 eV lower than that calculated from our calculations.^{118,121} The only HSE06 calculations on V_{Ti} in anatase show that the defect transitions from the neutral charge state to the 2- then the 4- charge state over the band gap. In these calculations, only a Monkhorst-Pack 1x1x1 k-point sampling was used which can lead to inaccurate total energies and therefore the thermodynamic picture of the defects.⁹⁰

It is known that the thermodynamic transition levels can be sensitive to the correct localization and delocalization of electrons and holes and **Figure 2.17** presents the calculated partial charge densities of each charge state of V_{Ti} displaying the correct localization of holes on the adjacent oxygens surrounding the vacancy. The axial holes are the first to be removed (V_{Ti}^{1-} and V_{Ti}^{2-} which are depicted as p_y orbitals) and then the equatorial holes (V_{Ti}^{3-} and V_{Ti}^{4-} depicted as p_z orbitals). This correct localization is important and we have shown this to be as important in ZnO.¹³⁶

Previous theoretical studies have shown that the dominant acceptor and donor defects in anatase are the titanium vacancy (V_{Ti}) and the oxygen vacancy

(V_O).^{88,90,118–121} Under *Ti-rich/O-poor* conditions, V_O acts as a *resonant donor* with a low formation energy (for V_O⁰, ΔH_f = ~1.19 eV) with the 2+ charge state dominant across the entirety of the band gap. This is in contrast to most wide band gap binary oxides such as ZnO,^{76,122–124} SnO₂,^{124–127} In₂O₃,^{84,124,128–131} and BaSnO₃¹³² where V_O is a “negative-U” defect modulating from the 2+ to the neutral charge state in the band gap. Under

Ti-poor/O-rich conditions, V_O has a higher formation energy (ΔH_f = ~4.71 eV). These results are consistent with other theoretical studies carried out on anatase.^{90,118,133,134}

V_{Ti} is a *deep* acceptor under both growth regimes with the 1-/0 transition level occurring at ~0.87 eV above the VBM. The formation energies of the neutral charge state occur at ~14.26 eV and ~7.23 eV for *Ti-rich/O-poor* and *Ti-poor/O-rich* conditions respectively, meaning that the formation of V_{Ti} near the VBM is highly unfavorable and will be seen in negligible quantities. Under *Ti-poor/O-rich* conditions (*p*-type favourable), V_{Ti}⁴⁺ begins compensating the donor defects ~2.28 eV above the VBM. Our calculations show that all charge states of V_{Ti} are shown in the band gap. Multiple pictures of V_{Ti} are seen in the theoretical literature on anatase. Phattalung et al.¹³⁵ found using LDA (Local Density Approximation) that V_{Ti} is a quadruple *shallow* acceptor, however, LDA is known to be inadequate in describing the band gap and correct localization of holes and electrons. Applying a Hubbard-like “U” value (which incorporates an occupation penalty scheme), Morgan et al. show that V_{Ti} is a *deep* acceptor (2-/0 transition occurs ~0.85 eV above the VBM). In this study, however, it is shown that there is no 0/1- transition level and the formation energy is ~2.5 eV lower than that calculated from our calculations.^{118,121} The only HSE06 calculations on V_{Ti} in anatase show that the defect transitions from the neutral charge state to the 2- then the 4- charge state over the band gap. In these calculations, only a Monkhorst-Pack 1x1x1 k-point sampling was used which can lead to inaccurate total energies and therefore uncertainty in the thermodynamic picture of the defects.⁹⁰

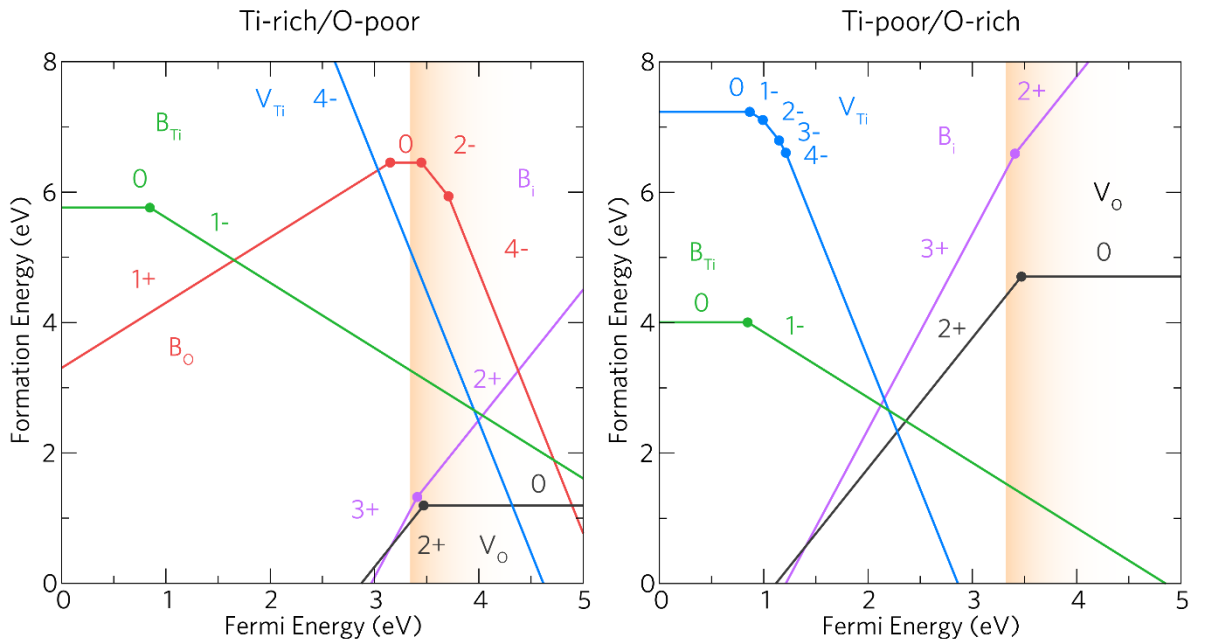


Figure 2.16. The transition level diagrams for B-TiO₂ under both Ti-rich/O-poor (left) and Ti-poor/O-rich (right) growth regimes. The Fermi energy goes from the VBM (0 eV) to 1.7 eV above the CBM (which is at 3.35 eV). The conduction band region is shown by the graded.

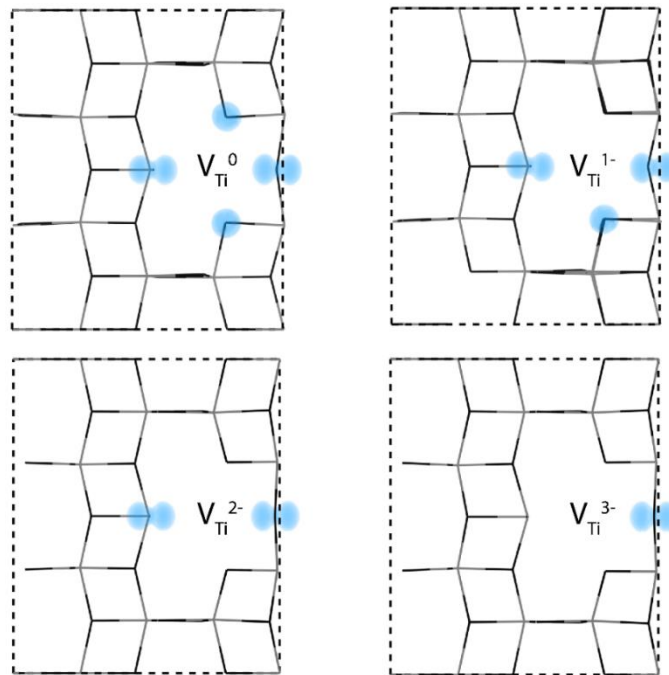


Figure 2.17. The partial charge densities of the charge states of V_{Ti} as viewed along the {010} direction showing the localisation of holes (blue isosurfaces) in each example. The isosurfaces are plotted from 0 - 0.015 eV Å⁻³.

2.4.5.3 B-Doping:

Reported and studied, theoretically and experimentally, by the research community, boron can enter the anatase lattice interstitially (B_i) or substitutionally on a titanium site (B_{Ti}) or oxygen site (B_o).

Previous theoretical studies have been carried out on B-TiO₂^{25,40,42,43,137,138} in particular, a study by Pacchioni and coworkers which gives a fairly comprehensive view on the electronic structure of various B related defects.

Under *Ti-rich/O-poor* conditions, B_i^{3+} is lowest in energy across the whole band gap, meaning that interstitial boron is the most preferential dopant state to form. B_i acts as a shallow dopant donating 3 electrons into the conduction band and has a very low formation energy. The Fermi level is pinned in the conduction band at ~ 0.65 eV above the CBM when the V_{Ti}^{4-} charge state falls low enough in formation energy to begin compensation of the donated electrons. Under *Ti-poor/O-rich* conditions, the formation energy of B_i is raised in energy and the Fermi level is pinned in the band gap ~ 2 eV above the VBM when B_{Ti}^{1-} and V_{Ti}^{4-} cross those of B_i^{3+} and V_o^{2+} .

The partial charge localization is shown for B_i in the 0, 1+ and 2+ charge states in **Figure 2.18a, b and c**.

B_i is a three electron donor, however when it reaches the 0 and 1+ charge states (~ 2.42 eV above the CBM) (**Figures 2.18a and b**), the donated electrons start to become highly localized on the B and adjacent Ti atoms, this has also been seen previously by Yang et al.⁴² the 2+ charge state is shows a delocalized electron (**Figure 2.18c**).

B_{Ti} has a high formation energy under *Ti-rich/O-poor* (B_{Ti}^0 occurs ~ 5.76 eV) where self-compensation is observed when B_{Ti}^{1-} crosses the B_i^{3+} line at ~ 2.12 eV above the VBM. Under *Ti-poor/O-rich* conditions, p-type defect favourable conditions, B_{Ti} is still relatively high in energy (~ 4 eV). The 1-/0 transition level occurs at ~ 0.85 eV above the VBM making this defect a *very deep* acceptor so no p-type capability should be seen. Under *Ti-rich/O-poor* conditions, B_{Ti} begins to self-compensate ~ 2.12 eV above the VBM. Previous theoretical studies have stated that B_{Ti} is the least favourable substitutional defect,^{43,137} however, we find the opposite is true. B_{Ti}^0 distorts from the Ti site by up to $\sim 11\%$ in the b direction forming a trigonal planar BO₃. The hole is localized on an adjacent O as shown

in **Figure 2.18d**, with the distortion clearly visible. In the 1- charge state, the B moves back towards the original Ti site now that the hole is removed reforming a tetrahedral BO₄.

The last defect to be considered is B_o which acts as a slightly deep donor with the 1+/0 transition level occurring at ~0.20 eV below the CBM. Under *Ti-rich/O-poor* conditions B_o forms at a high energy (~6.45 eV) and under *Ti-poor/O-rich* conditions this rises to ~15.23 eV. Beyond the CBM B_o quickly becomes an acceptor changing to the 2- charge state ~0.1 eV above the CBM then to the 4- charge state ~0.36 eV above the CBM. Under *Ti-rich/O-poor* conditions B_o becomes the dominant boron defect ~1.37 eV above the CBM. The partial charge density of the neutral and 4- charge states are shown in **Figures 2.18e and f** where localization is seen shared between the boron atom and the titanium atom below it. Accounts by Finazzi and coworkers²⁵ see an almost identical picture, however with more localization on the Ti, which could be an artifact from using a Γ -point only calculation. Less distortion is seen here than for B_{Ti} although in the neutral charge state B distorts ~5% in the c direction whilst the Ti below shifts ~4% from its original position away from the defect. The 4- charge state displays a quadruple polaron (**Figure 2.18f**) and the atoms shift back towards their original positions (~2% from B_{Ti}⁰).

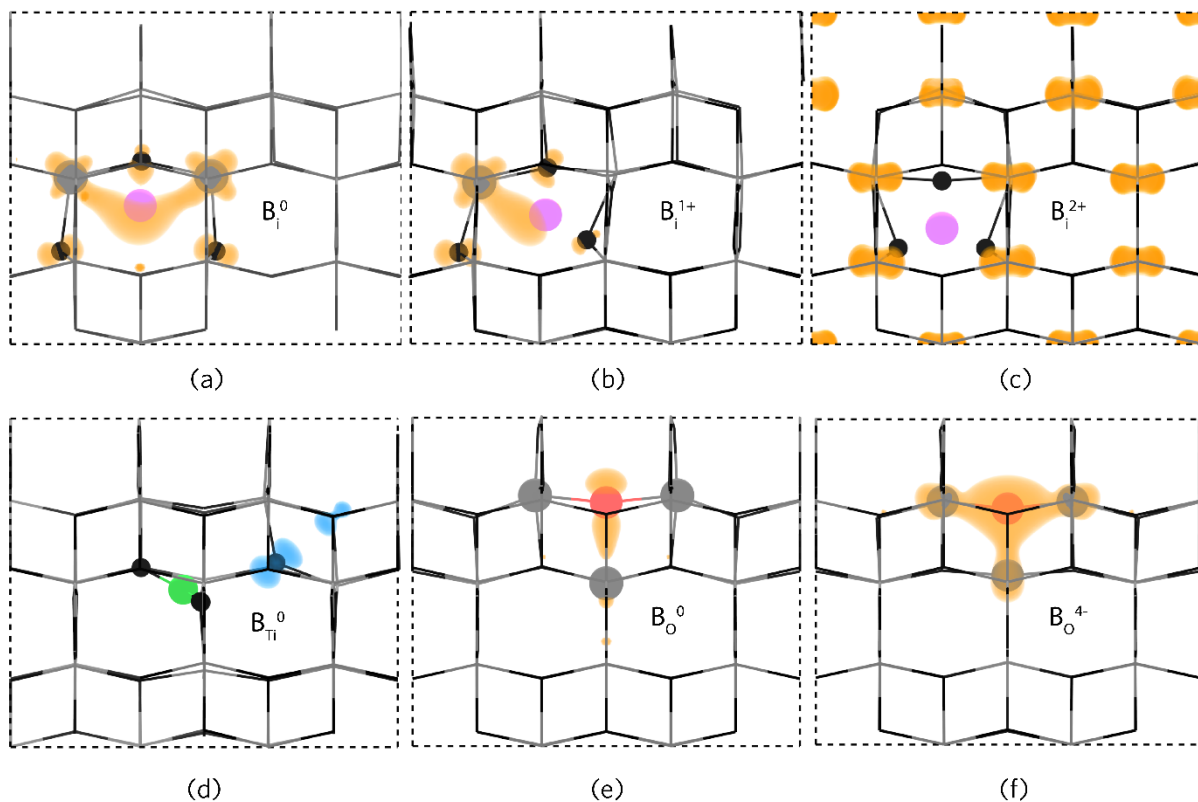


Figure 2.18. The partial charge densities of B_i^0 (a), B_i^{1+} (b), B_i^{2+} (c), B_{Ti}^0 (d), B_o^0 (e) and B_o^{4-} (f) defect charge states as viewed along the $\{100\}$ direction displaying the localisation of holes and electrons (blue and orange isosurfaces respectively). The isosurfaces are plotted from 0-0.015 eV \AA^{-3} .

2.5 Conclusions:

In this chapter, interstitial boron-doped anatase TiO₂ thin films of different concentrations were synthesised and deposited on glass by one-step APCVD. The content of boron (from 1-5% at.), was varied by increasing the mass flow rate of the precursor, boron isopropoxide, and varying the temperature of the bubbler where it was placed. XRD and Raman studies showed that anatase was obtained in the undoped and all of the boron-doped TiO₂ samples. In the case of sample C, when a higher mass flow of boron was used during the APCVD deposition, some rutile TiO₂ (\approx 15%) was formed along with a powdery deposition on top of some areas of the film. The powdery deposition was easily removed and was characterised by PXRD as a mixture of anatase and a form of boric acid (H₃BO₃), called sassolite. Demonstrated by XPS and D-SIMS analyses, boron was incorporated in TiO₂ as interstitial, being the most stable form of boron-doped TiO₂.^{45,63} No reduced form of Ti³⁺ was found on the surface of samples A and B. In the case of sample C, a small component attributed as Ti³⁺ was found on the surface, indicating that when the concentration of boron within the film is reaching its saturation levels, Ti⁴⁺ reduces to Ti³⁺ to compensate the charges, due to the incorporation of interstitial boron in its 3+ oxidation state. The incorporation of interstitial boron induced a noticeable change in the morphology of the doped-films, seen by SEM imaging and in the average particle size, more remarkable in the case of sample B-TiO₂ (A), where a low flow of boron isopropoxide was used. The optical band gap, obtained by UV-Vis spectroscopy, applying the Tauc plot method, slightly changed but no visible light absorption/response was found. The photocatalytic performance of B-TiO₂ films under UV, during the degradation of stearic acid, was enhanced, being much higher and noticeable in the case of sample A, which contains around 1% at. B. Surprisingly, and reported for the first time, interstitial boron-doped TiO₂ samples presented certain conductivity and electron mobility, proven by multimeter and Hall Effect measurements.

From the theoretical and computational analyses, we show that in the likely event of B_i forming, the material will be made n-type under *Ti-rich/O-poor* conditions, explaining the n-type conductivity measured. B_i³⁺ is the most preferential dopant state to form. Under *Ti-poor/O-rich* conditions the Fermi level will be trapped \sim 2

eV above the VBM, indicating that electrons trapped at this level could be excited by visible light into the CBM thus increasing the visible light activity.

Chapter 3

Interstitial B-TiO₂ thin films synthesised by AP-PECVD: Dual injection approach

3.1 Introduction

In this **chapter 3**, an atmospheric-pressure plasma-enhanced chemical vapour deposition (AP-PECVD) approach is investigated in the perspective to lower the formation temperature of anatase boron-doped titanium dioxide thin films. The coating of a thermo-sensitive polymeric substrate, poly-methyl methacrylate (PMMA) optical fibres, and silicon and glass substrates with boron-doped TiO₂ anatase thin films is reported. The B-TiO₂ thin films, which presented enhanced photocatalytic properties when compared to undoped samples, were formed from the one-step CVD reaction of titanium and boron precursors by an atmospheric plasma generated in a microwave cavity. As mentioned previously in chapters 1 and 2, TiO₂ thin films have attracted the attention of scientists for the past years and have been commonly produced using different synthetic methods, such as hydrothermal treatment,⁴ sol-gel,⁶⁰ surface impregnation, electrochemical deposition,¹³⁹ and physical⁴⁷ and chemical vapor deposition methods.⁵¹ CVD is a well-known, adjustable and flexible technique employed to synthesize a vast

number of metal and non-metal chemical species in the form of thin films and coatings.^{6,51,140} CVD techniques commonly involved the use of a heating source to produce a solid deposit or a thin film. For instance, the average temperature required in the synthesis of anatase TiO₂ by atmospheric pressure chemical vapour deposition (APCVD) can be placed between 400-600 °C.⁵ The limitation that reaching such high temperatures presents for certain applications, has led the scientific community to different modifications and approaches, *i.e.* the use of plasma sources often allows much lower deposition temperatures. In the last years, plasma-enhanced chemical vapour deposition (PECVD) processes are extensively used for surface modification and thin film deposition.¹⁴¹ Both, low-pressure and AP-PECVD^{141,142} have allowed the deposition of TiO₂ thin films at lower substrate temperature than conventional CVD.^{141,143} Recently, S. Dong *et al.* have used an atmospheric RF plasma source to synthesise TiN_x/TiO₂ hybrid coatings.¹⁴⁴

Anatase TiO₂ has been widely used for several photocatalytic applications,¹⁹ including water and air purification, antibacterial coatings,¹⁴⁵ self cleaning materials,¹⁴ photoelectrochemical cells for solar energy-harvesting devices,¹⁴⁶ electricity production, and water splitting.¹⁰ Nevertheless, anatase TiO₂ presents a relatively wide band gap (~ 3.2 eV), which lies in the UV region of the electromagnetic spectrum, minimising its outdoor applications at ground level (< 5% of solar photons can excite the photocatalyst). This has led to a vast number of studies to modify and improve its intrinsic properties, and overcome the existing drawbacks. TiO₂ has been combined with noble metal nanoparticles (Ag, Pt, etc.)⁷ resulting in a significant enhancement of its photocatalytic properties. However, the most commonly studied approach has been the chemical modification of TiO₂ using metal or non-metal species (S, C, N, B). The addition of dopant species to the lattice of TiO₂ results in a modification of its electronic structure, facilitating the use of lower energy photons to excite the material's band gap, and thus extending its photocatalytic response into the visible range.²¹

The chemical modification of TiO₂, especially through the implementation of nitrogen species, has been widely explored. Unfortunately, despite the wealth of literature on N-doped TiO₂ materials, there is little consensus on whether this leads to an overall improvement in visible driven photocatalysis.^{39,147} Therefore, alternative non-metal species have been extensively explored in the last few

decades. The use of boron as a dopant has attracted attention because of its creation of electron acceptor levels.⁴⁴ When boron is incorporated into the TiO₂ lattice it can appear and/or coexist in two different oxidation states; whether as interstitial B (B_{int}), within the TiO₂ lattice, or as substitutional (B_{sub}) replacing oxygen.²⁵ Interestingly, when boron occupies an interstitial position within the TiO₂ lattice, the stability of the boron-doped TiO₂ is far superior than when compared to that of substitutional boron. In terms of formation energy per unit cell, B_{int} is the highly preferred B-doping site in TiO₂, while B_{sub} is difficult to obtain experimentally because of the high formation energy.⁴⁴ The substitutional boron-doped TiO₂, which seems to be metastable, decomposes into boron oxide.^{45,63} Previously, the synthesis of boron-doped TiO₂ has been focused on the formation of powders by sol-gel, annealing and hydrothermal methods.⁶³ B-TiO₂ thin films deposited by APCVD were reported for the first time by Carmichael *et al.*⁴⁸ where O-substitutional boron-doped TiO₂ led to noticeable rates of hydrogen production and more favourable photocurrent profiles when compared to that of undoped TiO₂ coatings. Very recently, thin films of interstitial boron-doped TiO₂ with an enhancement of photoactivity and a significant change in the morphology of the films is described in Chapter 2. The interstitial B-TiO₂ thin films, synthesized by APCVD and deposited on glass at 500 °C, exhibit enhanced photoactivity under UV light and higher stability.⁶⁴

To summarise the following chapter and briefly introducing the data presented here, poly(methyl methacrylate) (PMMA) optical fibres were coated with crystalline photocatalytic anatase and doped-TiO₂ thin films in a one-step AP-PECVD process. Among the numerous routes towards the deposition of anatase TiO₂ thin films, the AP-PECVD method developed is particularly suitable for the treatment of polymer optical fibres and the preparation of optical fibres for the photocatalytic decontamination of water or air. This was the first time that doping of TiO₂ by AP-PECVD was done and reported. Titanium ethoxide (TEOT) and boron isopropoxide were the selected precursors for the formation of anatase titanium dioxide and the source of the dopant, respectively. The selection of the TiO₂ precursor, *i.e.* TEOT, ensured the deposition of dense and crystalline TiO₂ thin films in contrast to the more conventional TiO₂ CVD precursors, *i.e.* TTIP and TiCl₄. As a matter of fact, recently reported by Kamal B. *et al.*, when employing TTIP with a similar setup such as the one described in the present chapter,

powdery and poorly crystalline coatings with low adherence and low photocatalytic degradation rates were obtained.¹⁴⁸

Previous PECVD reported results have shown the formation of dense and smooth coatings when using TEOT and rough coatings composed of nanoparticles when using TTIP.¹⁴⁹

Thin film growth of TiO₂, is influenced by the length of the precursor's alkoxy groups which are responsible for the resulting chemistry, crystallinity and morphology of the films.¹⁴⁹ For instance, TEOT, which has shorter alkoxy groups when compared to TTIP, is expected to be more reactive in terms of forming higher concentration of reactive species in the gas phase. Once created, the reactive species increase the amount of absorbed species at the substrate surface, forming many nucleation sites that enhance the growth of denser and more crystalline coatings with smoother surfaces. On the other hand, the use of TTIP results in a lower amount of reactive species upon exposure to the plasma due to longer alkoxy groups and a slower dissociation rate. Hence, the reactive species form at early stage of the reaction coexist with unreacted precursor molecules, affecting negatively the development of crystallinity of the films.

These observations are consistent with the work of Ritala et al.,¹⁵⁰ where an evident inverse relationship between the growth rates of TiO₂ films and the size of precursor molecules was reported. The films grown from the alkoxides were more crystalline than those deposited from TiCl₄.¹⁵⁰

3.2 Experimental Section

3.2.1 Atmospheric Pressure Plasma Enhanced CVD (AP-PECVD) setup

As described and presented in **Figure 3.1**, the AP-PECVD reactor was mainly composed of a power generator, a gas line, a wave launcher, a discharge tube, a deposition chamber, an ultrasonic generator, a syringe pump connected to a nozzle and a bubbler, where the dopant precursor was placed. The plasma, a surface wave discharge (cold plasma) was generated at atmospheric pressure inside a quartz tube (discharge tube) of 5 and 7 mm inner and outer diameter, respectively. Plasma was generated by applying a high-frequency electric field to a gas (Argon by Air Liquide, 99.999%) flowing in the discharge tube by means of a wave launcher. The MW generator (power generator) with a frequency of 2.45 GHz was operated in continuous mode with a power of 200 W. The wave launcher (Surfatron 80 by SAIREM) was powered *via* a coaxial cable and cooled by water. The discharge tube was cooled down by compressed air and its end was at a distance of 3 cm from the launching gap (**Figure 3.1**). The flow of discharge gas, *i.e.* argon, was maintained at 10 standard litres per minute (slm) by a MKS mass flow controller.

Titanium ethoxide ([Ti(OC₂H₅)₄], 80%) was diluted in toluene ($\geq 98\%$) to 0.5 M. In order to facilitate the injection of the precursor for the thin film deposition, the precursor flow rate was fixed at 10 $\mu\text{L}\cdot\text{min}^{-1}$ and carried toward an ultrasonic nebulizing nozzle operating at 120 kHz (Sono-Tek). The mist formed at the outlet of the nozzle was composed of droplets with diameters ranging between 10 μm and 20 μm and which were carried by a mixture of gases, argon/oxygen (see **Table 3.1**). The boron precursor, boron isopropoxide (B(OCH(CH₃)₂)₃), $\geq 98\%$ was placed in a separated bubbler, connected to the nebulizing nozzle, joining simultaneously the flow of Ar (carrier gas). The solution was bubbled by using a constant flow of 0.1/ 0.5 and/or 0.9 $\text{L}\cdot\text{min}^{-1}$ of Ar, making the total flow of Ar carrier gas equal to 1 $\text{L}\cdot\text{min}^{-1}$ (*i.e.* 0.9 + 0.1 $\text{L}\cdot\text{min}^{-1}$). The post-discharge distance from the launching gap was equal to 6 cm after the initiation of the plasma discharge.

Typical deposition was carried out for 10 minutes, keeping constant all the parameters previously described.

Films were grown on both, side glowing PMMA (2 mm of diameter; Luxylum) and silica core with polyimide cladding (0.8 mm diameter; CeramOptec) optical fibres (OFs) as well as on double side-polished silicon wafers and glass microscope slides (2 × 2 cm) for technical reasons in terms of film characterisation. For the OFs substrates, pieces of 1 m length were placed from the left to the right side of the experimental setup and through the discharge tube in a horizontal position. In the present chapter, all the deposition on OFs were performed in the static mode for a total duration of 3 min. The characterized area of the coated-OFs was located in the post-discharge region (from 5 to 8 cm from the launching gap) and close to the precursor injection outlet (*i.e.* 6 cm from the launching gap). Silicon wafer and glass substrates were cleaned and prepared for deposition using absolute ethanol (97 %) and dried with nitrogen prior to use. In the case of the silicon substrates, during the depositions, the substrate was placed in the deposition chamber in the same horizontal position as OF substrates (**Figure 3.1**), at a distance of 6 cm from launching gap. The deposition time for the experiments carried out on Si wafers was 10 min. The precursors, titanium ethoxide (0.5 M in toluene) and boron isopropoxide (placed in a bubbler) were injected and led in the post-discharge zone to avoid an excessive gas phase reaction, which would conduct to a powdery deposition (**Figure 3.2a and b**).

Table 3.1. Experimental parameters of the AP-PECVD depositions. (*) When necessary, P1 is shown in different substrates, appearing as P1(OF), P1(Si) and P1(G) for optical fibre, Si wafers, and glass, respectively.

Sample	Substrate	Carrier gases		Plasma parameters			Precursors		
		Ar flow	O ₂ flow	Surfatron-injection	Plasma power	Ar	Ti injected	B flow	Deposition
		[slm]	[slm]	distance [cm]	[W]	[slm]	[uL/min]	[slm]	[min]
P1(*)	Si/glass/OF	1	1	6	200	10	10	N/A	10
P2	Si/glass	0.1	1	6	200	10	10	0.9	10
P3	Si/glass	0.5	1	6	200	10	10	0.5	10
P4	Si/glass	0.9	1	6	200	10	10	0.1	10
P5	OFs	0.5	1	6	200	10	3	0.5	10

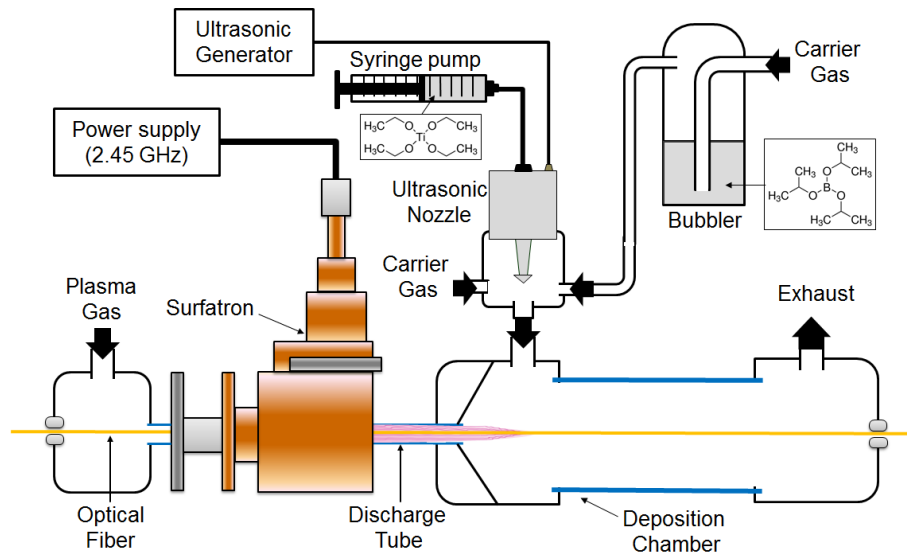


Figure 3.1. Schematic of the AP-PECVD apparatus set up for doping.

3.2.2 Analytical techniques

The Raman spectra were recorded with a Renishaw inVia micro-Raman spectrometer at an excitation wavelength of 532 nm with a laser power of approximately 0.44 mW focused on a 1 μm^2 spot. X-ray diffraction (XRD) patterns of the films were obtained using a Lynxeye XE Bruker-Axs D8 diffractometer. The instrument operates with a Cu X-ray source, monochromated ($K\alpha_1$, 1.54 Å).

Scanning electron microscopy (SEM), employed to characterize the thickness and morphology of the coatings, was performed on a Hitachi SU-70 FE-SEM. Prior to SEM observations, the nonconductive sample was sputter-coated with 5 nm of platinum to prevent image charging and distortion. XPS analyses were performed on a Kratos AxisUltra DLD instrument using a monochromatic Al $K\alpha$ X-ray source ($h\nu = 1486.6$ eV) at pass energy of 20 eV. AES was performed on a ThermoVG Microlab 350 operating at 20 kV, 3 nA, and 30°. Argon sputtering operating at 2 keV and 2 mA was used for approximately 500 s in a roasting mode in order to remove surface contamination and gain information on the elemental composition in the bulk of the coating. The peak positions of the samples were referenced with respect to carbon (C 1s) at 285.4 eV.

Secondary Ion Mass Spectrometry (D-SIMS) were obtained in a Cameca SC-Ultra instrument in positive ion mode, by a bombardment with Cs^+ ions, having an impact energy of 1.0 keV.

3.2.3 Photocatalytic test

The photocatalytic activity of undoped and boron-doped TiO_2 films under UV light was evaluated by measuring the photodecomposition of methylene blue (MB) in aqueous solution ($\text{C}_{16}\text{H}_{18}\text{N}_3\text{S}-\text{Cl}-3\text{H}_2\text{O}$; 0.05 wt.% in H_2O , Sigma-Aldrich) with an initial concentration of 10 $\mu\text{mol}\cdot\text{L}^{-1}$ and a volume of 2 mL. The samples with a size of 1 cm^2 were immersed in the dye solution in a 12 well plate (each sample in a different well). The well plate containing the samples and the dye was stirred using an orbital shaker (250 rpm) under irradiation of a 16 W black light lamps (Herolab; 365 nm, 2 $\text{mW}\cdot\text{cm}^{-2}$). Before light irradiation, the solutions were stirred in dark for 2 h to ensure the establishment of an adsorption–desorption equilibrium. Photocatalytic degradation was monitored by measuring the

absorption spectra of the MB solution at 664 nm with a UV-Vis spectrophotometer (Tecan Infinite M1000 Pro).

3.3 Results and discussion:

3.3.1 Synthesis of the samples: structure & morphology

Results and discussion are based on the selected most representative samples out of several depositions, after parameters were optimised. AP-PECVD synthesis of all samples, undoped and boron-doped TiO₂, was carried out by using [Ti(OEt)₄] and B(OiPr)₃ as precursors. As explained in section 3.2.1, the precursor for boron was placed in a separated bubbler, whereas the precursor for Ti was injected directly into the mist. Sample P5 was synthesized using the same experimental parameters as for P3, but the selected substrate was PMMA optical fibre. These parameters were selected based on the analysis of the data in terms of functional properties. Sample P3 presented the optimised deposition parameters, making its synthesis on polymeric optical fibre (POF) more interesting. The thin films were characterized by Raman spectroscopy, XRD, UV-Vis spectroscopy, SEM, XPS, D-SIMS and their photocatalytic activity under UV light was measured using methylene blue aqueous solution and following the degradation of stearic acid by FTIR.

It is important mentioning that this special configuration of the plasma-assisted APCVD reactor allows the deposition of crystalline oxides thin films on temperature-sensitive substrates that, otherwise would see their physical properties compromised by the heating source traditionally required (hot plasmas). Indeed, atmospheric-pressure microwave plasma discharges are surface discharges that induce a high degree of ionization and high electron density on the inner surface of the quartz tube (**Figure 3.1**). On the other hand, the central part of the tube is far less reactive and the temperature suitable with the use of polymer substrates. The specific conditions used for the deposition of photocatalytic B-TiO₂ (**Table 3.1**) thin films ensured the conformal coating of side-glowing PMMA optical fibres, which can be illuminated and activate the crystalline

oxide coating on their surface with light passing through their cores. After the deposition, it was observed that the optical fibres kept their elasticity and flexibility. More importantly, their ability to diffuse light was also retained (**Figure 3.2c**), as when the light passed through no visual variation was observed compare to non-coated OF. This property is an essential feature for their use, *i. e.*, in a photocatalytic optical fibre reactor (OFR). Supplementary, after the macroscopic observations, scanning electron microscopy (SEM) analysis (**Figure 3.10a and b**) confirmed that both, the undoped and boron-doped TiO₂ thin films, were well adhered to the polymer optical fibres (POFs).

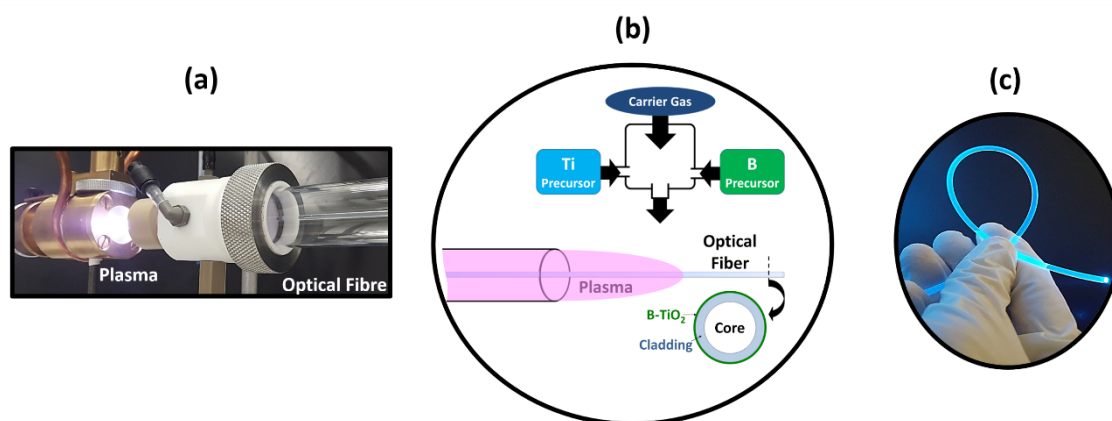


Figure 3.2. AP-PECVD deposition on optical fibre: (a) photo of the microwave plasma reactor and PMMA optical fibre being coated, passing through the plasma; (b) simplified scheme of the plasma coating process; (c) photo of the illuminated PMMA optical fibre coated with B-TiO₂ (sample P5).

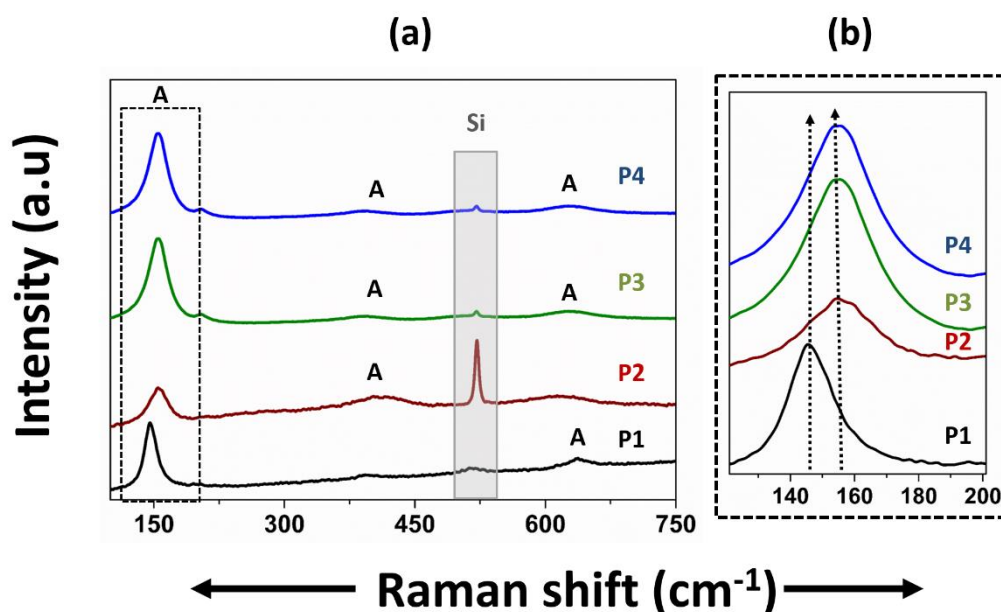


Figure 3.3. Raman analysis of the samples deposited on Si wafers: (a) compilation of Raman spectra of boron-doped samples (P2, P3, and P4) compared to the undoped reference (P1), synthesised by one-step AP-PECVD; (b) Zoomed Raman shifting (E_g band) of the spectra.

To investigate the structure and crystallinity of all samples, undoped TiO₂ and boron-doped TiO₂ thin films deposited by AP-PECVD, Raman spectroscopy, and X-Ray diffraction (XRD) analyses were performed (**Figure 3.3 and 3.4**). These studies confirmed the presence of solely anatase TiO₂ phase in both, undoped and boron-doped TiO₂ thin films. The major scattering E_g band, typically found at 144 cm⁻¹ in undoped TiO₂ anatase materials,^{1,23} can be clearly observed at 145.8 cm⁻¹ for sample P1 (**Figure 3.2b**).

This scattering E_g band was shifted to higher wavenumbers when TiO₂ was boron-doped, in the case of samples P2, P3 and P4 (**Figure 3.2b**), to 155 cm⁻¹, for B-TiO₂ films.

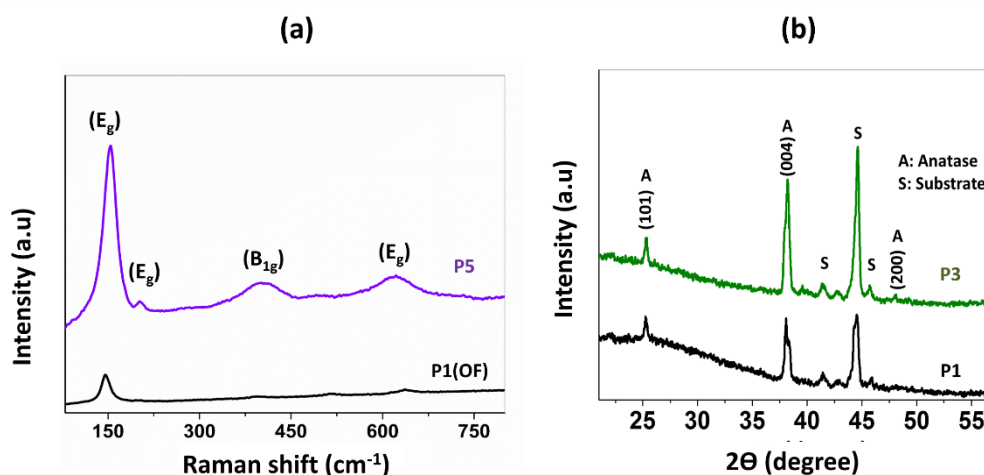


Figure 3.4. (a) Raman spectra of the undoped and boron-doped samples deposited on optical fibres (P5); (b) XRD patterns of samples P1(undoped) and P3 (B-TiO₂) deposited on Si wafers.

The shifting did not show changes between all the doped samples, *i. e.*, as the flow of boron isopropoxide, increased during the AP-PECVD deposition, the shifting of the E_g band does not show any changes between all doped samples, whereas there is a clear shifting when comparing undoped TiO₂ film (P1) to any of the boron-doped samples (P2, P3 or P4).

The described shifting has been observed previously when doping TiO₂ with boron,³⁰ due to the incorporation of boron in the TiO₂ lattice, inducing a change in the mode of vibration of pure TiO₂. No signal due to boron or boron oxide (B₂O₃) was detected by Raman spectroscopy. Differences in the intensity can be observed as well. The intensity of the Raman spectra depends on the i) intensity of the light source ii) the wavelength, indirectly proportional (1/λ⁴) iii) the number of molecules/ concentration of the sample and iv) the scattering properties of the sample. The intensity of the peaks for the B-TiO₂ was higher than in the case of the undoped sample (pure anatase). As the two first factors mentioned previously are similar, and the morphology of the films seen by SEM are similar, so the scattering properties of the sample might be similar, the distribution and/or the concentration of the molecules (crystals) in B-TiO₂ and undoped TiO₂ are likely to be slightly different.

In **Figure 3.2b**, XRD analysis of samples P1 and P3 showed anatase TiO₂ in both cases, undoped and doped B-TiO₂. Preferred orientation for the growth of the films was observed. For undoped and boron-doped samples (P1 and P3), peaks matching planes (004) and (101) were seen as the preferred. There was not any noticeable shifting of the main peak for anatase, corresponding to the (101) plane. In both cases, for TiO₂ and B-TiO₂ the peak appeared around $\sim 25.3^\circ$ (2 theta). Boron-doped and undoped TiO₂ thin films deposited on silicon wafers were used for the XRD analysis, for technical reasons.

Once the presence of anatase was proven, to prove and demonstrate the presence of boron, X-ray photo-electron spectroscopy (XPS) and dynamic secondary ion mass spectrometry (D-SIMS) were used to study the nature and concentration of boron within the TiO₂ coatings. As XPS is a surface-sensitive technique (≤ 10 nm),¹⁵¹ several depths within the bulk were investigated by etching the surface with argon sputtering.

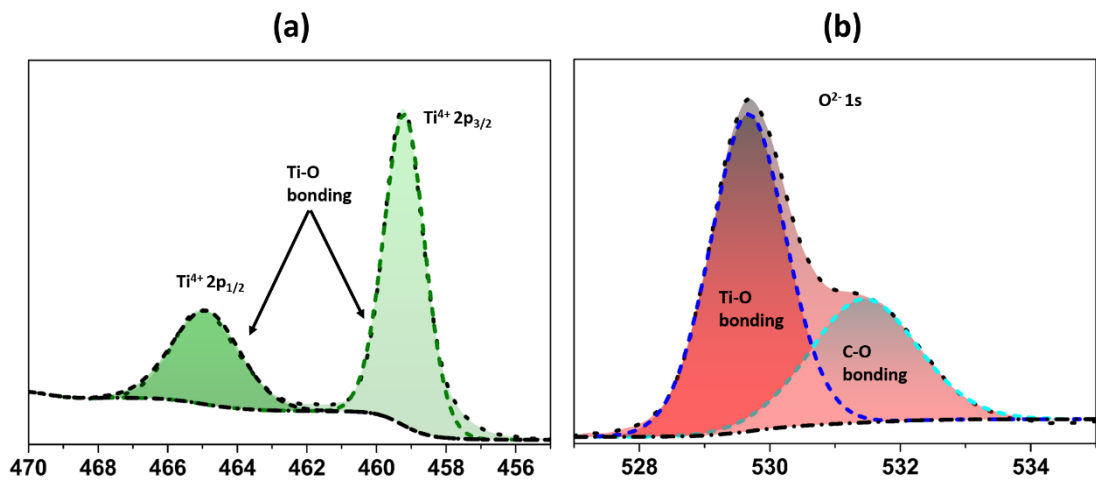


Figure 3.5. Typical XPS fitted spectra for TiO₂ on the surface of sample P1: (a) Ti 2p and (b) O 1s chemical environments.

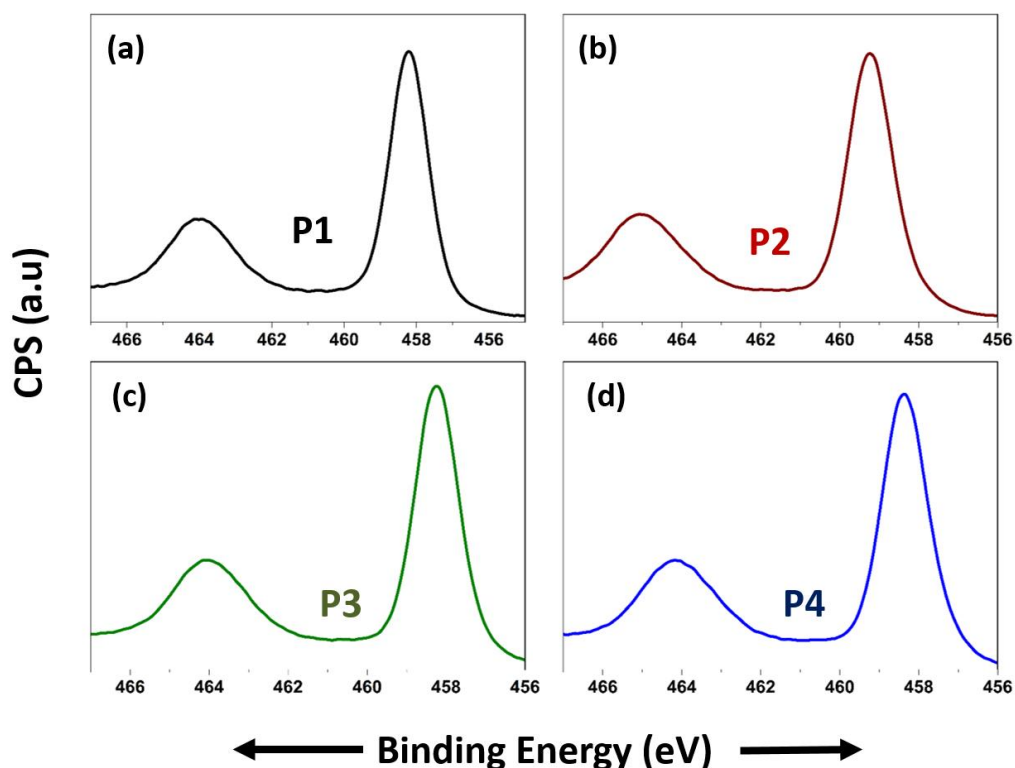


Figure 3.6. Surface XPS spectra in the Ti 2p environment of all samples deposited on Si wafers: (a) undoped (P1) and (b, c, and d) B-TiO₂ samples P2, P3, and P4. This graph does not show fitting of the spectra.

XPS analysis showed the Ti 2p environment peaks at average binding energies ~ 458.9 and 464.6 eV, for Ti⁴⁺ 2p_{3/2} and Ti⁴⁺ 2p_{1/2} respectively. The peaks were attributed to Ti-O bonds of Ti⁴⁺ in TiO₂.¹⁰⁶ No presence of reduced Ti³⁺ species were detected on the surface upon instrumental error (**Figure 3.5**). The O 1s peak was observed at binding energy values of 530.4 eV, confirming the formation of TiO₂.⁵⁰ When targeting B1s chemical environment by XPS, all as-synthesised B-TiO₂ films showed a single peak (**Figure 3.7**) at 192.1, 191.4 and 191.3 eV, respectively for samples P2, P3, and P4. The corresponding peaks were assigned to interstitial boron. Generally, when B is found at a binding energy between 191-192 eV then it is attributed to interstitial boron.^{45,64,152} Following this classification, the boron incorporated into the TiO₂ deposited by AP-PECVD most likely occupies an interstitial position. The concentration of the different elements,

extracted from the XPS analysis showed that the percentage of Ti and oxygen remain similar in both cases, undoped and boron-doped TiO₂. Surprisingly, the total concentration of boron in all B-TiO₂ thin film was found to be $\approx 4\%$ at. (surface and bulk). A small shifting and change in the position of B1s peak of the doped samples was observed as the flow of the boron precursor was modified, the final concentration of boron (element) in all doped films was similar. The synthesis and XPS analyses were repeated several times and the concentration of B in the films did not present noticeable differences between samples P2, P3, and P4.

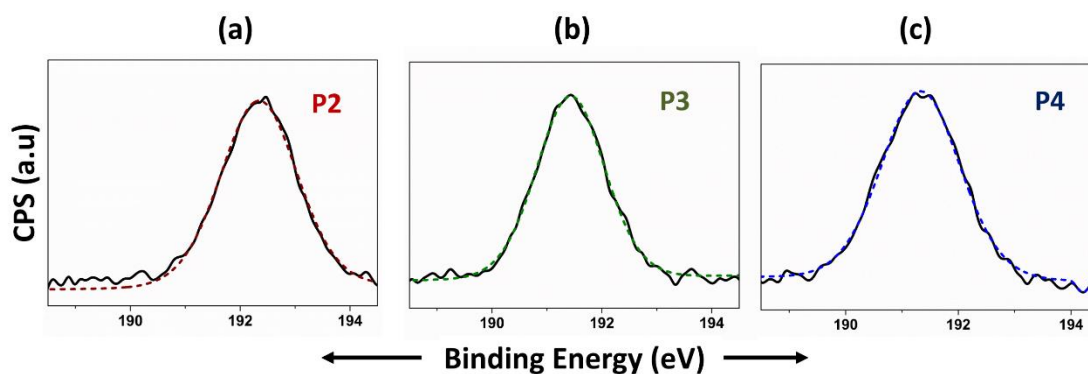


Figure 3.7. B1s environment XPS surface spectra of B-TiO₂ samples deposited on Si wafers. Black lines represent the experimental raw data (CPS); Dashed colourful lines represent the fitting.

To confirm what was observed by XPS analyses, in-depth D-SIMS analysis was carried out. Further elemental studies were carried out using D-SIMS depth profile analysis (see **Figure 3.8**), confirming the presence of boron within the bulk of the film.

The D-SIMS analysis must be interpreted as purely qualitative and as an extra analysis confirming the presence of boron, due to its high sensitivity compared to XPS analyses, since boron is the lightest element that can be detected by XPS. Some of the reasons why the SIMS analysis could not be performed as quantitative is the need of a verified standard reference sample and complex procedures, which due to complex matrix effects, could not be found by any commercial provider. However, the combination of SIMS analysis plus XPS spectra allowed further interpretation of the data.

As seen in **Figure 3.8**, The D-SIMS profile of all B-TiO₂ samples appeared to be quite similar. The differences in shape depended on the thickness of the spot of the sample which was sputtered. As it can be seen in **Figure 3.8d**, a comparison of the ratio Ti/B, based on the normalised counts per second obtained during the in-depth analysis, showed that the content and profile of boron in all B-TiO₂ samples was similar. As also confirmed by XPS data, the concentration of the dopant, *i.e.* B, was found to be very similar in all depositions.

Both analysis, XPS, and D-SIMS demonstrated that there is boron found as a dopant and that it was present on the surface and through the bulk of the boron-doped TiO₂ thin film. Hence, the deposition of anatase B-TiO₂, most likely to be interstitial B-TiO₂ from the XPS data, can be confirmed.

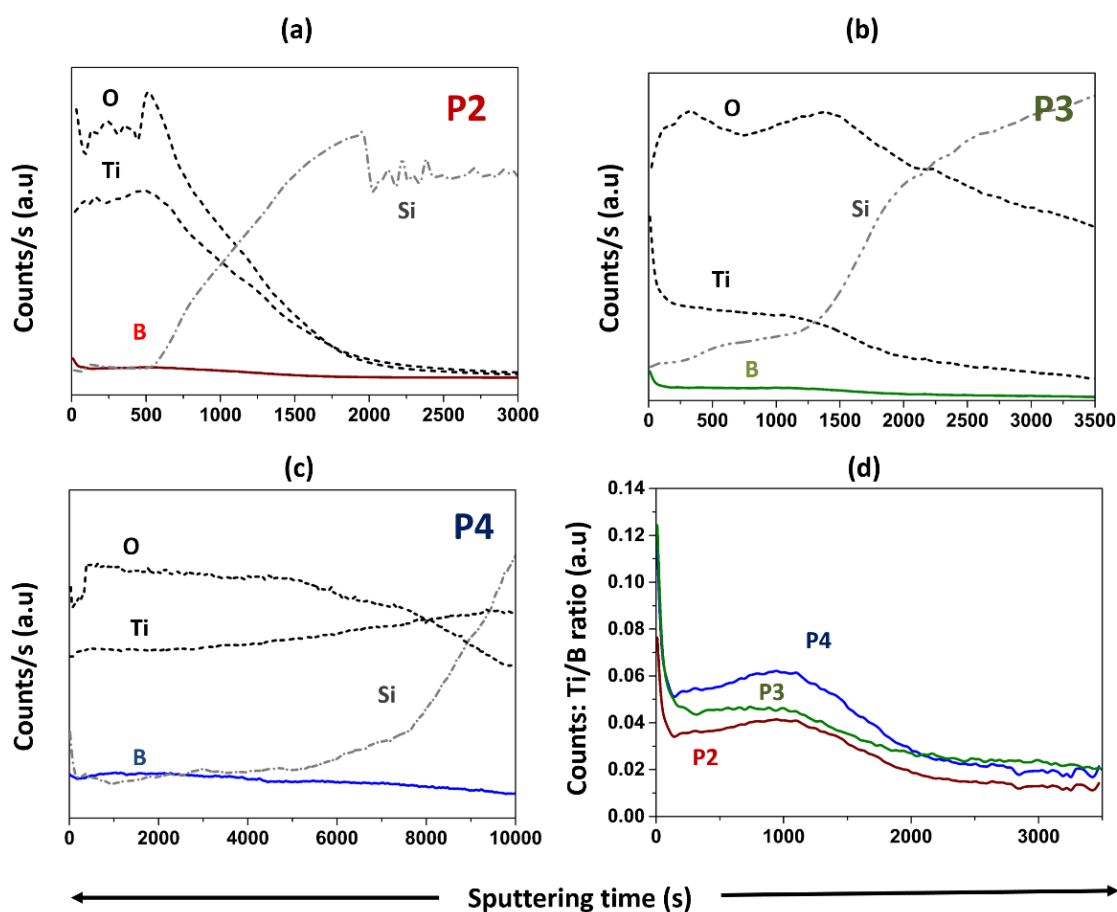


Figure 3.8. D-SIMS elemental analysis spectra of boron-doped TiO₂ films deposited on Si wafers, for the selected elements (O, Ti, B, and Si): (a) spectra for sample P2; (b) spectra of sample P3; (c) spectra of sample P4 and (d) comparison of the normalised ratio Ti/B for all samples, calculated from the counts of previous spectra. Black short-dashed lines represent O and Ti; gray dash-dotted lines represent Si; colourful lines (red, green and blue) represent B counts in each sample, P2, P3 and P4 respectively.

3.3.2 Morphology of the films

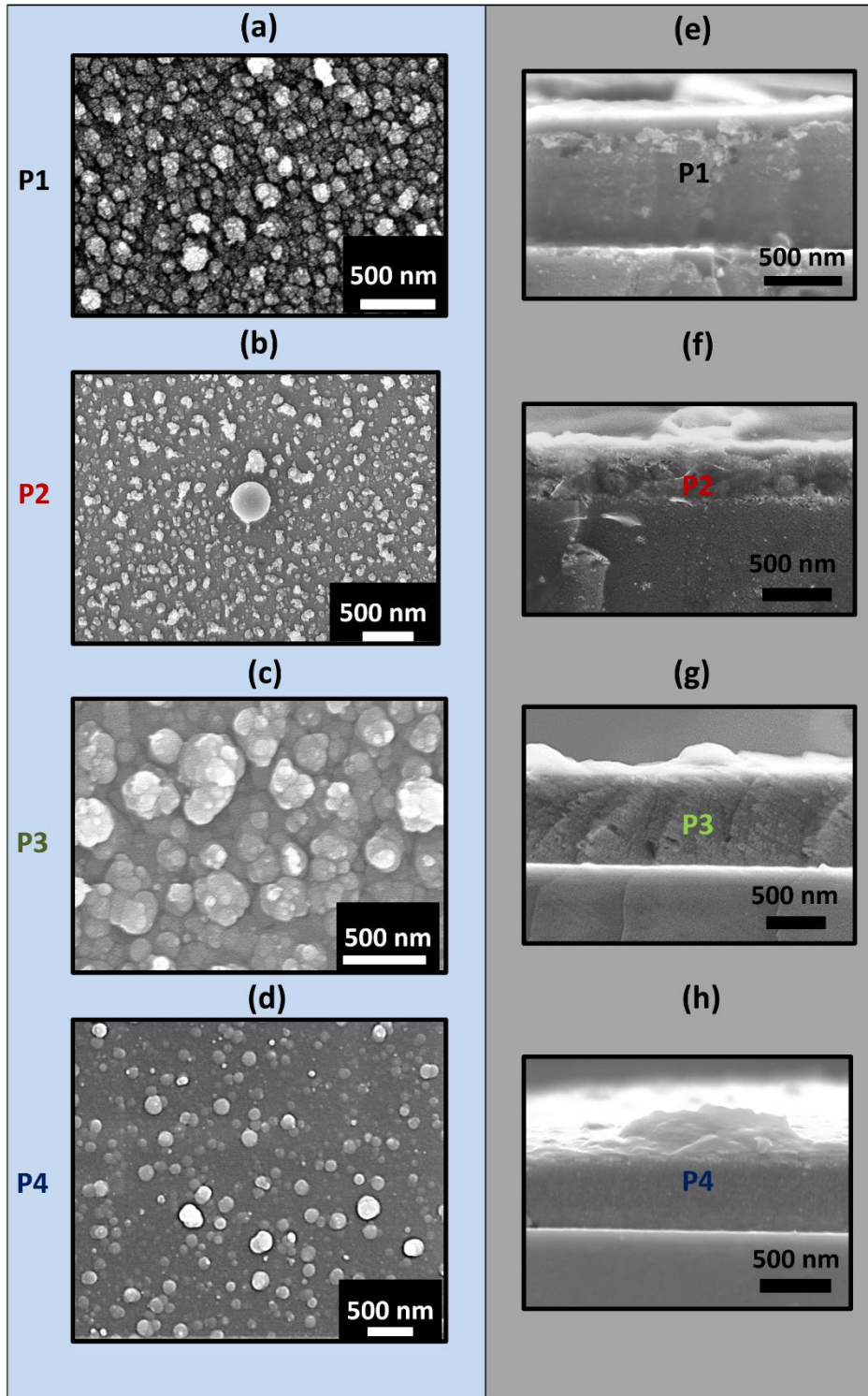


Figure 3.9. SEM analysis: Top view SEM images of all samples deposited on Si wafers, undoped (P1) and boron-doped (P2, P3, and P4) respectively (a, b, c and d); Cross-section SEM images of all samples (e, f, g, and h).

For sample P5, side view SEM analyses showed the effective deposition and coating of a B-TiO₂ thin film on optical fibre substrates (**Figure 3.10**). It can be clearly observed that the thin films were well attached to the substrate, with a growth rate estimated around 72 nm·min⁻¹. In addition, top-down SEM analysis showed B-TiO₂ thin films with spherical shape particles (~ 50 – 150 nm in diameter). As seen in **Figure 3.9**, there are some areas containing larger particles (~570 nm in diameter). These particles maybe formed from the gas phase reaction of the precursors with the reactive species of the plasma discharge, inducing a high concentration of condensable species which further leads to high concentrations of nucleated particles that grow by condensation and coagulation.²⁸ The number of formed particles in the gas phase and observed at the surface of the films is therefore related to the precursor concentration, but also to the density and energy of the plasma post-discharge. Furthermore, the PMMA optical fibre has a melting point of 160 °C.¹⁵³ The successful deposition on substrates of such chemical nature demonstrated that the deposition temperature was at least below 160 °C.

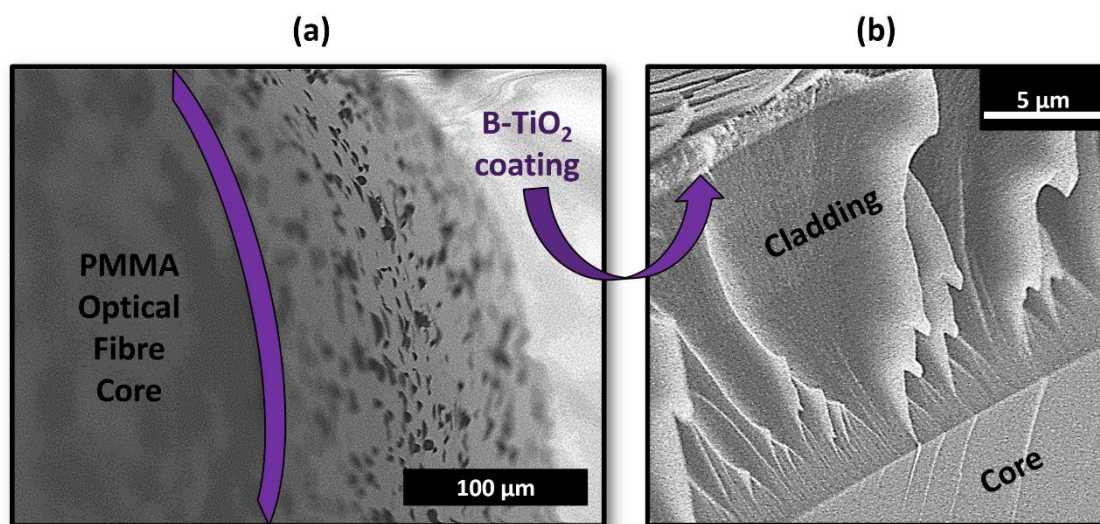


Figure 3.10. SEM analysis of B-TiO₂ thin film deposited by AP-PECVD on optical fibre. (sample P5): (a) Side view of the coated optical fibre with a tilted angle; (b) SEM cross-section image of P5.

3.3.3 Functionality of the samples:

In this section, both the optical and the photocatalytic properties, the functional properties of interest of the films, will be discussed. Calculated from the UV-Vis spectra (transmittance) of the samples, a representation of a Tauc plot can be observed in **Figure 3.11**.

By observing the results, the experimental band gap for the undoped TiO₂ sample (P1) was found ~ 3.44 eV, whereas for the boron-doped samples at ~ 3.40 eV for samples P2 and P4 at ~ 3.3 eV for sample P3. As reported in table 1 (section 3.2.1), all samples were synthesised under the same conditions, only the flow rate of the bubbler containing boron isopropoxide was varied. The experimental value for the optical band gap in the case of undoped TiO₂ (P1) and boron-doped samples P2 and P4 was very similar. Hence no changes were experienced in the optical band gap between samples P1 (undoped), P2 and P4. However, sample P3 showed a small shifting to a lower energy (~ 0.14 eV less). The shifting to a lower energy has been previously observed and reported in the literature as well as experimentally in chapter 2 when the TiO₂ was doped with boron and also when interstitial B-TiO₂ thin films were synthesised by APCVD.^{45,64,152}

From the theoretical calculations done on interstitial boron-doped TiO₂ thin films synthesised by APCVD and summarised in chapter 2, section 2.4.5, the interstitial B³⁺ is the most suitable dopant state for B-TiO₂ systems, and as purely interstitial, induces only small changes in the band gap. However, the photocatalytic performance of boron-doped TiO₂ improved when compared to undoped, under UV light, but only in the special case of a Ti-poor/O-rich environment. There, the Fermi level could be trapped around 2 eV above the VBM, so the electrons trapped at this level could be excited by visible light.

The boron-doped TiO₂ films synthesised by AP-PECVD, using a dual injection approach, slightly change their optical band gap and did not absorb in the visible range of the light spectra (**Figure 3.11**).

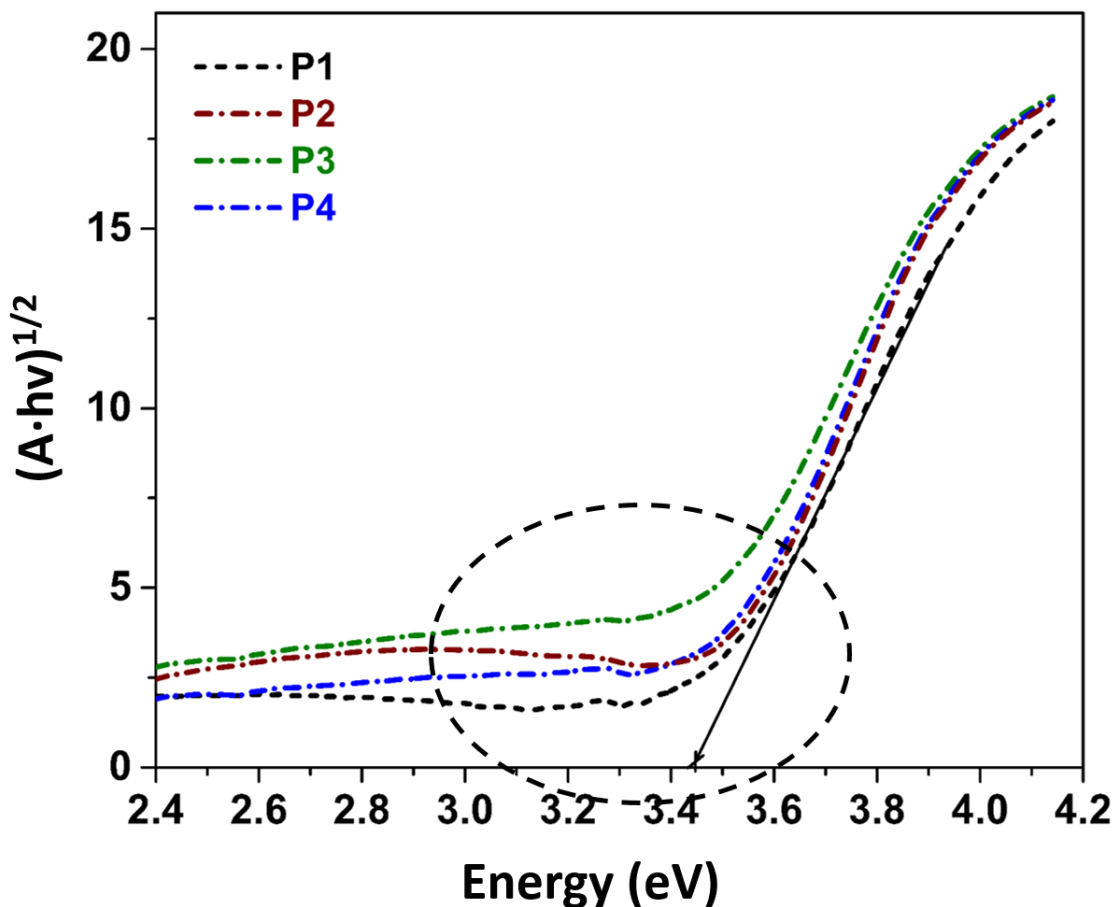


Figure 3.11. Representation of Tauc Plot for the calculation of the optical band gap of undoped and boron-doped TiO₂ samples, synthesised by AP-PECVD. P1 is the undoped TiO₂ sample.

For further understanding of the influence of boron doping in a TiO₂ system, by AP-PECVD, the photocatalytic performance of all samples was studied. The photocatalytic activities of the undoped (P1) and boron-doped TiO₂ films (P2, P3, and P4) were evaluated by the degradation of methylene blue (MB) in aqueous solution with an initial concentration of 10 $\mu\text{mol}\cdot\text{L}^{-1}$. The testing of photocatalytic properties of the films was performed by MB for two main reasons: (i) the project in which the described synthesis was included, the PlasmOnWire project, as described in **Chapter 1**, aimed to finally build a reactor combining a source of UV and/or visible light which would have connected several optical fibres coated with a photocatalytic coating and such a reactor would be aimed to be used for water decontamination or even water splitting; (ii) for the simplicity of the test and fast results compared to other methodologies for testing photocatalysis. The samples with a size of 2.25 cm² (1.5 cm × 1.5 cm) were drowned in 2 mL of the dye solution

(MB) in a 12 well plate (each sample in a different well). The well plate containing the samples and the dye was stirred using an orbital shaker (250 rpm) under irradiation of a 16 W black light lamps (Herolab; 365 nm, 2 mW·cm⁻²). **Figure 3.12**, describes the photocatalytic degradation of methylene blue under UV light (365 nm) for undoped TiO₂ and all B-TiO₂ thin films deposited on silicon wafers by AP-PECVD. As seen in **Figure 3.12b**, the degradation of MB is presented as the rate constant (k) of a pseudo kinetic first order reaction divided by the surface area of the samples. Given the equation $\ln(C_0/C)=K \cdot t$, where C_0 and C are the initial concentration and the concentration at certain point respectively, correlated to a certain time, t , and k is the rate constant of the reaction.³² The reaction was considered as pseudo first order reaction as the graphic representation was almost linear (**Figure 3.12a**).

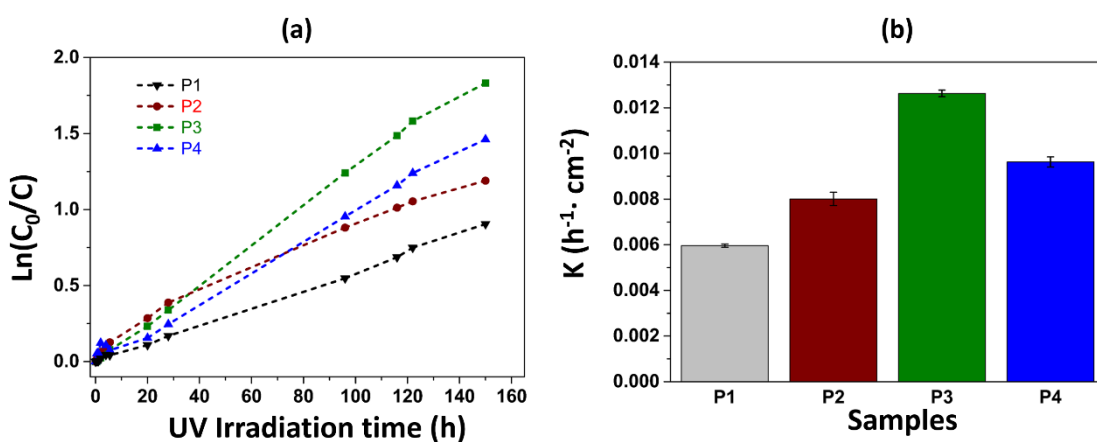


Figure 3.12. Photocatalytic test for all samples: (a) linear representation ($\ln(C_0/C)$ vs irradiation (UV) time) of the degradation of MB; (b) Bar diagram as function of rate constant of the reaction (h⁻¹·cm⁻²) of degradation of MB. Sample P1 is the reference (undoped); samples P2-P4 are boron-doped TiO₂ samples.

As it can be observed, all boron-doped samples presented a higher rate of photocatalysis when compared to the undoped TiO₂ sample synthesised under the same conditions, being reported the highest performance by sample P3. After repeated cycles of photocatalysis, the photoactivity of sample P3 was higher (**Figure 3.13**). As mentioned previously, the conditions for the synthesis of the coating on polymeric optical fibre (POF) were selected based on the photocatalytic performance of the samples, selecting the most photoactive

sample, as the content of boron and optical band gap were similar between all boron-doped TiO₂ samples.

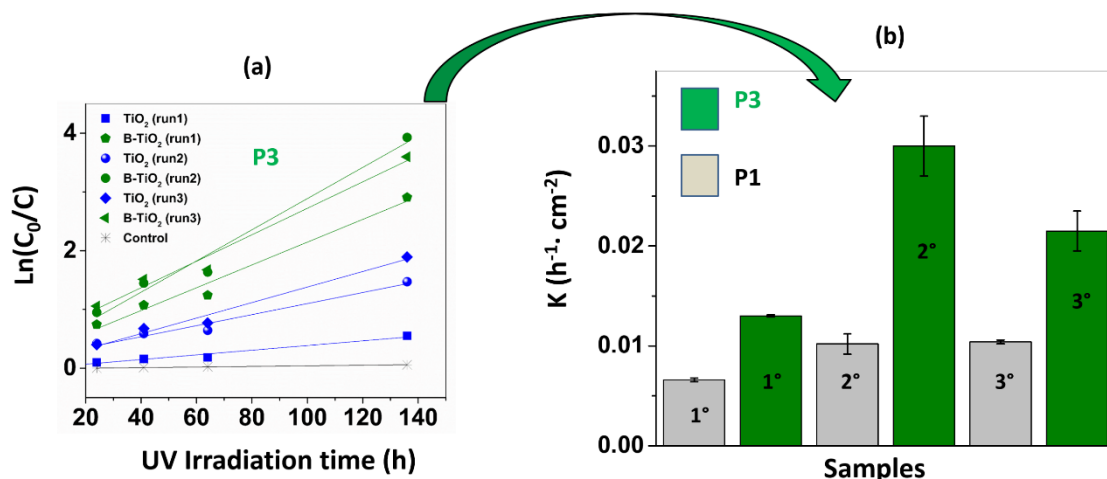


Figure 3.13. Photocatalytic test for P3 vs P1:(a) Linear representation of photodegradation of methylene blue (MB) for undoped TiO₂ and B-TiO₂ thin films as $\ln(C_0/C)$ vs irradiation (UV) time for B-TiO₂ thin film, sample P3 compared to undoped TiO₂ sample, sample P1; (b) Bar diagram as function of rate constant of the reaction ($\text{h}^{-1}\cdot\text{cm}^{-2}$) of degradation of MB. Different bars corresponding to different consecutive cycles of photocatalysis are represented as 1°, 2°, and 3°.

Typical synthetic methods used to produce B-TiO₂ photocatalytic materials, such as sol-gel and hydrothermal synthesis may produce materials with varying boron content and surface area, potentially affecting the performance of B-TiO₂ photocatalysts.⁶⁰ In contrast, the use of PECVD methods allow the synthesis of thin films with a homogeneous B content across the photocatalyst bulk, as well as comparable surface properties. Here, it was observed that the incorporation of B to the TiO₂ lattice was beneficial from a photocatalytic point of view. The dopant, boron, can be added in two different oxidation states, interstitially (B_{int}) sitting in the lattice of TiO₂ and substitutionally (B_{sub}) replacing O sites.^{63,64,154} When boron occupies a O-substitutional vacancy, the resulting B-TiO₂ appears as a metastable species, which decomposes over time,¹² whereas interstitial boron-doped TiO₂ has been reported to be very stable over time, several photocatalytic cycles and even after annealing process at relatively high

temperature.²⁷ The presence of both species ($B_{\text{int}} + B_{\text{sub}}$), within the TiO₂ lattice, has been previously reported.⁴⁵

When boron occupies simultaneously both positions within the TiO₂ lattice, the absorbance of UV light and, also the absorbance in the visible range of the spectra increases, even the B_{sub} disappears and decomposes in mild conditions. The higher photoactivity of TiO₂- B_{int} under UV light, as compared to that of TiO₂- $B_{\text{int+sub}}$ is due mainly to the delayed recombination processes even though the optical band gap is not significantly varied.⁴⁵ The enhancement of absorbance in the UV region increases the number of photogenerated electrons and holes to participate in the photocatalytic reaction, which can enhance the photocatalytic activity of TiO₂, whereas the band gap does not show anything more than a slight decrease in energy. The boron located at the interstitial site develops a shallow level, below the conduction band (CBM) due to the formation of a B-O-Ti bond. The shallow level seems to act as a trapping site for the photogenerated electrons to increase the lifetime and decrease the recombination process. This level hardly affects the band gap but plays a major role in trapping the photogenerated electrons.^{45,64}

In **Figures 3.12 and 3.13**, it can be observed that both boron-doped and undoped TiO₂ showed photoactivity under the UV light (365 nm). When comparing B-TiO₂ to undoped TiO₂ photocatalytic performances, after several cycles of photocatalysis for the same samples, a noticeable increase can be observed in the case of boron-doped anatase. There is a remarkable increase in the performance when comparing the first cycle of photocatalysis to the second one. The presence of carbon on the surface after the synthesis of the films was shown by XPS analysis, and, as previous cleaning of the films before the first run of photocatalytic performance was not conducted, the increase in performance for both, undoped and boron-doped samples, could be explained because of the self-cleaning process of the films, induced by the UV radiation in the aqueous medium. Moreover, in between the cycles, the samples were washed with ethanol and distilled water, to make sure no methylene blue was left on the thin films. The enhancement of photocatalytic activity under UV light of B-TiO₂ has been described previously and attributed to a narrowing in the band gap and the reduction of recombination rates for photoexcited e^-/h^+ .^{25,42,45,48,49,64} It has been commonly acknowledged that the photocatalytic process in TiO₂ proceeds

through two different pathways: i) the reaction of h^+ with surface H_2O producing hydroxyl radicals and/or ii) the reaction of e^- with O_2 creating superoxide radicals. These highly reactive radicals are responsible for the degradation of nearby organic pollutants like p-NP and MB dye. This process is mainly affected by the surface area of the photocatalyst, light absorption capability, and charge separation and transfer.⁷

3.4 Conclusions

Anatase and boron-doped anatase TiO_2 thin films were investigated and synthesized by AP-PECVD. The thin films were deposited on polymers (as well as on silicon wafers) which are sensitive to temperature, such as optical fibres (PMMA core based). The depositions were performed in one step, with no need of annealing or post-treatment to obtain the desired photoactive anatase phase of TiO_2 at low temperature. The POF fibres visually kept their mechanical properties after the deposition and did not melt.

Boron occupied most probably an interstitial position and even though the different boron-doped films were synthesised using different flow rates of the dopant placed in a separated bubbler (APCVD approach), the concentration of boron within the doped films was found to be very similar between all boron-doped samples, showing that by this technique and this specific approach, only films containing ~4% at. of interstitial boron could be synthesised. The optical band gap only showed differences in sample P3, which showed the highest rates for photodegradation of MB. All the films presented higher rates of photodegradation when compared to the undoped TiO_2 synthesised under the same conditions. When compared to the undoped TiO_2 films, the B- TiO_2 films presented higher rates of photodegradation of the dye. Nevertheless, the optical properties of the transparent films, both, undoped and boron-doped anatase seemed to be similar, with no significant change. On the other hand, further research has to be done in terms of controlling the exact amount of dopant, which will be incorporated within the anatase lattice by changing some of the deposition parameters. To the best of our knowledge, this was the first time that doped- TiO_2 was synthesized and doped simultaneously at atmospheric pressure by PECVD

and that anatase doped-TiO₂ films were deposited in one-step on a thermo-sensitive polymeric matrix such as PMMA optical fibre. In addition, the described approach could pave the way to the low-temperature synthesis and deposition of other functional crystalline transition-metal oxides, including transparent conductive oxides and thermochromic oxides, on a wide range of substrates such as textiles and polymers. The deposition of crystalline and doped anatase TiO₂ at atmospheric pressure and dry process operating at low temperature (< 160 °C), opens up to a situation plenty of possibilities for the coating of thermo-sensitive transparent polymeric substrates. In this chapter, the coating of POF with boron-doped anatase TiO₂ can ease the design and construction of a device to be used for water decontamination. Such a device could cover a large extension of polluted water. The light would pass through the POF and diffuse along it, avoiding the need of using a large source of light, saving cost of energy and material resources in the construction of such device. Also, developing the doping process by AP-PECVD, and using different types of dopants could make doped-TiO₂ to perform under visible light, as it has been reported previously.^{26,38,62,155}

Chapter 4

B-TiO₂ thin films synthesised by AA-PECVD: Aerosol-assisted approach

4.1 Introduction

In this **chapter 4**, a modified precursors' injection procedure is investigated in the perspective to finely tune the composition of anatase doped-titanium dioxide thin films grown at low temperature by AP-PECVD. Modified titania (TiO₂) thin films have become an extensively studied field due to their multifunctional applications.^{2,5,7} The most commonly studied approach for modifying the natural properties of TiO₂ has been the chemical modification through doping by using metal or non-metal species. The addition of dopant species to the lattice of TiO₂ results in a modification of its electronic structure, facilitating the use of lower energy photons to excite the material's band gap, and thus extending its photocatalytic response to the visible range.¹¹

Doping of TiO₂ with foreign elements, metal or non-metal, can also enhance the performances of TiO₂ through a narrowing of the band gap or by creating defect levels within the band gap.²⁶

Metal dopants and noble metal nanoparticles can significantly enhance the photocatalytic properties of TiO₂.^{17,21} It is well known that an appropriate amount of transition metal ions doped into TiO₂ can introduce electron capture centres

and may also change the crystallinity of TiO₂, resulting in the production some defects and thereby a decrease in electron/ hole recombination centres.^{30,102,156} Nonmetal or anion dopants do not cause a major narrowing of the band gap, yet these impurity states participate in trapping the charges to cause improvement in the photocatalytic activity.⁶¹ The doping of TiO₂ through the use of nitrogen species, has been widely explored.^{38,157} Unfortunately, despite the wealth of literature on N-doped TiO₂ materials, there is little consensus on whether this leads to an overall improvement in visible-light driven photocatalysis.^{39,158}

Therefore, alternative non-metal species have been extensively explored in the last few decades. Boron doping of TiO₂ has attracted attention because of its inductive creation of electron acceptor levels.⁴⁴ When boron is doped into the TiO₂ lattice, boron atoms can occupy two different positions, an interstitial position (B_{int}) and a substitutional position (B_{sub}) by filling up the oxygen vacancies.⁶³ When boron occupies an interstitial position within the TiO₂ lattice, the stability of the doped TiO₂ is far better when compared to the substitutional boron, which appear to be metastable and decompose into boron oxide.^{64,107}

Experimental evidence for the stability of these boron species was provided by Artiglia *et al.*¹⁰⁷ using different synthesizing techniques to produce B-TiO₂: B_{sub} with Ti (Ti-B), B_{sub} with O (Ti-B-O), B_{int} (Ti-O-B), and B₂O₃. On annealing, both the substitutional sites of B disappear to form B₂O₃ while the interstitial B is highly stable at all temperatures. Different techniques were adopted by Zaleska *et al.*⁶³ to dope B into TiO₂, and it was observed that activity strongly depends on the preparation conditions, method, and type of TiO₂ used. Theoretical calculations by Finazzi *et al.*²⁵ suggested that substitutional B is a metastable species and decomposes into interstitial boron or B₂O₃ by forming oxygen vacancy. They predicted that interstitial boron is the preferred site in TiO₂. It was also tentatively suggested that boron in interstitial site reduces Ti⁴⁺ to Ti³⁺ to facilitate separation of photoexcited electron/hole pairs and slow down their recombination.⁴¹ The electronic variation upon B-doping has been theoretically studied using density functional theory (DFT) calculations, they showed that boron in the substitutional site of oxygen can create midgap states and eventually cause the red shift in the absorption edge, whereas interstitial occupancy of B does not cause any significant variation in the band gap.^{42,43} The simultaneous presence of boron at both the interstitial and substitutional sites was first reported by Xue *et al.*²⁸ and

was later also confirmed by Wu *et al.*¹⁵⁹ and most recently by Patel *et al.*⁴⁵ The midgap states at different locations are formed by the charge balancing due to the interaction between interstitial and substitutional boron.^{42,45}

Nevertheless, the synthesis of B-TiO₂ has been focused on the formation of powders. Recently, thin films of B-TiO₂ were formed on metallic substrates by atmospheric pressure chemical vapour deposition (APCVD).⁴⁸ In that case, boron was incorporated in an O-substitutional position into the TiO₂, leading to remarkable rates of hydrogen production and more favourable photocurrent profiles when compared to undoped samples. Later, as presented and described in **Chapters 2 and 3**, thin films of purely interstitial boron-doped TiO₂ have been deposited by APCVD and atmospheric pressure plasma enhanced chemical vapour deposition (AP-PECVD) on glass and polymeric optical fibres, respectively.^{64,101,160} The synthesis of interstitial B-TiO₂ thin films presented some advantages: (i) as a thin film, in comparison to powders, it can be re-used easily and synthesised in a single one-step reaction; (ii) interstitial B is stable at all temperatures, which gives the doped films long-life performance; (iii) B_{int} enhances the UV absorption of TiO₂, thereby increasing its photocatalytic performance when compared to pure TiO₂; (iv) recently, it has been discovered that they present certain conductivity, and, as they are transparent they might be part of multifunctional layers for transparent conductive oxides and many other photocatalytic applications.¹⁶⁰

Thanks to the ability of enhancing the reactivity of either organic or inorganic precursors with plasma when depositing thin films, PECVD processes are considered as a versatile method allowing for the deposition of a broad range of materials at intermediate or low-temperature. In addition to this and when operated at atmospheric pressure, AP-PECVD processes becomes of great interest because of the advantages they offer, such as low cost, low temperature and easy implementation in a reel-to-reel process. Surfatron plasma generators are well known surface wave devices that provide a high plasma density at relatively low microwave power (≈ 200 W),¹⁶¹ with a high degree of ionization and an electron density which can reach a value up to 10^{20-21} m⁻³. The discharge of a surfatron device is highly stable due to the low deviation of the characteristic parameters in plasma.¹⁶² Non-doped and interstitial boron-doped anatase TiO₂ thin films have been successfully deposited on thermo-sensitive substrates by

using AP-PECVD approach employing a surfatron device, as shown in **Chapter 3** in this thesis.¹⁵² However, controlling the amount of dopant within the B-TiO₂ thin films is not straightforward from the results presented in Chapter 3

In the present Chapter, a new approach named Aerosol-Assisted Plasma Enhanced Chemical Vapour Deposition (AA-PECVD), for the one step synthesis and deposition of boron doped-TiO₂ thin films, with different atomic percentage of boron in the titania films is described. Titanium ethoxide (TEOT) and triethyl borate were used as Ti and B precursors, respectively, and mixed in the same solution. The aerosol was generated using an ultrasonic nozzle and carried into the deposition chamber with argon. The influence of boron concentration in the TiO₂ films on the morphological, structural, and optical properties of the deposited B-TiO₂ films were investigated with X-ray diffraction (XRD), Raman spectroscopy, scanning electron microscopy (SEM). X-ray photoelectron spectroscopy (XPS), Secondary Ion Mass Spectrometry (SIMS) and UV-Vis spectrophotometry. The photocatalytic activity of the deposited films under UV and visible light was demonstrated by the degradation of stearic acid and monitored by FTIR.

4.2 Experimental Section

4.2.1 Aerosol-Assisted Plasma Enhanced CVD (AA-PECVD) configuration

Previously reported, in chapter 3, the low-temperature (*i.e.* ≤ 200 °C) formation of interstitial boron-doped anatase TiO₂ thin films on polymer optical fibres,¹⁵² by AP-PECVD was achieved. Nevertheless, the study demonstrated that the selected dual injection mode solely led to an extremely narrow range of composition. Indeed, irrespective of the carrier gas flow through the boron isopropoxide bubbler (**Figure 3.1, Chapter 3**), the total concentration of boron in the B-TiO₂ thin films was found to be *ca.* 4% at.. Since the concentration of dopant is known to greatly influence the properties of the resulting materials and in order to gain a deeper understanding on the B-TiO₂ thin films, further investigation of a single injection mode for the titanium and boron precursors was performed. With the objective to form interstitial B-TiO₂ thin films with tuneable boron content, a

series of AA-PECVD experiments involving different concentrations of the titanium and boron precursors mixture (**Table 4.1**) were undertaken. To prevent any detrimental exchange of ligand in our precursors solution, triethyl borate (B(OCH₂CH₃)₃) was chosen as boron source for doping.

Table 4.1. Experimental parameters of the AA-PECVD depositions.

Sample	Carrier gases		Plasma parameters			Precursors	
	Ar flow	O ₂ flow	Surfatron-injection	Plasma power	Ar	Sol injected	[B]
	[slm]	[slm]	distance [cm]	[W]	[slm]	[μ L/min]	[mol. %]
Undoped	1	1	6	200	10	10	0
B-TiO ₂ (3%)	1	1	6	200	10	10	3
B-TiO ₂ (4%)	1	1	6	200	10	10	4
B-TiO ₂ (5%)	1	1	6	200	10	10	5
B-TiO ₂ (6%)	1	1	6	200	10	10	6

The plasma discharge was generated at atmospheric pressure inside a quartz tube of 5 and 7 mm inner and outer diameter, respectively (**Figure 4.1**), by applying a high-frequency electric field to a gas (Argon by Air Liquide, 99.99 %) flowing in a discharge tube by means of a wave launcher. The MW generator with a frequency of 2.45 GHz is operated in continuous mode with a power of 200 W. The wave launcher (Surfatron 80 by SAIREM) was powered via a coaxial cable and cooled by water. The discharge tube was cooled by compressed air and its end is at a distance of 3 cm from the launching gap. The flow of discharge gas, i.e. argon, was maintained at 10 standard liter per minute (slm) by a MKS mass flow controller.

For the undoped TiO₂ films, titanium ethoxide (Ti(OCH₂CH₃)₄, 80%) was diluted in toluene ($\geq 97\%$) to 0.5 mol·L⁻¹. In order to facilitate the injection of the precursor for the thin film deposition, the precursor flow rate was fixed at 10 μ L·min⁻¹ and carried toward an ultrasonic nebulizing nozzle operating at 120 kHz (Sono-Tek). The drizzle formed at the outlet of the nozzle was composed of droplets with diameters ranging between 20 μ m and 40 μ m and were carried by a mixture of gases, argon/oxygen, with a flow rate of 1 slm for each of the gases. For the boron-doped films, the boron precursor, triethyl borate (B(OCH₂CH₃)₃), $\geq 98\%$

was mixed with titanium ethoxide, at different boron concentrations (3, 4, 5 and 6 mol.%), keeping the total concentration of the solution constant (0.5 mol·L⁻¹). Then, the solution was injected under the same conditions as described above for the undoped TiO₂ films deposition. The post-discharge distance from the launching gap was equal to 6 cm after the initiation of the plasma discharge. All the depositions were carried out for 10 minutes, keeping constant all the parameters previously described. Films were grown on both, side glowing PMMA (2 mm of diameter; Luxylum) and silica core with polyimide cladding (0.8 mm diameter; CeramOptec) optical fibres (OFs) and double side-polished silicon wafers (2 × 2 cm) were employed as substrates. For the OF substrates, pieces of 1 m length were placed from the left to the right side of the experimental setup and through the discharge tube in a horizontal position. In the present work, all the deposition experiments were performed in the static mode for a total duration of 3 min. The characterized area of the coated-OFs was located in the post-discharge region (from 5 to 8 cm from the launching gap) and close to the precursor injection outlet (*i.e.* 6 cm from the launching gap). Silicon wafer substrates were cleaned using absolute ethanol (97 %) and dried with nitrogen prior to use. In the case of the silicon substrates, during the depositions, the substrate was placed in the deposition chamber in the same horizontal position as OF substrates (**Figure 4.1**), at 6 cm from launching gap.

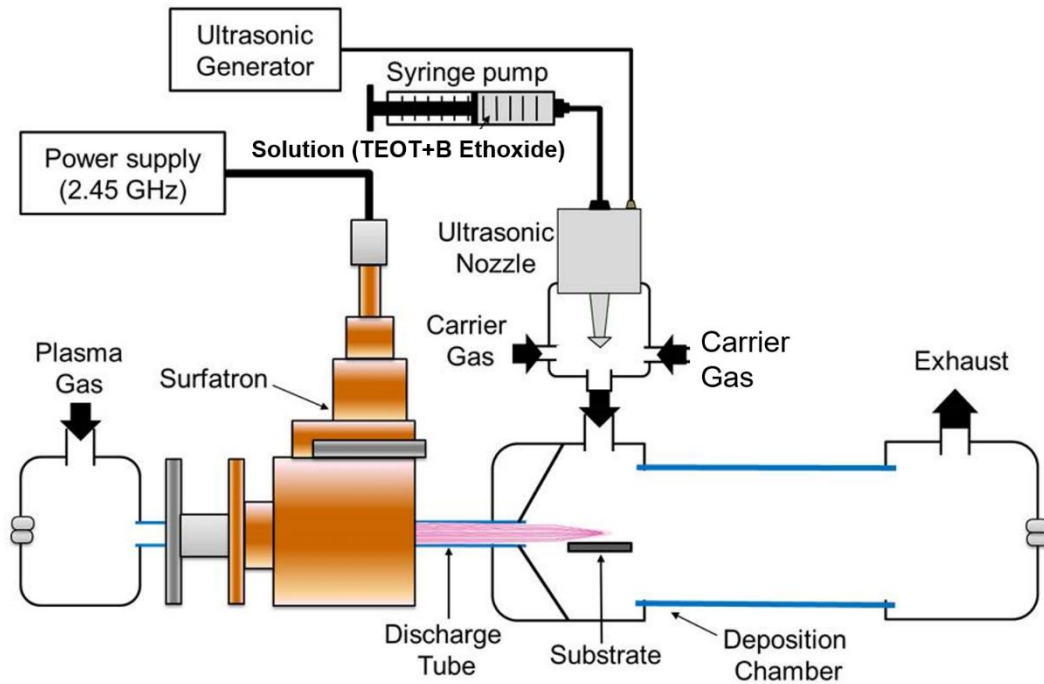


Figure 4.1. Schematic of the AA-PECVD setup for boron doping of TiO₂. Planar substrate was chosen for this representation. When the deposition was performed on optical fibre substrates, the polymeric optical fibre was passed through the reactor, as shown in figure 3.1 of chapter 3.

4.2.2 Analytical Methods

For the full characterisation of the films synthesised by AA-PECVD, several analytical techniques were employed: X-ray diffraction (XRD) patterns of the films were obtained using a Lynxeye XE Bruker-Axs D8 diffractometer. Cu X-ray source, monochromated ($K\alpha_1$, 1.54 Å). The Joint Committee on Powder Diffraction Standards (JCPDS) was used to determine the crystal structure adopted. The lattice parameters and average crystal size was determined using a Le Bail model using the GSAS-EXPGUI software suite.⁶⁵ Raman spectroscopy was carried out using a Renishaw 1000 spectrometer equipped with a 514-nm laser.

Characterisation of the chemical profile of the thin films was carried out by Dynamic Secondary Ion Mass Spectrometry (D-SIMS) in a Cameca SC-Ultra instrument in positive ion mode, by a bombardment with Cs⁺ ions, having an impact energy of 1.0 keV.

X-ray photoelectron spectroscopy (XPS) was used to determine the composition of the films and spectra were recorded on a Kratos Axis Nova spectrometer equipped with a monochromated Al K α X-ray source and delay line detector. Survey spectra were recorded with energy of 160 eV and higher resolution spectra were recorded at 80 eV. The analysis of the spectra and the fitting were performed by adjusting the position of the C 1s (adventitious carbon), tooled by the software CasaXPS.

UV/visible spectroscopy was performed using a double monochromated PerkinElmer Lambda 950 UV/vis/NIR spectrophotometer in the 300–2500 nm range. Reflectance spectra were recorded for different positions in the range 300–2500 nm on a Helios double beam instrument standardized relative to a silicon mirror, which allowed the thickness of the films to be also determined *via* the Swanepoel method.

The morphology of the films was studied by Scanning Electron Microscopy (SEM). The images were taken using JEOL 6301 (5 kV) and a JEOL JSM-6700F field.

4.2.3 Photocatalytic Test

The films synthesised in this chapter were photocatalytically evaluated by photodegradation of octadecanoic (stearic) acid (95%, Sigma-Aldrich). A thin layer of stearic acid was applied on the surface of samples by spin-coating, using 5 μ L of stearic acid solution (0.05 M) in chloroform, at 10000 rpm during 30 s. The photocatalytic activity of the samples was measured under UVA (Vilber-Lourmat, 2 \times 8 W, 365 nm, 2 mW cm⁻²) illumination.

To monitor the degradation of the overlain stearic acid, a PerkinElmer RX-I Fourier transform infrared (FTIR) spectrometer was used.

For the visible light test, a white light lamp (λ_{max} =590 nm, 2 mW/cm²) was used.

4.3 Results and discussion

The results presented here are based on the synthesis of several batches of samples and the selection of the most representative. I decided to try a different approach, similar to AACVD because of:

- AACVD approach it simplifies the vapour precursor generation and delivery method as compared to the conventional APCVD method which uses a bubbler/vaporiser method.
- The use of single source precursors (titanium and boron ethoxide) which provide good molecular mixing of chemical precursors which enables the synthesis of multicomponent materials with well controlled stoichiometry. If I could control initially the concentration in solution, I was “sure” I was adding more or less boron when the reaction takes place.
- It allows rapid formation of the deposited phases at relatively low temperatures due to the small diffusion distances between reactant and intermediates.
- It is a relatively “low cost” process as compared to conventional CVD because the AACVD process can be performed in an open atmosphere for the deposition of oxide and some less oxygen sensitive non-oxide materials without the need of any sophisticated reactor. As we were working in the patent for the process at the same time, I wanted to choose the method which would be the best fit for scaling up our open plasma reactor.

In this section, the results obtained from all the analytical techniques (XRD, Raman, XPS, UV-Vis, etc) and tests run to determine the structure, composition and the functional properties of the undoped and boron-doped films synthesised by AA-PECVD will be discussed in detail.

4.3.1 Structure and morphology

As mentioned before in **section 4.2.2**, one of the techniques used to study the structure and crystallinity of the films deposited by AA-PECVD was XRD.

The dopant content is known to have a significant influence on the crystallinity of the doped materials (phase, cell parameters and grain size) and XRD of the reference (undoped) and boron-doped TiO₂ samples was carried out (**Figure 4.2**).

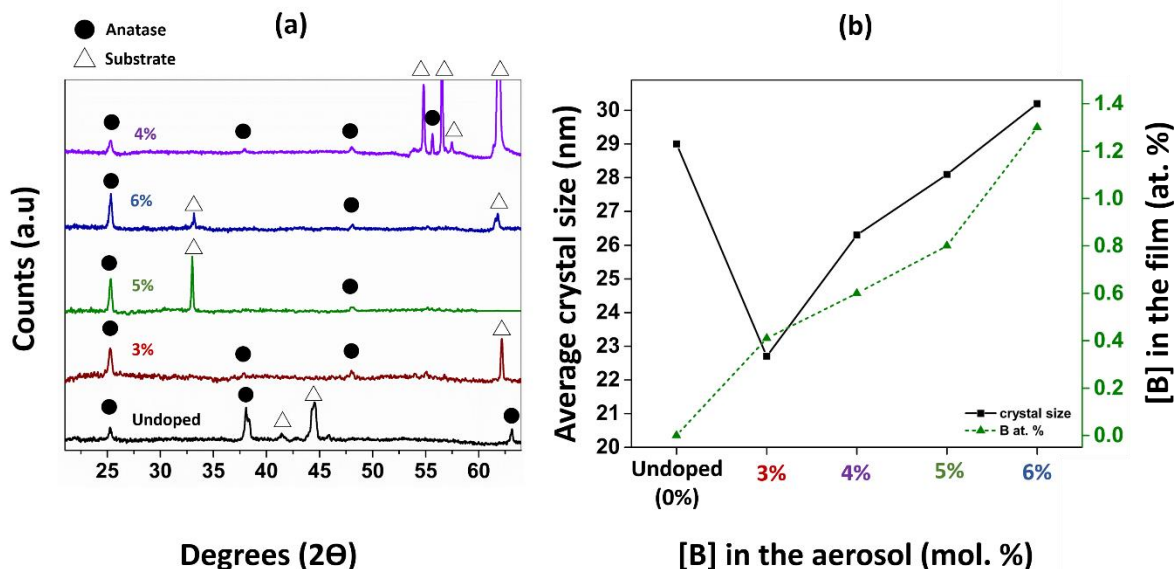


Figure 4.2. (a) XRD patterns of boron-doped TiO₂ thin film samples (3, 4, 5 and 6 mol. % of boron in solution) compared to the undoped TiO₂ thin film, deposited on silicon wafers; (b) graphic representation of average crystal size vs the molar and atomic (%) concentration of boron in the solution of the precursor and in the resulting films, respectively.

The XRD patterns of undoped and B-TiO₂ thin films deposited on double polished silicon wafers all revealed the characteristic pattern of the anatase polymorph of TiO₂ (**Figure 4.2a**). Interestingly, the main diffraction peak of anatase, corresponding to *hkl* (101), is known as being mostly responsible for the photocatalytic performance of anatase TiO₂,¹⁶³ and it was observed in all the samples. The orientation growth of the films by AA-PECVD already shows differences when compared to films synthesised by AP-PECVD described in chapter 3. When films are grown by AP-PECVD (using a separate bubbler for the dopant) the diffraction peak corresponding to (004) plane was the preferred orientation (**Figure 3.4b**), whereas, when the films are grown by AA-PECVD the preferred orientation changes. In the case of the undoped TiO₂ sample, as

expected and observed previously, the preferred orientation was (004), around $\sim 38^\circ$ two theta. When doping by using the different solutions containing different concentrations of boron (mol.%), the preferred orientation was (101). Several peaks, corresponding to the silicon wafer substrate can be also seen in all the samples. Due to the growth orientation of the films, cell parameters of all the samples could not be obtained due to insufficient data. Nevertheless, in the case of B-TiO₂ (4%), the necessary peaks were found and after applying le bail mode, tooled by GSAS, the cell parameters of the film were found to be $a=3.7815 \text{ \AA}$, $c=9.4951 \text{ \AA}$ and the cell unit volume was 135.78 \AA^3 . These values correspond well to the literature values of anatase TiO₂ thin films synthesised by APCVD.¹⁰⁶ When observing the position of the (101) diffraction peak, a small shifting to a higher degree (2θ) can be noticed when comparing boron-doped TiO₂ thin films to the undoped anatase reference.

XRD shifting of the (101) peak in doped anatase thin films can be explained by changes in the lattice of TiO₂ induced by the dopant, i.e. boron can either occupy an oxygen vacancy (substitutional boron) or it can be incorporated interstitially (interstitial boron) within the TiO₂ lattice.⁶³ It was reported that when annealing, the substitutional sites of B disappear to form B₂O₃ while the interstitial B is highly stable at all temperatures, suggesting that interstitial boron is the preferred and the most stable site in TiO₂.¹⁰⁷

Therefore, the shifting of the (101) diffraction peak to a higher 2θ angle, suggested that somehow the lattice parameters are shrinking and becoming smaller due to the presence of substitutional boron.^{45,63} In the case of boron replacing O (B_{sub}), the unit cell volume is expected to decrease since the radius of B³⁺ (0.023 nm) is smaller than O²⁻ (0.132 nm) whereas the occupancy of the interstitial position (B_{int}) induces the lattice expansion to shift the diffraction to a lower 2θ angle.

Nevertheless, the reported shifting was not as noticeable as the one that the films showed by Raman spectroscopy (**Figure 4.3**).

The average particle/crystal size was obtained from the fitting of the main diffraction peak (101) and was based on the Scherrer formula: $D=(K\cdot\lambda)/(\beta\cdot\cos\Theta)$; where K is the shape factor, λ is the wavelength, β is the line broadening at half the maximum intensity (FWHM), after subtracting the instrumental line

broadening, in radians. Θ is the Bragg angle (in degrees). The values were 29 nm for the undoped TiO₂ film and compressed between 22.7 and 30.2 nm for the B-TiO₂ films (**Figure 4.2b**). The initial decrease in the average crystal size (B-TiO₂ (3%)), is a clear indication of boron occupying the substitutional vacancies. **Figure 4.1b**, shows that as doping with boron remains at very low concentrations, the average particle size noticeably decreases when compared to the undoped TiO₂ film. In contrast, as the concentration of boron in the B-TiO₂ films increased, the average crystal size increased as well, indicating the presence and contribution of interstitial boron, expanding the TiO₂ lattice and coexisting with substitutional. ⁶⁴

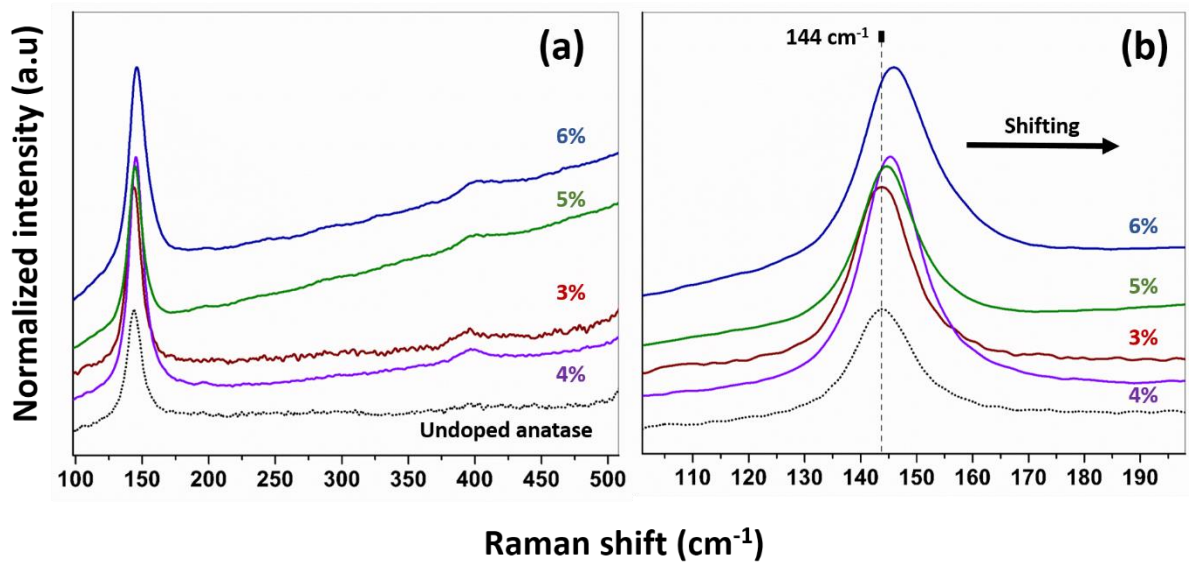


Figure 4.3. (a) Raman spectra of boron-doped TiO₂ thin film samples (3, 4, 5 and 6 mol. % of boron in solution) compared to the undoped TiO₂ thin film; (b) zoomed E_g band, showing the shifting of the peak for all of the samples.

Raman spectroscopy confirmed the formation of anatase TiO₂ for the boron-doped and the undoped TiO₂ thin films (**Figure 4.3**) and the characteristic E_g

band for anatase was found, in the case of undoped TiO₂ thin film, at 144 cm⁻¹, which corresponds with the values that can be found in the literature.⁹⁹ When the E_g band was observed in close range (**Figure 3b**), a shifting of the characteristic band can be noticed. The peak was shifted to a higher value as the molar concentration of boron in solution increases. In the case of B-TiO₂ 6 mol.%, the band was found at 146.1 cm⁻¹. This linear blue shifting of the E_g band for TiO₂ has been previously reported when doping TiO₂ with boron and other elements^{29,48,64,109} This shifting appears when the frequency of phonons interacting with the incident photons increases. Phonon confinement can be caused by different factors, including an expansion in the unit cell volume caused by the introduction of a dopant. An example of this is in W-doped TiO₂, where a direct correlation was drawn between W concentration and the extent of the E_g shifting.⁴⁸ Another mechanism by which phonon confinement is reported to occur is through a reduction in particle size.^{50,164}

In the case of the results obtained by XRD and Raman spectroscopy presented here, a combination of the presence of a dopant, as well as a decrease in the lattice parameters compared to non-doped TiO₂ is likely to account for the large blue shift.⁴⁸

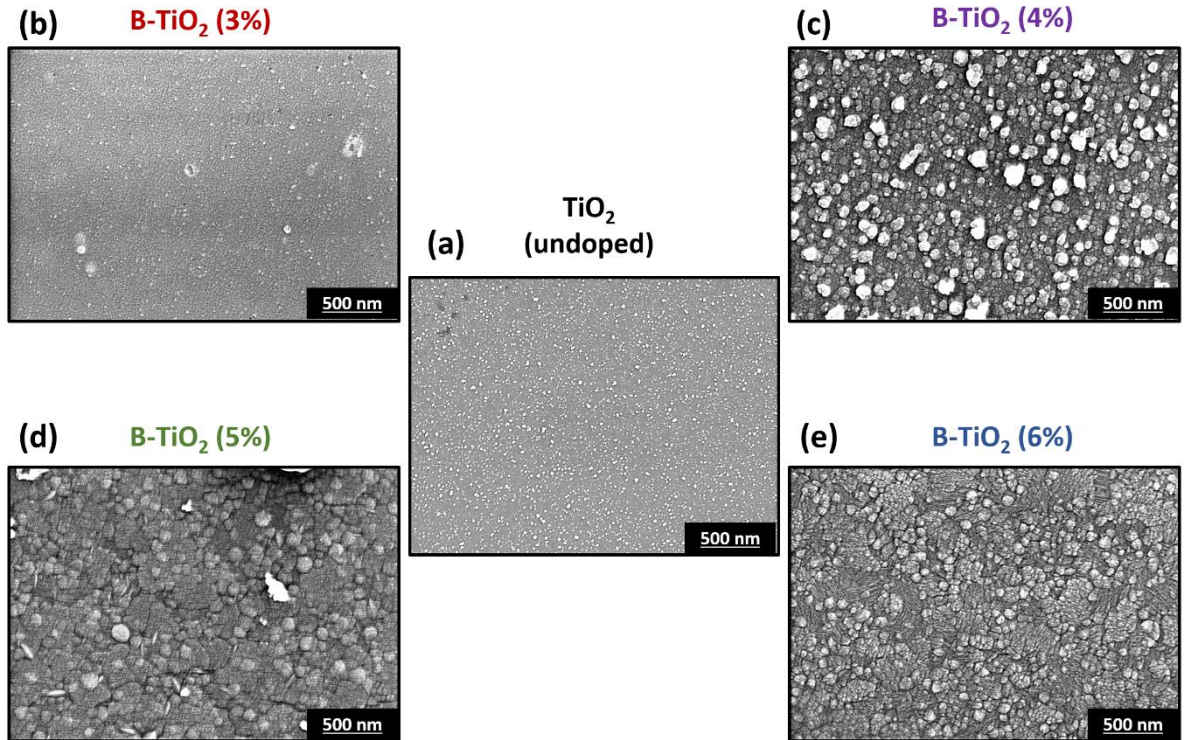


Figure 4.4. SEM images of (a) undoped TiO₂ and (b, c, d and e) B-TiO₂ thin films. 3%, 4%, 5% and 6% represent the mol. % of boron in solution, when preparing the precursor.

To study the possible changes, as well as the influence of the incorporation of the dopant on the morphology of the films, SEM analysis were carried out (**Figure 4.4**). The noticeable influence of interstitial boron doping on the surface morphology of TiO₂ thin films has been reported previously and can be seen in **Chapter 2** of this thesis.^{64,152} In **Figure 4.4a**, the undoped thin film presented a surface formed of spherical particles, equally distributed, as previously reported when depositing B-TiO₂ by AP-PECVD.¹⁰¹ Examining the SEM images showed some discrepancies between the undoped TiO₂ and the boron-doped TiO₂ thin films deposited by AA-PECVD.

In the case of the sample B-TiO₂ 3 mol.% (**Figure 4.4b**), when compared to the undoped sample, both samples showed similar morphology and the influence of the doping on the morphology seem to be limited. When the concentration of boron increases by only 1 mol.%, as shown in **Figure 4.4c**, the B-TiO₂ thin film synthesised by using a solution of 4 mol.% of boron, showed a different

morphology when compared to the undoped TiO₂. The surface of the film was composed of agglomerations of spherical shaped particles, that on comparison to the undoped TiO₂ film, the particles were larger (ca. 100 nm to 250 nm). In the case of B-TiO₂ (5 mol.%) thin film, as observed in **Figure 4.3d**, the spherical particles were present, in a range of sizes similar to the particles in sample B-TiO₂ (4 mol.%). Nevertheless, some areas showed a planar shaped deposition, probably formed by the agglomeration of smaller particles, providing the appearance of a smooth coating.

In the case of B-TiO₂ (6 mol.%) (**Figure 4.4e**), the surface experienced a remarkable change of morphology. Agglomerations of prism-like shaped particles can be seen in the SEM image. The prism-like shaped particles have been described previously (**Chapter 2**) in doped-TiO₂ thin films when doping with boron.⁶⁴

Consequently, these appreciable and noticeable changes in the morphology of the surface of the boron-doped thin films, and the shifting of the E_g band observed in the Raman spectra, support the presence of interstitial boron, incorporated as dopant in the anatase TiO₂ structure.^{45,48,63,64,107}

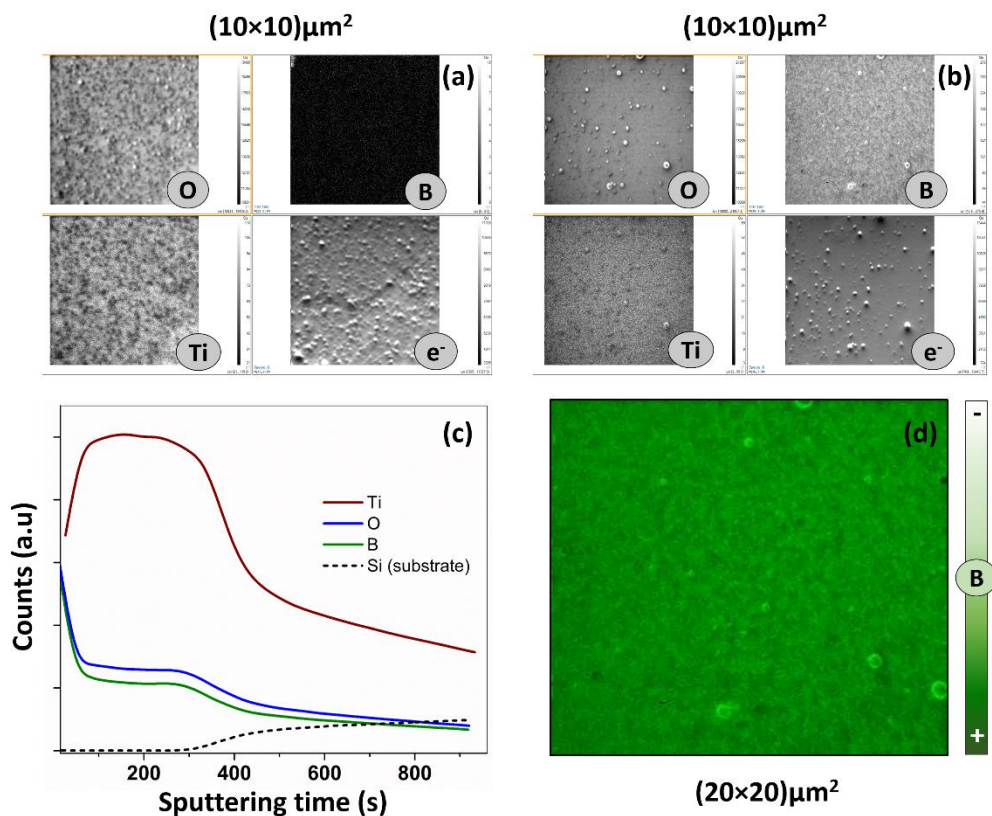


Figure 4.5. SIMS analysis of undoped and boron-doped TiO₂ thin films synthesised by AP-PECVD: SIMS mapping, 10x10 μm², of the selected elements (O, Ti and B) for undoped TiO₂ (a) and boron-doped TiO₂ (b) thin films; (c) Depth profiling of the selected elements (O, Ti, B and Si) for the B-TiO₂ film; (d) SIMS mapping of boron (coloured scale) of a 20x20 μm² image of B-TiO₂ thin film.

The applicability of the described AA-PECVD approach for the low-temperature synthesis and deposition of doped anatase TiO₂ thin films was demonstrated above through XRD, XPS and Raman. In order to evidence the homogeneity of the B-TiO₂ films, which is an essential aspect for potential applications, a mapping and profile analysis of the samples was carried out by secondary ion mass spectrometry (SIMS). The selected elements to be detected by the mapping were Ti, O and B, as well as for the profile in depth analysis, which includes Si as well to be detected, as the main component of the silicon wafer substrate. In **Figure 4.5a** and **b**, in black and grey scale, it can be observed that boron was not detected in the case of the undoped TiO₂ sample (**Figure 4.5a**), whereas in the case of the boron-doped sample, boron can be seen and detected (**Figure 4.5b**). Observing both surfaces imaging, undoped and boron-doped TiO₂, the uniformity and homogeneity of the films was noticeable.

The distribution of the elements was shown to be equal, both for the undoped TiO₂ and for the B-TiO₂ films synthesised by AP-PECVD under the same experimental conditions. The images where electrons were detected, confirmed and showed that the differences relating to the concentration and distribution of the elements are negligible. The SIMS imaging analysis itself supports the observations by SEM, where even the surface of the samples was changing noticeably when the concentration of the boron precursor was changed in the solution, the different morphologies observed remain uniform along the sample surface. For instance, in **Figure 4.5d**, a larger section (20x20 μm²) of the selected B-TiO₂ sample, shows the detection of boron (in a green scale). In the image it can be confirmed and the uniformity of the topography of the B-TiO₂ thin film seen. To obtain the characteristic in-depth profile spectra of the B-TiO₂ sample, a primary beam of Cs⁺ was employed to sputter the film as a function of time (**Figure 4.5c**). As it can be seen in **Figure 4.5c**, Ti, O and B were detected with initial different counts (surface), and they remain stable over sputtering time (bulk

of the film) until they started to decrease, as Si signal increases (reaching the substrate). The imaging of the selected elements and the detection of such elements by sputtering the film, demonstrated the presence of the dopant, boron, and its homogenous distribution on the surface and within the bulk of the B-TiO₂ thin film.

To elucidate the nature of the element within the TiO₂ lattice, either substitutional or interstitial boron, XPS measurements of the samples were performed in both surface and bulk. The Ti 2p peaks, located at binding energies of 458.9 eV and 464.6, were identified as Ti-O bonds of Ti⁴⁺ in TiO₂.⁵ No other Ti⁴⁺ environment or reduced Ti³⁺ species were detected. The O 1s peak, located at 530.4 eV is also consistent with the formation of TiO₂.¹⁵¹ All Ti 2p and O 1s spectra were similar to spectra shown in **Chapter 3, section 3.3.1**.

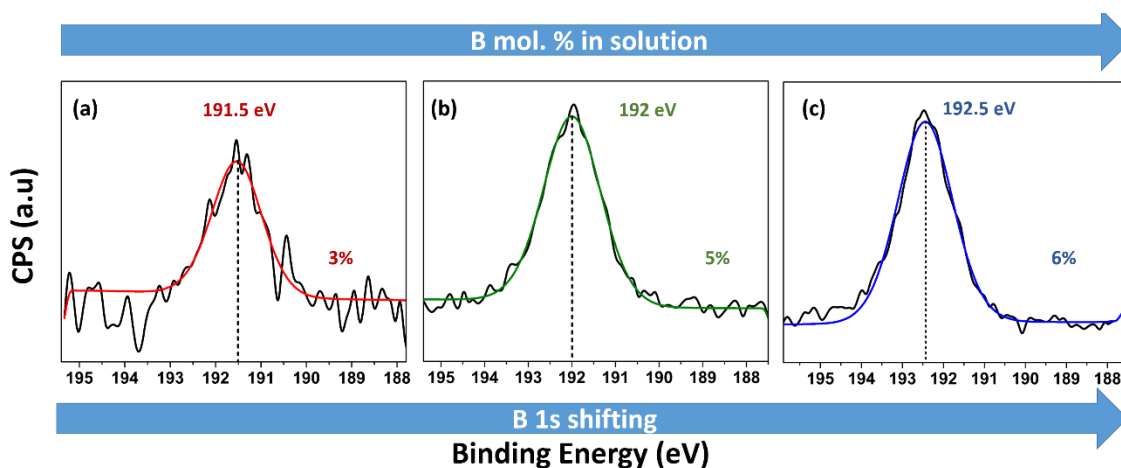


Figure 4.6. B 1s XPS spectra of: (a) B-TiO₂ (3%); (b) B-TiO₂ (5%) and (c) B-TiO₂ (6%). Dotted straight lines indicating the position of the peaks after deconvolution.

The chemical shifting in XPS is produced by a change in binding energy of a core electron of an element due to a change in the chemical bonding of that

element.¹⁵¹ In a qualitative view, core binding energies are determined by: (i) electrostatic interaction between it and the nucleus, and reduced by: (ii) the electrostatic shielding of the nuclear charge from all other electrons in the atom (including valence electrons). Removal or addition of electronic charge as a result of changes in bonding will alter the shielding, such that withdrawal of valence electron charge increases the binding energy (BE) (i.e. oxidation) and addition of valence electron is translated as charge decrease in BE.

The position of the B 1s peaks and the shifting which the peaks experienced as the concentration of boron increases (from 0.4 to 1.3 at.% in the films) can be explained by the transition from a mixture of interstitial and substitutional boron to a purely contribution of interstitial boron as preferred site. The concentration (at.%) of B_{sub} is beyond the detection limits of the technique (≈ 0.4 at.%) when it comes to peak deconvolution. However, the shift of the BE suggests the transition from a mixture of both, B_{int} and B_{sub}, to a purely interstitial B-TiO₂.

4.3.2 Functional properties

The following section provides a discussion of the optical and photocatalytic properties of the undoped and boron-doped TiO₂ films deposited by AA-PECVD.

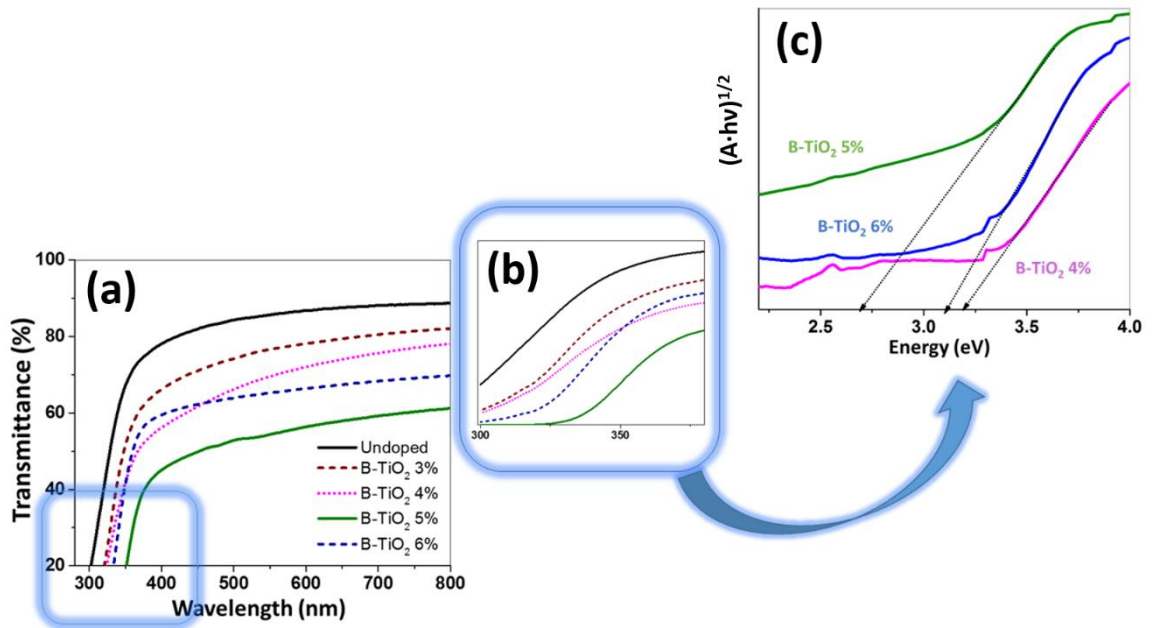


Figure 4.7. (a) Transmittance spectra of B-TiO₂ thin films compared to undoped TiO₂ film; (b) zoomed transmittance/adsorption edge from previous graph and (c) Tauc plot for the calculation of the optical band gap (4%-6% B-TiO₂ samples).

In the case of optical properties, UV-Visible spectrophotometry was employed to characterise the B-TiO₂ thin films synthesised by AA-PECVD and to compare them with those of undoped TiO₂. For this analysis, the samples were deposited on glass microscope slices, following the same procedure and by using the same conditions as used to deposit on silicon wafers. In **Figure 4.7a**, the transmittance spectra for all the boron-doped films is shown, as well as for the undoped anatase TiO₂ film. The spectrum of undoped TiO₂ showed an absorption edge close to 310 nm, which matches the values previously reported in the literature.^{5,113} When observing the transmittance spectra of the B-TiO₂ thin films, the spectra absorption edges, compared to the one of undoped TiO₂, shift to a higher wavelength value, being relatively close to 400 nm (\approx 350 nm) in the case of B-TiO₂ (5 mol.%). Indeed, Tauc plot analysis (**Figure 4.7c**) showed a change in the band gap more noticeable in the case of B-TiO₂ (4 mol.%, 5 mol.% and 6 mol.%) when compared to the experimental value obtained for undoped anatase TiO₂ (\approx 3.45 eV). Surprisingly, the lowest value for the band gap was found in B-TiO₂

(5 mol.%), about 2.69 eV when it was expected to be lower in the case of B-TiO₂ (6 mol.%), where it was found at 3.13 eV. For the rest of B-TiO₂ films, 3 mol.% and 4 mol.%, the optical band gap values were 3.41 and 3.19 eV, respectively. The changes in the optical properties of the boron-doped TiO₂ samples were then correlated to the amount of boron precursor in the solutions used for the AA-PECVD deposition. The modification of the optical band gap of TiO₂ by doping with boron has been reported recently by N. Patel *et al.*, where at low concentration of B-doping (1% at.), a minor decrease in band gap was observed, reducing from 3.15 eV for pure TiO₂ to 3.0 eV. However, in the case of 2% at. B-doping the presence of two absorption edges (2.4 and 2.2 eV) was clear from the Tauc plot, suggesting the possible existence of a localized state deep in the band gap causing a two-step transition.

When the B-TiO₂ is purely interstitial, it does affect slightly the optical properties of anatase, whereas for B_{sub}-TiO₂, the band gap and the light absorption of TiO₂ are more noticeably modified.^{43,45,160} The results obtained by Tauc plot analysis supported the observed shifting in Raman and XRD, which indicates the incorporation of boron within the TiO₂ and its influence, as well as the possibility of having both doped species, B_{sub} and B_{int}-TiO₂, coexisting. Previous DFT calculations for TiO₂, containing B_{int}, B_{sub}, and B_{int+sub} revealed that the two localized deep levels were formed in the mid gap region which were responsible for these optical transitions for TiO₂-B_{int+sub}. Reported photoluminescence (PL) emission spectra showed that the shallow level created below the conduction band is able to decrease the radiative recombination process in B_{int}-TiO₂ by trapping electrons and prolonging the lifetime of charge carriers, suggesting better charge mobility and a lower recombination rate.⁶⁴

While both the synthesis and deposition of crystalline TiO₂ and doped TiO₂ from a single step process operating at low temperature represent a challenge for the scientific community,¹⁶⁵ we successfully formed homogeneous boron-doped TiO₂ thin films on polymer substrate. The use of a single injection for our titanium and boron precursors mixture allow us to tune the composition of our B-TiO₂ thin films. The combination of the results obtained by XRD, Raman, XPS and the UV-Vis spectra confirmed the presence of both species, interstitial and substitutional boron incorporated to the anatase TiO₂ lattice, with a major contribution of B_{int}.

These results are interesting when compared to different approaches of CVD synthesis of B-TiO₂. By APCVD, thin films of B-TiO₂ can be synthesised containing either substitutional boron or interstitial, both of them, inducing completely different changes in properties and morphology of the films.^{48,64} Recently, it was reported for the first time the synthesis of B_{int}-TiO₂ thin films by AP-PECVD, corresponding to **Chapter 3** of this thesis.⁶⁴ In that case, the boron source was boron isopropoxide, which was placed in a bubbler and lead to thnebuliser by a carrier gas (Ar). The resulting boron-doped films showed a higher photocatalytic performance when compared to the undoped TiO₂ films, synthesised under the same conditions. No narrowing of the optical band gap was reported. In this work, the different approach to synthesise the B-TiO₂ films using a prepared solution combining the titanium and boron precursors, even by using the same technique (AP-PECVD), it has resulted in the formation of B_(sub+int)-TiO₂ thin films, with a narrowing of the optical band gap.

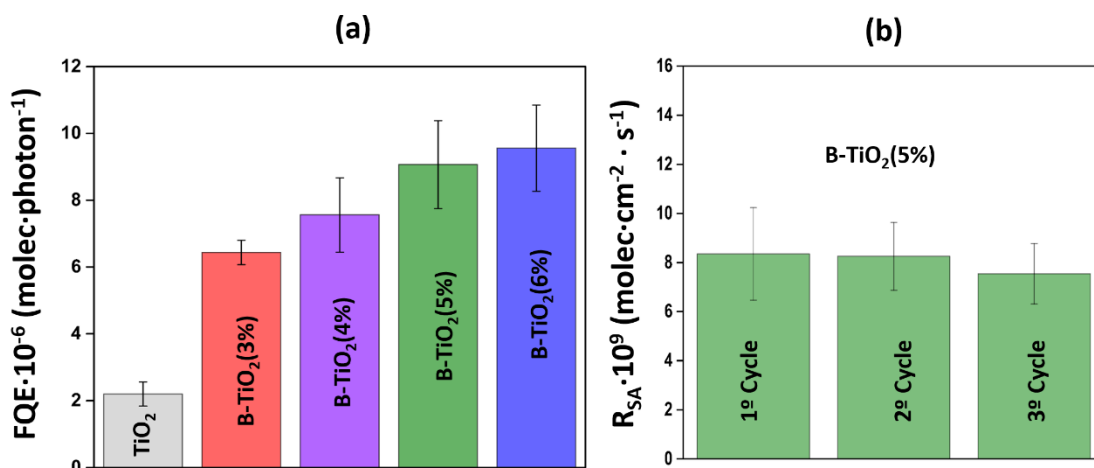


Figure 4.8. (a) average formal quantum efficiencies (FQE) obtained during photodegradation of stearic acid under UV irradiation of B-TiO₂ samples compared to undoped TiO₂ synthesised under the same conditions (reference); (b) visible light activity, given as rate of degradation of stearic acid (R_{SA}), of selected B-TiO₂ (5%) film. The visible light test is presented for 3 consecutive cycles of photocatalysis.

As for understanding and proving the functional properties of boron-doped TiO₂ films synthesised by AA-PECVD, a photocatalytic test was performed by using stearic acid as a model molecule for an organic pollutant. All boron-doped TiO₂ samples presented a higher rate of photodegradation, under UV light (365 nm) in comparison to the undoped TiO₂ sample (reference), with all samples synthesised by AA-PECVD under the same conditions (**Figure 4.8a**).

As observed in **Figure 4.8a**, the photocatalytic performance of the boron-doped TiO₂ samples increased as a function of dopant content, meaning that the most photoactive doped film, under UV light, was the sample B-TiO₂ (6 mol.%). This sample has been synthesised using an initial concentration of 6 mol.% of boron in solution, obtaining a total concentration of B in the film of ~1.35% at.

One of the doped samples, B-TiO₂ (5 mol.%), showed certain photoactivity under visible light. The test was repeated up to five times, cleaning the film in between cycles using ethanol and water, exposing the film after to UV light in the presence of wet air (48h). The several repetitions of the photocatalytic test shows as well the chemical stability of the doped samples, which corroborates the existence of interstitial boron, as proven previously in **Chapters 2 and 3**.^{45,64,160}

The absorption of this sample in the visible light and therefore the photoactivity shown is correlated with the observations of changes and shifting in the optical band gap (**Figure 4.7c**). The XPS spectrum of this sample, B-TiO₂ (5 mol.%) did not show any presence of Ti³⁺ on the surface and boron was attributed as interstitial (~192 eV).

From the theoretical and computational analyses, we showed, in **Chapter 2**, that under *Ti-poor/O-rich* conditions the Fermi level could be trapped ~2 eV above the VBM, indicating that electrons trapped at this level could be excited by visible light into the CBM thus increasing the visible light activity.

4.4 Conclusions

A series of undoped and boron-doped anatase TiO₂ thin films of different concentrations were deposited on different substrates (glass and silicon wafers) by one-step AA-PECVD. The content of the dopant, *i.e.* boron, was varied in solutions from 3-6 mol. % (triethyl borate in toluene). XRD and Raman studies showed that anatase was obtained in the undoped and all boron-doped TiO₂ samples. XPS and D-SIMS analyses, showed that boron was incorporated within TiO₂ as mostly interstitial, being that form the most stable of boron-doped TiO₂.^{45,63} All samples presented different concentrations (% at.) of boron within the films. The incorporation of interstitial boron induced a noticeable change in the morphology of the doped-films, seen by SEM imaging and in the average particle size.

The optical band gap, obtained by UV-Vis spectroscopy (Tauc plot method) showed changes in the boron-doped TiO₂ samples when compared to the undoped TiO₂ film. A shift to a higher wavelength value was observed, which in the case of sample B-TiO₂ (5 mol.%) was close to 400 nm (~350 nm). In the case of this sample, visible light absorption/response was found. The photocatalytic performance of all B-TiO₂ films under UV light (365 nm), during the degradation of stearic acid, was enhanced, being much higher and noticeable in the case of sample B-TiO₂ (6 mol.%), which contains around 1.35% at. B.

Chapter 5

Conclusions and future work

5.1 Conclusions: summary of results

As far as our knowledge can reach, this thesis presented and reported for the first time the synthesis of interstitial boron-doped anatase TiO₂ thin films of different concentrations by one-step APCVD, AP-PECVD and AA-PECVD. The use of different synthetic methodologies, approaches and techniques allowed for the deposition of functional interstitial B-TiO₂ on different types of substrate, such as float glass, silicon wafers, and the most important achievement, the successful deposition on polymeric optical fibres, *i.e.*, PMMA. When using APCVD, the content of the dopant (boron) was varied by increasing the mass flow rate of the selected precursor (boron isopropoxide) and varying the temperature of the bubbler where it was placed.

The incorporation of interstitial boron induced a noticeable change in the morphology of the doped-films, as observed by SEM imaging and in the average particle size, more remarkable when depositing the films using APCVD. In that case, the optical band gap, obtained by UV-Vis spectroscopy, applying the Tauc plot method, slightly changed but no visible light absorption/response was found. The photocatalytic performance of B-TiO₂ films under UV, during the degradation

of stearic acid, was enhanced, being much higher and noticeable in the case of the film containing around 1% at. B. Also, reported for the first time in this thesis, the interstitial boron-doped TiO₂ samples presented certain conductivity and electron mobility, proven by multimeter and Hall Effect measurements.

From our theoretical and computational analyses, we show that when forming B_i, the material will be made n-type under *Ti-rich/O-poor* conditions, explaining the n-type conductivity measured. B_i³⁺ is the most preferential dopant state to form. Under *Ti-poor/O-rich* conditions the Fermi level will be trapped ~2 eV above the VBM, indicating that electrons trapped at this level could be excited by visible light into the CBM thus increasing the visible light activity. Nevertheless, our samples synthesised by APCVD never showed any visible light induced photoactivity.

When using AP-PECVD for the synthesis of boron-doped anatase TiO₂ thin films, the depositions were performed in one step, with no need of annealing or post-treatment to obtain the desired photoactive anatase phase of TiO₂ at low temperature. The PMMA polymeric optical fibres visually kept their mechanical properties after the deposition and did not melt during the synthesis. In this case, boron occupied most probably an interstitial position and even though the different boron-doped films were synthesised using different flow rates of the dopant placed in a separated bubbler (APCVD approach), the concentration of boron within the doped films was found to be very similar between all born-doped samples, showing that by this technique and this specific approach, only films containing ~4% at. of interstitial boron were synthesised. The optical band gap only showed differences in the B-TiO₂ sample synthesised using a boron isopropoxide flow rate of 0.5 slm (sample P3, Chapter 3), which showed the highest rates for photodegradation of MB. All the films presented reasonable rates for photodegradation of methylene blue and all B-TiO₂ samples presented higher rates of photodegradation when compared to the undoped TiO₂ synthesised under the same conditions. When compared to the undoped TiO₂ films, the B-TiO₂ films presented higher rates of photodegradation of the dye. To the best of our knowledge, this was the first time that doped-TiO₂ was synthesized and doped simultaneously at atmospheric pressure by PECVD and that anatase

doped-TiO₂ films were deposited in one-step on a thermo-sensitive polymeric matrix such as PMMA optical fibre.

To overcome the issue of the amount of boron which was incorporated into the thin films, a different approach for AP-PECVD based on regular AACVD was designed and performed.

This time, boron-doped anatase TiO₂ thin films of different concentrations were deposited on different substrates (glass and silicon wafers) by one-step AA-PECVD. The content of boron was modified in solutions from 3-6 mol. % (triethyl borate in toluene). XRD and Raman studies showed that anatase was obtained in the undoped and all boron-doped TiO₂ samples. XPS and D-SIMS analyses showed that boron was incorporated within TiO₂ as mostly interstitial.

All samples presented different concentrations of boron within the films. The incorporation of interstitial boron induced a noticeable change in the morphology of the doped-films, seen by SEM and differences in the average particle size.

In this case, the optical band gap, obtained by Tauc plot method, showed major changes in the boron-doped TiO₂ samples when compared to the undoped TiO₂ film. A shift to a higher wavelength value was observed, which in the case of sample B-TiO₂ (5 mol.%) was close to 400 nm (\approx 350 nm). In the case of this sample, visible light absorption/response was found (see **Chapter 4**). The photocatalytic performance of all B-TiO₂ films under UV light (365 nm), during the degradation of stearic acid, was enhanced, being much higher and noticeable in the case of sample B-TiO₂ (6 mol.%), which contains around 1.35% at. B.

As a personal interpretation of all the data collected after analysis, after all the depositions performed, the time invested on each of them and my own opinion, a table, summarising and rating the suitability of each technique, APCVD, AP-PECVD and AA-PECVD, in terms of what technique to use, depending on what is the final aim for the coating is presented (**Table 5.1**). The table contains several selected properties which have been selected and are explained explain below:

- (1) *Robustness and attachment to the substrate*: based on visual observations of the samples and the cross-section SEM images which can be seen in all chapters.
- (2) *Smooth surface*: based on the top-view SEM images taken in all the cases.

- (3) *Deposition on thermos-sensitive substrates*: based on the working temperature required for each technique to operate and get a functional coating, *i. e.*, APCVD needs to be performed between 450-500 °C to obtain the desired anatase with functional properties.
- (4) *Reproducibility of the process*: here, I based my rating on my personal experience, *i. e.*, how many samples, synthesised under the same conditions, present similar properties and how many times the synthesis can be performed producing similar samples.
- (5) *Crystallinity of the resulting films*: based on XRD and Raman analysis of the samples.
- (6) *Selectivity of the process*: based on the idea of obtaining interstitial boron and at different concentrations within the different B-TiO₂ films.
- (7) *Suitable for reel-to-reel process*: here, a few facts have been taken in account; the need of a vacuum system; the possible size of the sample that can be coated; the availability of precursors and the possibility of building and up-scale a bigger reactor, based on the prototypes used in this thesis.
- (8) *Modification of the optical band gap*: based on the UVV-Visible spectra recorded and the Tauc plot calculations. Also, theoretical calculations supported the idea of BG modification in certain cases.
- (9) *Photocatalysis performance under UVA and visible light*: based on all the photocatalytic tests run.
- (10) *Conductivity*: based on the test by multimeter and hall effect measurements when applicable

Table 5.1. Personal rating of selected physical and functional properties, as well as the suitability of synthesis of interstitial boron-doped TiO₂ by APCVD, AP-PECVD and AA-PECVD.

Synthesis of interstitial B-TiO ₂ films			
Physical & Functional properties of the resulting films	APCVD	AP-PECVD	AA-PECVD
Robustness & attachment to the substrate	↑↑↑↑	↑↑	↑↑
Smooth surface	↑↑↑↑	↑	↑
Deposition on thermo-sensitive substrates	↓	↑↑↑	↑↑↑
Reproducibility of the process	↑↑↑↑	↑	↑↑
Crystallinity of the resulting films	↑↑↑↑	↑	↑
Selectivity of the process	↑↑↑↑	↑	↑↑
Suitable for a reel-to-reel process	↑↑↑↑	↑↑↑	↑↑↑
Modification of the BG-Changes in the optical properties	↑	↑	↑↑↑
Photocatalysis performance under UVA light	↑↑↑↑	↑↑	↑↑
Photocatalysis performance under visible light	↓	↓	↑↑
Conductivity	↑↑	↓	↓

5.2 Future work: promising results

I believe this thesis is of considerable interest to the Materials Research community. Anatase TiO_2 and in boarder perspective crystalline transition-metal oxides thin films are continuously drawing considerable interest, particularly considering their applications in photoelectrochemical cells for solar energy harvesting devices and water splitting. Our novel AP-PECVD/AA-PECVD processes are inherently suitable to other crystalline transition-metal oxides and could reach other functionalities, such as electrical conductivity or electrochromic (WO_3) or thermochromic coatings (VO_2). The ability to deposit crystalline transition-metal oxides on temperature-sensitive substrates (e.g. textiles, polymers) represents new opportunities in the fields of energy and sensing materials.

The suggested next step would be doping of TiO_2 with transition metals such as W, by AA-PECVD, so TCOs could be synthesised and deposited on POFs, creating a new generation of flexible TCOs that could have many applications in the industry.

In fact, we have been recently trying to synthesise W- TiO_2 and the results are promising. First trials of W- TiO_2 thin films by a combination of AP-PECVD and AA-PECVD approaches, showed the presence of solely anatase and first functional tests showed both, conductivity and photocatalytic properties enhanced when compared to undoped TiO_2 synthesised under the same conditions (see **Figure 5.1**).

The major Raman scattering band of anatase (E_g) was found at 144.8 cm^{-1} in undoped TiO_2 films, which can be clearly observed in **Figure 5.1a and b**. In **Figure 5.1b**, it can be observed that the scattering E_g band was shifted to higher wavenumbers when TiO_2 was doped by tungsten. The shifting was proportional to the increase of concentration (mol. %) of W in solution, in other words, a noticeable linear inter-relationship between the tungsten doping level and the degree of blue shifting in the main Raman active E_g vibrational mode was found. The shifting can be explained as a direct effect of expansion of the unit cell of anatase when doping.

Also, we believe that co-doping of interstitial boron-doped TiO_2 with other elements, will offer new opportunities for the synthesis of new stable multifunctional layers.

For instance, the combination of W and B could lead to a stable and multifunctional coating which thanks to our AP-PECVD/AA-PECVD approach could be easily deposited on thermos-sensitive substrates.

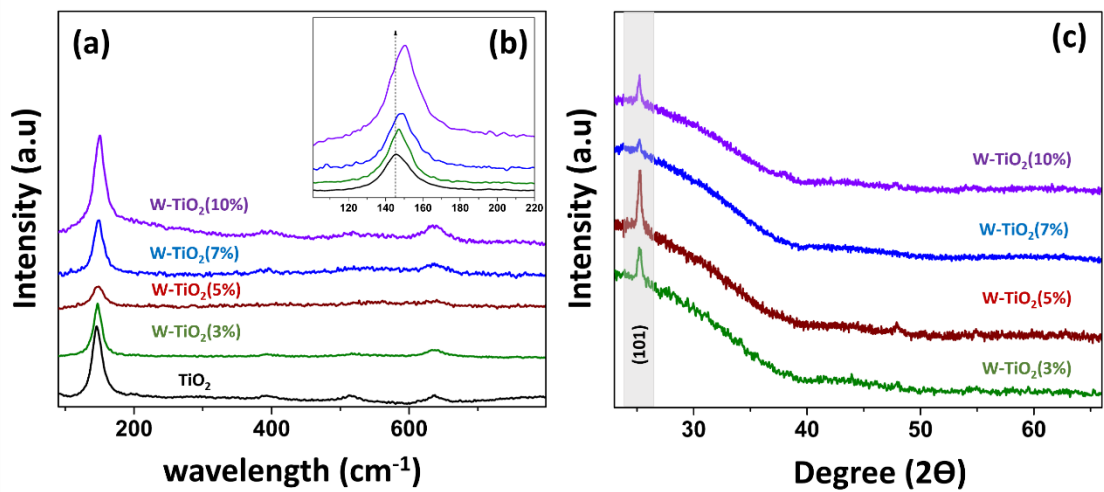


Figure 5.1. (a) Comparison of Raman spectra: W-TiO₂ films samples of different concentrations vs undoped TiO₂ synthesised and deposited on POFs under the same conditions; (b) inset of the Eg band shifting in Raman; (c) XRD patterns of W-TiO₂ thin films deposited on glass.

References

- (1) Fujishima, A.; Rao, T. N.; Tryk, D. A. Titanium Dioxide Photocatalysis. *J. Photochem. Photobiol. C Photochem. Rev.* **2000**, 1, 1–21.
- (2) Fujishima, A.; Zhang, X.; Tryk, D. A. TiO₂ Photocatalysis and Related Surface Phenomena. *Surface Science Reports.* 2008, 515–582.
- (3) Velten, D.; Biehl, V.; Aubertin, F.; Valeske, B.; Possart, W.; Breme, J. Preparation of TiO₂ Layers on Cp-Ti and Ti₆Al₄V by Thermal and Anodic Oxidation and by Sol-Gel Coating Techniques and Their Characterization. *J. Biomed. Mater. Res.* **2002**, 59, 18–28.
- (4) Burda, C.; Chen, X.; Narayanan, R.; El-Sayed, M. A. Chemistry and Properties of Nanocrystals of Different Shapes. *Chemical Reviews.* 2005, 1025–1102.
- (5) Kafizas, A.; Parkin, I. P. Combinatorial Atmospheric Pressure Chemical Vapor Deposition (cAPCVD): A Route to Functional Property Optimization. *J. Am. Chem. Soc.* **2011**, 133, 20458–20467.
- (6) Kafizas, A.; Parkin, I. Inorganic Thin-Film Combinatorial Studies for Rapidly Optimising Functional Properties. *Chem. Soc. Rev.* **2012**, 41, 738-781.
- (7) Mills, A.; Le Hunte, S. An Overview of Semiconductor Photocatalysis. *J. Photochem. Photobiol. A Chem.* **1997**, 108, 1–35.
- (8) Ni, M.; Leung, M. K. H.; Leung, D. Y. C.; Sumathy, K. A Review and Recent Developments in Photocatalytic Water-Splitting Using TiO₂ for Hydrogen Production. *Renew. Sustain. Energy Rev.* **2007**, 11, 401–425.
- (9) Savage, N.; Chwieroth, B.; Ginwalla, A.; Patton, B. R.; Akbar, S. A.; Dutta, P. K. Composite N-P Semiconducting Titanium Oxides as Gas Sensors. *Sensors Actuators, B Chem.* **2001**, 79, 17–27.
- (10) Liu, B.; Aydil, E. S. Growth of Oriented Single-Crystalline Rutile TiO₂ Nanorods on Transparent Conducting Substrates for Dye-Sensitized Solar Cells. *J. Am. Chem. Soc.* **2009**, 131, 3985–3990.
- (11) Zaleska, A. Doped-TiO₂: A Review. *Recent Patents Eng.* **2008**, 1, 157–164.
- (12) Hashimoto, K.; Irie, H.; Fujishima, A. TiO₂ Photocatalysis: A Historical Overview and Future Prospects. *Jpn. J. Appl. Phys.* **2005**, 44, 8269–8285.
- (13) Zhang, H.; Chen, G.; Bahnemann, D. W. Photoelectrocatalytic Materials for Environmental Applications. *J. Mater. Chem.* **2009**, 19, 5089.
- (14) Page, K.; Palgrave, R. G.; Parkin, I. P.; Wilson, M.; Savin, S. L. P.;

- Chadwick, A. V. Titania and Silver–titania Composite Films on Glass—potent Antimicrobial Coatings. *R. Soc. Chem.* **2006**, 17, 95–104.
- (15) Hajkova, P.; Spatenka, P.; Horsky, J.; Horska, I.; Kolouch, A. Photocatalytic Effect of TiO₂ Films on Viruses and Bacteria. *Plasma Process. Polym.* **2007**, 4, 397–401.
- (16) Kubota, Y.; Shuin, T.; Kawasaki, C.; Hosaka, M.; Kitamura, H.; Cai, R.; Sakai, H.; Hashimoto, K.; Fujishima, A. Photokilling of T-24 Human Bladder Cancer Cells with Titanium Dioxide. *Br. J. Cancer*, **1994**, 70, 1107–1111.
- (17) Schneider, J.; Matsuoka, M.; Takeuchi, M.; Zhang, J.; Horiuchi, Y.; Anpo, M.; Bahnemann, D. W. Understanding TiO₂ Photocatalysis : Mechanisms and Materials. *Chem. Rev.* **2014**, 114, 9919–9986.
- (18) Li, H.; Guan, L.-X.; Feng, J.-J.; Li, F.; Yao, M.-M. TiO₂ -Based Composite Films For The Photodegradation of Oxytetracycline. *Surf. Rev. Lett.* **2015**, 22, 1550024.
- (19) Kafizas, A.; Kellici, S.; Darr, J. A.; Parkin, I. P. Titanium Dioxide and Composite Metal/metal Oxide Titania Thin Films on Glass: A Comparative Study of Photocatalytic Activity. *J. Photochem. Photobiol. A Chem.* **2009**, 204, 183–190.
- (20) Kamat, P. V. Photophysical, Photochemical and Photocatalytic Aspects of Metal Nanoparticles. *J. Phys. Chem. B*, **2002**, 106, 7729–7744.
- (21) Palgrave, R. G.; Parkin, I. P. Aerosol Assisted Chemical Vapor Deposition Using Nanoparticle Precursors: A Route to Nanocomposite Thin Films. *J. Am. Chem. Soc.* **2006**, 128, 1587–1597.
- (22) Rajh, T.; Nedeljkovic, J. M.; Chen, L. X.; Poluektov, O.; Thurnauer, M. C. Improving Optical and Charge Separation Properties of Nanocrystalline TiO₂ by Surface Modification with Vitamin C. *J. Phys. Chem. B* **1999**, 103, 3515–3519.
- (23) Zhao, D.; Chen, C.; Wang, Y.; Ji, H.; Ma, W.; Zang, L.; Zhao, J. Surface Modification of TiO₂ by Phosphate: Effect on Photocatalytic Activity and Mechanism Implication. *J. Phys. Chem. C*, **2008**, 112, 5993–6001.
- (24) Thurnauer, M. C.; Martin, A. M. Y.; Kemme, P. A. Surface Modification of TiO₂ Nanoparticles For Photochemical Reduction of Nitrobenzene. **2000**, 34, 4797–4803.
- (25) Finazzi, E.; Valentin, C. Di; Pacchioni, G. Boron-Doped Anatase TiO₂: Pure and Hybrid DFT Calculations. *J. Phys. Chem. C*, **2009**, 113, 220–228.
- (26) Asahi, R.; Morikawa, T.; Irie, H.; Ohwaki, T. Nitrogen-Doped Titanium Dioxide as Visible-Light-Sensitive Photocatalyst: Designs, Developments, and Prospects. *Chem. Rev.* **2014**, 114, 9824–9852.

- (27) Zhang, X.; Liu, F.; Huang, Q. L.; Zhou, G.; Wang, Z. S. Dye-Sensitized W-Doped TiO₂ Solar Cells with a Tunable Conduction Band and Suppressed Charge Recombination. *J. Phys. Chem. C* **2011**, 115, 12665–12671.
- (28) Wang, Y.; Xue, X.; Yang, H. Preparation and Characterization of Carbon Or/and Boron-Doped Titania Nano-Materials with Antibacterial Activity. *Ceram. Int.* **2014**, 40, 12533–12537.
- (29) Sathasivam, S.; Bhachu, D. S.; Lu, Y.; Chadwick, N.; Althabaiti, S. A.; Alyoubi, A. O.; Basahel, S. N.; Carmalt, C. J.; Parkin, I. P. Tungsten Doped TiO₂ with Enhanced Photocatalytic and Optoelectrical Properties via Aerosol Assisted Chemical Vapor Deposition. *Sci. Rep.* **2015**, 5, 10952.
- (30) Tian, Y.; Tatsuma, T. Mechanisms and Applications of Plasmon-Induced Charge Separation at TiO₂ Films Loaded with Gold Nanoparticles. *J. Am. Chem. Soc.* **2005**, 127, 7632–7637.
- (31) Sangpour, P.; Hashemi, F.; Moshfegh, A. Z. Photoenhanced Degradation of Methylene Blue on Cosputtered M:TiO₂ (M = Au, Ag, Cu) Nanocomposite Systems: A Comparative Study. *J. Phys. Chem. C*, **2010**, 114, 13955–13961.
- (32) Anpo, M. Utilization of TiO₂ Photocatalysts in Green Chemistry. *Pure and Appl. Chem.*, **2000**, 72, 1265–1270.
- (33) Fuerte, A.; Hernández-Alonso, M. D.; Maira, A. J.; Martínez-Arias, A.; Fernández-García, M.; Conesa, J. C.; Soria, J. Visible Light-Activated Nanosized Doped-TiO₂ Photocatalysts. *Chem. Commun.* **2001**, 24, 2718–2719.
- (34) Yamashita, H.; Harada, M.; Misaka, J.; Takeuchi, M.; Ichihashi, Y.; Goto, F.; Ishida, M.; Sasaki, T.; Anpo, M. Application of Ion Beam Techniques for Preparation of Metal Ion-Implanted TiO₂ thin Film Photocatalyst Available under Visible Light Irradiation: Metal Ion-Implantation and Ionized Cluster Beam Method. *J. Synchrotron Radiat.* **2001**, 8, 569–571.
- (35) Ihara, T.; Miyoshi, M.; Ando, M.; Sugihara, S.; Iriyama, Y. Preparation of a Visible-Light-Active TiO₂ Photocatalyst by RF Plasma Treatment. *J. Mater. Sci.* **2001**, 36, 4201–4207.
- (36) Takeuchi, K.; Nakamura, I.; Matsumoto, O.; Sugihara, S.; Ando, M.; Ihara, T. Preparation of Visible-Light-Responsive Titanium Oxide Photocatalysts by Plasma Treatment. *Chem. Lett.* **2000**, 29, 1354–1355.
- (37) Korösi, L.; Oszkó, A.; Galbács, G.; Richardt, A.; Zöllmer, V.; Dékány, I. Structural Properties and Photocatalytic Behaviour of Phosphate-Modified Nanocrystalline Titania Films. *Appl. Catal. B Environ.* **2007**, 77, 175–183.
- (38) Wawrzyniak, B.; Morawski, A. W.; Tryba, B. Preparation of TiO₂-Nitrogen-Doped Photocatalyst Active under Visible Light. *Int. J. Photoenergy* **2006**, Article ID 68248, 8 pages.

- (39) Quesada-Cabrera, R.; Sotelo-Vazquez, C.; Quesada-Gonzalez, M.; Melian, E. P.; Chadwick, N.; Parkin, I. P. On the Apparent Visible-Light and Enhanced UV-Light Photocatalytic Activity of Nitrogen-Doped TiO₂ Thin Films. *J. Photochem. Photobiol. A Chem.* **2017**, 333, 49–55.
- (40) Gombac, V.; De Rogatis, L.; Gasparotto, A.; Vicario, G.; Montini, T.; Barreca, D.; Balducci, G.; Fornasiero, P.; Tondello, E.; Graziani, M. TiO₂ Nanopowders Doped with Boron and Nitrogen for Photocatalytic Applications. *Chem. Phys.* **2007**, 339, 111–123.
- (41) Chen, D.; Yang, D.; Wang, Q.; Jiang, Z. Effects of Boron Doping on Photocatalytic Activity and Microstructure of Titanium Dioxide Nanoparticles. *Ind. Eng. Chem. Res.* **2006**, 4110–4116.
- (42) Yang, K.; Dai, Y.; Huang, B. Origin of the Photoactivity in Boron-Doped Anatase and Rutile TiO₂ Calculated from First Principles. *Phys. Rev. B - Condens. Matter Mater. Phys.* **2007**, 76, 1–6.
- (43) Geng, H.; Yin, S.; Yang, X.; Shuai, Z.; Liu, B. Geometric and Electronic Structures of the Boron-Doped Photocatalyst TiO₂. *J. Phys. Condens. Matter* **2006**, 18, 87–96.
- (44) Xu, T.-H.; Song, C.-L.; Liu, Y.; Han, G.-R. Band Structures of TiO₂ Doped with N, C and B. *J. Zhejiang Univ. Sci. B* **2006**, 7, 299–303.
- (45) Patel, N.; Dashora, A.; Jaiswal, R.; Fernandes, R.; Yadav, M.; Kothari, D. C.; Ahuja, B. L.; Miotello, a. Experimental and Theoretical Investigations on the Activity and Stability of Substitutional and Interstitial Boron in TiO₂ Photocatalyst. *J. Phys. Chem. C* **2015**, 119, 18581–18590.
- (46) Carlsson, J. Chemical Vapor Deposition. *Handb. Depos. Technol. Film. Coatings* **2010**, 400–459.
- (47) Guillot, J.; Lecoq, E.; Duday, D.; Puhakka, E.; Riihimäki, M.; Keiski, R.; Chemin, J.-B.; Choquet, P. Combining a Molecular Modelling Approach with Direct Current and High Power Impulse Magnetron Sputtering to Develop New TiO₂ Thin Films for Antifouling Applications. *Appl. Surf. Sci.* **2015**, 333, 186–193.
- (48) Carmichael, P.; Hazafy, D.; Bhachu, D. S.; Mills, A.; Darr, J. A.; Parkin, I. P. Atmospheric Pressure Chemical Vapour Deposition of Boron Doped Titanium Dioxide for Photocatalytic Water Reduction and Oxidation. *Phys. Chem. Chem. Phys.* **2013**, 15, 16788–16794.
- (49) Masahashi, N.; Oku, M. Superhydrophilicity and XPS Study of Boron-Doped TiO₂. *Appl. Surf. Sci.* **2008**, 254, 7056–7060.
- (50) Yu, J.; Zhao, X.; Zhao, Q. Effect of Surface Structure on Photocatalytic Activity of TiO₂ Thin Films Prepared by Sol-Gel Method. *Thin Solid Films* **2000**, 379, 7–14.
- (51) Choy, K. Chemical Vapour Deposition of Coatings. *Prog. Mater. Sci.*

- 2003**, 48, 57–170.
- (52) Tendero, C.; Tixier, C.; Tristant, P.; Desmaison, J.; Leprince, P. Atmospheric Pressure Plasmas: A Review. *Spectrochim. Acta - Part B At. Spectrosc.* **2006**, 61, 2–30.
- (53) Chabert, P.; Braithwaite, N. *Physics of Radio-Frequency Plasmas*; 2011; Vol. 9780521763.
- (54) Kabouzi, Y.; Calzada, M. D.; Moisan, M.; Tran, K. C.; Trassy, C. Radial Contraction of Microwave-Sustained Plasma Columns at Atmospheric Pressure. *J. Appl. Phys.* **2002**, 91, 1008–1019.
- (55) Woskov, P. P.; Hadidi, K. Large Electrodeless Plasmas at Atmospheric Pressure Sustained by a Microwave Waveguide. *IEEE Trans. Plasma Sci.* **2002**, 30, 156–157.
- (56) Bilgic, A. M.; Engel, U.; Vogest, E.; Kückelheim, M.; Broekaert, J. A. C. New Low-Power Microwave Plasma Source Using Microstrip Technology for Atomic Emission Spectrometry. *Plasma Sources Sci. Technol.* **2000**, 9, 1–4.
- (57) Skoog, D. A.; West, D. M.; Holler, F. J.; Couch, S. R. Fundamentos de Química Analítica. *Spectrochim. Acta Part B* **2003**, 58, 1585–1596.
- (58) O'Neill, S.; Parkin, I. P.; Clark, R. J. H.; Mills, A.; Elliott, N. Photocatalytically Active γ - WO_3 Films from the Atmospheric Pressure CVD of WOCl_4 with Ethyl Acetate or Ethanol. *Chem. Vap. Depos.* **2004**, 10, 136–141.
- (59) Bhachu, D. S.; Sathasivam, S.; Sankar, G.; Scanlon, D. O.; Cibir, G.; Carmalt, C. J.; Parkin, I. P.; Watson, G. W.; Bawaked, S. M.; Obaid, A. Y.; Al-Thabaiti, S.; Basahel, S. N. Solution Processing Route to Multifunctional Titania Thin Films: Highly Conductive and Photocatalytically Active Nb:TiO₂. *Adv. Funct. Mater.* **2014**, 24, 5075–5085.
- (60) Tseng, T. K.; Lin, Y. S.; Chen, Y. J.; Chu, H. A Review of Photocatalysts Prepared by Sol-Gel Method for VOCs Removal. *Int. J. Mol. Sci.* **2010**, 11, 2336–2361.
- (61) Quesada-Cabrera, R.; Sotelo-Vázquez, C.; Darr, J. A.; Parkin, I. P. Critical Influence of Surface Nitrogen Species on the Activity of N-Doped TiO₂ Thin films during Photodegradation of Stearic Acid under UV Light Irradiation. *Appl. Catal. B Environ.* **2014**, 161, 582–588.
- (62) Emeline, A. V.; Kuznetsov, V. N.; Rybchuk, V. K.; Serpone, N. Visible-Light-Active Titania Photocatalysts: The Case of N-Doped TiO₂— Properties and Some Fundamental Issues. *Int. J. Photoenergy* **2008**, Article ID 258394, 19 pages.
- (63) Zaleska, A.; Grabowska, E.; Sobczak, J. W.; Gazda, M.; Hupka, J. Photocatalytic Activity of Boron-Modified TiO₂ under Visible Light: The

- Effect of Boron Content, Calcination Temperature and TiO₂ Matrix. *Appl. Catal. B Environ.* **2009**, 89, 469–475.
- (64) Quesada-González, M.; Boscher, N. D.; Carmalt, C. J.; Parkin, I. P. Interstitial Boron-Doped TiO₂ Thin Films: The Significant Effect of Boron on TiO₂ Coatings Grown by Atmospheric Pressure Chemical Vapor Deposition. *ACS Appl. Mater. Interfaces* **2016**, 8, 25024–25029.
- (65) Toby, B. H.; EXPGUI, a Graphical User Interface for GSAS. *J. Appl. Crystallogr.* **2001**, 34, 210–213.
- (66) Kresse, G.; Hafner, J. Ab Initio Molecular Dynamics for Liquid Metals. *Phys. Rev. B* **1993**, 47, 558–561.
- (67) Kresse, G.; Hafner, J. Ab-Initio Molecular-Dynamics Simulation of the Liquid-Metal Amorphous-Semiconductor Transition in Germanium. *Phys. Rev. B*, **1994**, 49, 14251–14269.
- (68) Kresse, G.; Furthmüller, J. Efficiency of Ab-Initio Total Energy Calculations for Metals and Semiconductors Using a Plane-Wave Basis Set. *Comput. Mater. Sci.* **1996**, 6, 15–50.
- (69) Kresse, G.; Furthmu, J.; J., F.; Kresse, G.; Furthmu, J. Efficient Iterative Schemes for Ab Initio Total-Energy Calculations Using a Plane-Wave Basis Set. *Phys. Rev. B Condens. Matter Mater. Phys.* **1996**, 54, 11169.
- (70) Blochl, P. E. Projector Augmented-Wave Method. *Phys. Rev. B*, **1994**, 50, 17953–17979.
- (71) Paier, J.; Marsman, M.; Hummer, K.; Kresse, G. Screened Hybrid Density Functionals Applied to Solids Screened Hybrid Density Functionals Applied to Solids. **2006**, 124, 154709.
- (72) Heyd, J.; Scuseria, G. E.; Ernzerhof, M. Hybrid Functionals Based on a Screened Coulomb Potential. *J. Chem. Phys.* **2003**, 118, 8207–8215.
- (73) Sathasivam, S.; Williamson, B. A. D.; Kafizas, A.; Althabaiti, S. A.; Obaid, A. Y.; Basahel, S. N.; Scanlon, D. O.; Carmalt, C. J.; Parkin, I. P. Computational and Experimental Study of Ta₂O₅ Thin Films. *J. Phys. Chem. C* **2017**, 121, 202–210.
- (74) Marchand, P.; Sathasivam, S.; Williamson, B. A. D.; Pugh, D.; Bawaked, S. M.; Basahel, S. N.; Obaid, A. Y.; Scanlon, D. O.; Parkin, I. P.; Carmalt, C. J. A Single-Source Precursor Approach to Solution Processed Indium Arsenide Thin Films. *J. Mater. Chem. C*, **2016**, 4, 6761-6768.
- (75) Williamson, B. A.; Buckeridge, J.; Brown, J.; Ansbro, S.; Palgrave, R. G.; Scanlon, D. O. Engineering Valence Band Dispersion for High Mobility P-Type Semiconductors. *Chem. Mater.* **2016**, 29, 2402–2413.
- (76) Oba, F.; Togo, A.; Tanaka, I.; Paier, J.; Kresse, G. Defect Energetics in ZnO: A Hybrid Hartree-Fock Density Functional Study. *Phys. Rev. B* -

- Condens. Matter Mater. Phys.* **2008**, *77*, 3–8.
- (77) Chen, H.; Dawson, J. A. Nature of Nitrogen-Doped Anatase TiO₂ and the Origin of Its Visible-Light Activity. *J. Phys. Chem. C*, **2015**, *119*, 15890–15895.
- (78) Kafizas, A.; Noor, N.; Carmichael, P.; Scanlon, D. O.; Carmalt, C. J.; Parkin, I. P. Combinatorial Atmospheric Pressure Chemical Vapor Deposition of F:TiO₂; The Relationship between Photocatalysis and Transparent Conducting Oxide Properties. *Adv. Funct. Mater.* **2014**, *24*, 1758–1771.
- (79) Burbano, M.; Scanlon, D. O.; Watson, G. W. Sources of Conductivity and Doping Limits in CdO from Hybrid Density Functional Theory. *J. Am. Chem. Soc.* **2011**, *133*, 15065–15072.
- (80) Rajpalke, M. K.; Linhart, W. M.; Birkett, M.; Yu, K. M.; Scanlon, D. O.; Buckeridge, J.; Jones, T. S.; Ashwin, M. J.; Veal, T. D. Growth and Properties of GaSbBi Alloys. *Appl. Phys. Lett.* **2013**, *103*, 0–4.
- (81) Ganose, A. M.; Savory, C. N.; Scanlon, D. O. (CH₃NH₃)₂Pb(SCN)₂I₂: A More Stable Structural Motif for Hybrid Halide Photovoltaics? *J. Phys. Chem. Lett.* **2015**, *6*, 4594–4598.
- (82) Scanlon, D. O.; Walsh, A. Bandgap Engineering of ZnSnP₂ for High-Efficiency Solar Cells. *Appl. Phys. Lett.* **2012**, *100*, 4–7.
- (83) Walsh, A.; Kehoe, A. B.; Temple, D. J.; Watson, G. W.; Scanlon, D. O. PbO₂: From Semi-Metal to Transparent Conducting Oxide by Defect Chemistry Control. *Chem. Commun.*, **2013**, *49*, 448–450.
- (84) Buckeridge, J.; Scanlon, D. O.; Walsh, A.; Catlow, C. R. A. Automated Procedure to Determine the Thermodynamic Stability of a Material and the Range of Chemical Potentials Necessary for Its Formation Relative to Competing Phases and Compounds. *Comput. Phys. Commun.* **2014**, *185*, 330–338.
- (85) Çelik, V.; Mete, E. Range-Separated Hybrid Exchange-Correlation Functional Analyses of Anatase TiO₂ Doped with W, N, S, W/N, or W/S. *Phys. Rev. B - Condens. Matter Mater. Phys.* **2012**, *86*, 1–9.
- (86) Scanlon, D. O.; Dunnill, C. W.; Buckeridge, J.; Shevlin, S. A.; Logsdail, A. J.; Woodley, S. M.; Catlow, C. R. A.; Powell, M. J.; Palgrave, R. G.; Parkin, I. P.; Watson, G. W.; Keal, T. W.; Sherwood, P.; Walsh, A.; Sokol, A. A. Band Alignment of Rutile and Anatase TiO₂. *Nat. Mater.* **2013**, *12*, 798–801.
- (87) Huy, H. A.; Aradi, B.; Frauenheim, T.; Deák, P. Calculation of Carrier-Concentration-Dependent Effective Mass in Nb-Doped Anatase Crystals of TiO₂. *Phys. Rev. B - Condens. Matter Mater. Phys.* **2011**, *83*, 155201.
- (88) Janotti, A.; Varley, J. B.; Rinke, P.; Umezawa, N.; Kresse, G.; Van de

- Walle, C. G. Hybrid Functional Studies of the Oxygen Vacancy in TiO₂. *Phys. Rev. B* **2010**, 81, 85212.
- (89) Matsubara, M.; Saniz, R.; Partoens, B.; Lamoen, D. Doping Anatase TiO₂ with Group V-B and VI-B Transition Metal Atoms: A Hybrid Functional First-Principles Study. *Phys. Chem. Chem. Phys.* **2017**, 19, 1945–1952.
- (90) Boonchun, A.; Reunchan, P.; Umezawa, N. Energetics of Native Defects in Anatase TiO₂: A Hybrid Density Functional Study. *Phys. Chem. Chem. Phys.* **2016**, 4, 1166–1169.
- (91) Hine, N. D. M.; Frensch, K.; Foulkes, W. M. C.; Finnis, M. W. Supercell Size Scaling of Density Functional Theory Formation Energies of Charged Defects. *Phys. Rev. B - Condens. Matter Mater. Phys.* **2009**, 79, 1–13.
- (92) Nieminen, R. M. Issues in First-Principles Calculations for Defects in Semiconductors and Oxides. *Model. Simul. Mater. Sci. Eng.* **2009**, 17, 84001.
- (93) Murphy, S. T.; Hine, N. D. M.; Kensington, S. Defect Formation Energies. **2013**, 87, 094111.
- (94) Lany, S.; Zunger, A. Assessment of Correction Methods for the Band-Gap Problem and for Finite-Size Effects in Supercell Defect Calculations: Case Studies for ZnO and GaAs. *Phys. Rev. B - Condens. Matter Mater. Phys.* **2008**, 78, 17–20.
- (95) Freysoldt, C.; Neugebauer, J.; Van De Walle, C. G. Fully Ab Initio Finite-Size Corrections for Charged-Defect Supercell Calculations. *Phys. Rev. Lett.* **2009**, 102, 1–4.
- (96) Chase, J. M. . No Title. *J. Phys. Chem. Ref. Data Monogr. No. 9 NIST. JANAF Thermochem. Tables* **1998**, 9, 1.
- (97) Burdett, J. K.; Hughbanks, T.; Miller, G. J.; Richardson, J. W.; Smith, J. V. Structural-Electronic Relationships in Inorganic Solids: Powder Neutron Diffraction Studies of the Rutile and Anatase Polymorphs of Titanium Dioxide at 15 and 295 K. *J. Am. Chem. Soc.* **1987**, 109, 3639–3646.
- (98) Kafizas, A.; Carmalt, C. J.; Parkin, I. P. CVD and Precursor Chemistry of Transition Metal Nitrides. *Coord. Chem. Rev.* **2013**, 257, 2073–2119.
- (99) Ohsaka, T.; Izumi, F.; Fujiki, Y. Raman Spectrum of Anatase, TiO₂. *J. Raman Spectrosc.* **1978**, 7, 321–324.
- (100) Kafizas, A.; Noor, N.; Carmalt, C. J.; Parkin, I. P. TiO₂-Based Transparent Conducting Oxides; the Search for Optimum Electrical Conductivity Using a Combinatorial Approach. *J. Mater. Chem. C* **2013**, 1, 6335.
- (101) Quesada-González, M.; Baba, K.; Sotelo-Vázquez, C.; Choquet, P.; Carmalt, C. J.; Parkin, I. P.; Boscher, N. D. Interstitial Boron-Doped Anatase TiO₂ Thin films on Optical Fibres: Atmospheric Pressure-Plasma

- Enhanced Chemical Vapour Deposition as the Key for Functional Oxide Coatings on Temperature-Sensitive Substrates. *J. Mater. Chem. A*, **2017**, 5, 10836-10842.
- (102) Sabyrov, K.; Burrows, N. D.; Penn, R. L.; Merche, D.; Vandencastele, N.; Reniers, F.; Yokoyama, T.; Kogoma, M.; Yokoyama, T.; Kogoma, M.; Sawada, Y.; Ogawa, S.; Kogoma, M.; Kogoma, M.; Okazaki, S.; Di, L.; Li, X.; Shi, C.; Xu, Y.; Zhao, D.; Bruggeman, P.; Brandenburg, R.; Massines, F.; Sarra-bournet, C.; Fanelli, F.; Gherardi, N.; Evans, P.; Pemble, M. E.; Sheel, D. W.; Chen, C.; Bai, H.; Chang, S.; Chang, C.; Den, W.; Tio, U.; Pressure, A. Size-Dependent Anatase to Rutile Phase Transformation and Particle.pdf. *Chem. Mater.* **2013**, 25, 1408–1415.
- (103) Pore, V.; Ritala, M.; Leskelä, M.; Areva, S.; Järn, M.; Järnström, J. H₂S Modified Atomic Layer Deposition Process for Photocatalytic TiO₂ Thin Films. *J. Mater. Chem.* **2007**, 17, 1361.
- (104) Richter, H.; Wang, Z. P.; Ley, L. The One Phonon Raman Spectrum in Microcrystalline Silicon. *Solid State Commun.* **1981**, 39, 625–629.
- (105) Evans, P.; Pemble, M. E.; Sheel, D. W. Precursor-Directed Control of Crystalline Type in Atmospheric Pressure CVD Growth of TiO₂ on Stainless Steel. *Chem. Mater.* **2006**, 18, 5750–5755.
- (106) O'Neill, S. A.; Parkin, I. P.; Clark, R. J. H.; Mills, A.; Elliott, N. Atmospheric Pressure Chemical Vapour Deposition of Titanium Dioxide Coatings on Glass. *J. Mater. Chem.* **2002**, 13, 56–60.
- (107) Artiglia, L.; Lazzari, D.; Agnoli, S.; Rizzi, G. A.; Granozzi, G. Searching for the Formation of Ti – B Bonds in B-Doped TiO₂ – Rutile. **2013**, 117, 13163–13172.
- (108) Noor, N.; Chew, C. K. T.; Bhachu, D. S.; Waugh, M. R.; Carmalt, C. J.; Parkin, I. P. Influencing FTO Thin Film Growth with Thin Seeding Layers: A Route to Microstructural Modification. *J. Mater. Chem. C*, **2015**, 3, 9359-93683.
- (109) Sotelo-Vazquez, C.; Noor, N.; Kafizas, A.; Quesada-Cabrera, R.; Scanlon, D. O.; Taylor, A.; Durrant, J. R.; Parkin, I. P. Multifunctional P-Doped TiO₂ Films: A New Approach to Self-Cleaning, Transparent Conducting Oxide Materials. *Chem. Mater.* **2015**, 27, 3234–3242.
- (110) Mills, A.; Wang, J. Simultaneous Monitoring of the Destruction of Stearic Acid and Generation of Carbon Dioxide by Self-Cleaning Semiconductor Photocatalytic Films. *J. Photochem. Photobiol. A Chem.* **2006**, 182, 181–186.
- (111) Buckeridge, J.; Butler, K. T.; Catlow, C. R. A.; Logsdail, A. J.; Scanlon, D. O.; Shevlin, S. A.; Woodley, S. M.; Sokol, A. A.; Walsh, A. Polymorph Engineering of TiO₂: Demonstrating How Absolute Reference Potentials Are Determined by Local Coordination. *Chem. Mater.* **2015**, 27, 3844–

3851.

- (112) Landmann, M.; Rauls, E.; Schmidt, W. G. The Electronic Structure and Optical Response of Rutile, Anatase and Brookite TiO₂. *J. Phys. Condens. Matter*, **2012**, 24, 195503.
- (113) Dou, M.; Persson, C. Comparative Study of Rutile and Anatase SnO₂ and TiO₂: Band-Edge Structures, Dielectric Functions, and Polaron Effects. *J. Appl. Phys.* **2013**, 113, 083703.
- (114) Patrick, C. E.; Giustino, F. GW Quasiparticle Bandgaps of Anatase TiO₂ Starting from DFT + U. *J. physics. Condens. matter* **2012**, 24, 202201.
- (115) Kang, W.; Hybertsen, M. S. Quasiparticle and Optical Properties of Rutile and Anatase TiO₂. *Phys. Rev. B - Condens. Matter Mater. Phys.* **2010**, 82, 1–11.
- (116) Gong, S.; Liu, B.-G. Electronic Structures and Optical Properties of TiO₂: Improved Density-Functional-Theory Investigation. *Chinese Phys. B* **2012**, 21, 57104.
- (117) Chiodo, L.; Salazar, M.; Romero, A. H.; Laricchia, S.; Della Sala, F.; Rubio, A. Structure, Electronic, and Optical Properties of TiO₂ Atomic Clusters: An Ab Initio Study. *J. Chem. Phys.* **2011**, 135, 244704.
- (118) Morgan, B. J.; Watson, G. W. Intrinsic N-Type Defect Formation in TiO₂: A Comparison of Rutile and Anatase from GGA+U Calculations. *J. Phys. Chem. C* **2010**, 114, 2321–2328.
- (119) Mattioli, G.; Alippi, P.; Filippone, F.; Caminiti, R.; Amore Bonapasta, A. Deep versus Shallow Behavior of Intrinsic Defects in Rutile and Anatase TiO₂ Polymorphs. *J. Phys. Chem. C*, **2010**, 114, 21694–21704.
- (120) Deák, P.; Aradi, B.; Frauenheim, T. Polaronic Effects in TiO₂ Calculated by the HSE06 Hybrid Functional: Dopant Passivation by Carrier Self-Trapping. *Phys. Rev. B - Condens. Matter Mater. Phys.* **2011**, 83, 1–7.
- (121) Morgan, B. J.; Watson, G. W. Polaronic Trapping of Electrons and Holes by Native Defects in Anatase TiO₂. *Phys. Rev. B - Condens. Matter Mater. Phys.* **2009**, 80, 2–5.
- (122) Oba, F.; Nishitani, S. R.; Isotani, S.; Adachi, H.; Tanaka, I. Energetics of Native Defects in ZnO. *J. Appl. Phys.* **2001**, 90, 824–828.
- (123) Janotti, A.; Van De Walle, C. G. Native Point Defects in ZnO. *Phys. Rev. B - Condens. Matter Mater. Phys.* **2007**, 76, 1–22.
- (124) Agoston, P.; Albe, K.; Nieminen, R. M.; Puska, M. J. Intrinsic N-Type Behavior in Transparent Conducting Oxides: A Comparative Hybrid-Functional Study of In₂O₃, SnO₂, and ZnO. *Phys. Rev. Lett.* **2009**, 103, 1–4.

- (125) Scanlon, D. O.; Watson, G. W. On the Possibility of P-Type SnO₂. *J. Mater. Chem.* **2012**, *22*, 25236–25245.
- (126) Kılıç, C.; Zunger, A. Origins of Coexistence of Conductivity and Transparency in SnO₂. *Phys. Rev. Lett.* **2002**, *88*, 95501.
- (127) Singh, A. K.; Janotti, A.; Scheffler, M.; Van De Walle, C. G. Sources of Electrical Conductivity in SnO₂. *Phys. Rev. Lett.* **2008**, *101*, 1–4.
- (128) Walsh, A.; Catlow, C. R. A.; Sokol, A. A.; Woodley, S. M. Physical Properties, Intrinsic Defects, and Phase Stability of Indium Sesquioxide. *Chem. Mater.* **2009**, *21*, 4962–4969.
- (129) Ágoston, P.; Albe, K. Formation Entropies of Intrinsic Point Defects in Cubic In₂O₃ from First-Principles Density Functional Theory Calculations. *Phys. Chem. Chem. Phys.* **2009**, *11*, 3226.
- (130) Lany, S.; Zunger, A. Polaronic Hole Localization and Multiple Hole Binding of Acceptors in Oxide Wide-Gap Semiconductors. *Phys. Rev. B - Condens. Matter Mater. Phys.* **2009**, *80*, 1–5.
- (131) Goyal, A.; Gorai, P.; Peng, H.; Lany, S.; Stevanovic, V. A Computational Framework for Automation of Point Defect Calculations. **2016**, *130*, 1–9.
- (132) Scanlon, D. O. Defect Engineering of BaSnO₃ for High-Performance Transparent Conducting Oxide Applications. *Phys. Rev. B - Condens. Matter Mater. Phys.* **2013**, *87*, 1–5.
- (133) Deák, P.; Aradi, B.; Frauenheim, T. Quantitative Theory of the Oxygen Vacancy and Carrier Self-Trapping in Bulk TiO₂. *Phys. Rev. B - Condens. Matter Mater. Phys.* **2012**, *86*, 1–8.
- (134) Deák, P.; Aradi, B.; Frauenheim, T. Oxygen Deficiency in TiO₂: Similarities and Differences between the Ti Self-Interstitial and the O Vacancy in Bulk Rutile and Anatase. *Phys. Rev. B - Condens. Matter Mater. Phys.* **2015**, *92*, 1–7.
- (135) Na-Phattalung, S.; Smith, M. F.; Kim, K.; Du, M. H.; Wei, S. H.; Zhang, S. B.; Limpijumngong, S. First-Principles Study of Native Defects in Anatase TiO₂. *Phys. Rev. B - Condens. Matter Mater. Phys.* **2006**, *73*, 1–6.
- (136) Dixon S. C.; Sanjayan S.; Williamson B. A. D.; Scanlon D. O.; Carmalt C. J.; Parkin I. P. Transparent Conducting N-Type ZnO:Sc- Synthesis, Optoelectronic Properties and Theoretical Insight. *J. Mater. Chem. C*, **2017**, *5*, 7585–7597.
- (137) Zhao, W.; Ma, W.; Chen, C.; Zhao, J.; Shuai, Z. Efficient Degradation of Toxic Organic Pollutants with Ni₂O₃ /TiO₂ - XBx under Visible Irradiation. *J. Am. Chem. Soc.* **2004**, *126*, 4782–4783.
- (138) Li, L.; Meng, F.; Hu, X.; Qiao, L.; Sun, C. Q.; Tian, H.; Zheng, W. TiO₂ Band Restructuring by B and P Dopants. *PLoS One* **2016**, *11*, 152726.

- (139) Nanjo, H.; Hassan, F. M. B.; Venkatachalam, S.; Teshima, N.; Kawasaki, K.; Aizawa, T.; Aida, T.; Ebina, T. Fabrication of Nanostructured Titania on Flexible Substrate by Electrochemical Anodization. *J. Power Sources* **2010**, *195*, 5902–5908.
- (140) Blackman, C.; Carmalt, C. J.; Parkin, I. P.; Neill, S. O.; London, G. S.; Oaj, W. C. H.; Apostolico, L.; Molloy, K. C.; Rushworth, S. Titanium Phosphide Coatings from the Atmospheric Pressure Chemical Vapor Deposition of TiCl_4 and RPH_2 (R) T-Bu , Ph , Cy Hex). *Chem. Mater.* **2002**, *2*, 3167–3173.
- (141) Mariotti, D.; Belmonte, T.; Benedikt, J.; Velusamy, T.; Jain, G.; Švrček, V. Low-Temperature Atmospheric Pressure Plasma Processes for “Green” Third Generation Photovoltaics. *Plasma Process. Polym.* **2016**, *13* (1), 70–90.
- (142) Boscher, N. D.; Olivier, S.; Maurau, R.; Bulou, S.; Sindzingre, T.; Belmonte, T.; Choquet, P. Photocatalytic Anatase Titanium Dioxide Thin Films Deposition by an Atmospheric Pressure Blown Arc Discharge. *Appl. Surf. Sci.* **2014**, *311*, 721–728.
- (143) Liu, P.; Zhang, J.; Turner, J. A.; Tracy, C. E.; Benson, D. K. Lithium-Manganese-Oxide Thin-Film Cathodes Prepared by Plasma-Enhanced Chemical Vapor Deposition. **2005**, *146*, 2001–2005.
- (144) Dong, S.; Watanabe, M.; Dauskardt, R. H. Conductive Transparent $\text{TiN}_x/\text{TiO}_2$ Hybrid Films Deposited on Plastics in Air Using Atmospheric Plasma Processing. *Adv. Funct. Mater.* **2014**, *24*, 3075–3081.
- (145) Grégori, D.; Benchenaa, I.; Chaput, F.; Thérias, S.; Gardette, J.-L.; Léonard, D.; Guillard, C.; Parola, S. Mechanically Stable and Photocatalytically Active $\text{TiO}_2/\text{SiO}_2$ Hybrid Films on Flexible Organic Substrates. *J. Mater. Chem. A*, **2014**, *2*, 20096–20104.
- (146) Mills, A.; Crow, M.; Wang, J.; Parkin, I. P.; Boscher, N. Photocatalytic Oxidation of Deposited Sulfur and Gaseous Sulfur Dioxide by TiO_2 Films. *J. Phys. Chem. C*, **2007**, *111*, 5520–5525.
- (147) Asahi, R.; Mikawa, T.; Ohwaki, T.; Aoki, K.; Taga, Y. Visible Light Photocatalysis in Nitrogen-Doped Titanium Oxides. *Science*, **2001**, *293*, 269–271.
- (148) Baba, K.; Bulou, S.; Choquet, P.; Boscher, N. D. Photocatalytic Anatase TiO_2 Thin Films on Polymer Optical Fibre Using Atmospheric-Pressure Plasma. *ACS Appl. Mater. Interfaces* **2017**, *9* (15), 13733–13741.
- (149) Kubo, M.; Kusdianto, K.; Masuda, H.; Shimada, M. Fabrication of a Metal Oxide Layer on a Multi-Walled Carbon Nanotube Surface by in-Flight Coating Using Gas-Phase Deposition. *Ceram. Int.* **2016**, *42* (7), 9162–9169.
- (150) Ritala, M.; Leskelä, M.; Rauhala, E. Atomic Layer Epitaxy Growth of

- Titanium Dioxide Thin Films from Titanium Ethoxide. *Chem. Mater.* **1994**, 6 (7), 556–561.
- (151) B. Vincent, C. Handbooks of Monochromatic XPS Spectra Volume 1 - The Elements and Native Oxides. *Handb. Elem. Nativ. Oxides* **1999**, 1, 1–87.
- (152) Quesada-González, M.; Baba, K.; Sotelo-Vazquez, C.; Choquet, P.; Carmalt, C. J.; Parkin, I. P.; Boscher, N. D. Interstitial Boron-Doped Anatase TiO₂ Thin-Film on Optical Fibre: Atmospheric Pressure-Plasma Enhanced Chemical Vapour Deposition as the Key for Functional Oxides Coatings on Temperature-Sensitive Substrates. *J. Mater. Chem. A* **2017**, 5, 10836-10842.
- (153) Zhu, X.; Liu, A. E. G.; Guo, A. Y. Study of PMMA Thermal Bonding. *Micro- and Nano. Inf. Stor. and Process. Syst.*, **2007**, 403–407.
- (154) Gopal, N. O.; Lo, H.-H.; Ke, S.-C. Chemical State and Environment of Boron Dopant in B, N-Codoped Anatase TiO₂ Nanoparticles: An Avenue for Probing Diamagnetic Dopants in TiO₂ by Electron Paramagnetic Resonance Spectroscopy. *J. Am. Chem. Soc.* **2008**, 130 (9), 2760–2761.
- (155) Bhachu, D. S.; Sathasivam, S.; Carmalt, C. J.; Parkin, I. P. PbO-Modified TiO₂ Thin Films: A Route to Visible Light Photocatalysts. *Langmuir* **2014**, 30, 624–630.
- (156) Zhu, A. M.; Nie, L. H.; Wu, Q. H.; Zhang, X. L.; Yang, X. F.; Xu, Y.; Shi, C. Crystalline, Uniform-Sized TiO₂ Nanosphere Films by a Novel Plasma CVD Process at Atmospheric Pressure and Room Temperature. *Chem. Vap. Depos.* **2007**, 13 (4), 141–144.
- (157) Sotelo-Vazquez, C.; Quesada-Cabrera, R.; Darr, J. A.; Parkin, I. P. Single-Step Synthesis of Doped TiO₂ Stratified Thin films by Atmospheric-Pressure Chemical Vapour Deposition. *J. Mater. Chem. A* **2014**, 2 (19), 7082.
- (158) Chadwick N. P.; Kafizas, A.; Quesada-Cabrera, R.; Sotelo-Vazquez, C.; Bawaked, S. M.; Mokhtar, M.; Al Thabaiti, S. A.; Obaid, A. Y.; Basahel, S. N.; Durrant, J. R. ; Carmalt, C. J and Parkin. I. P. *ACS Catalysis*, **2017**, 7, 1485-1490
- (159) Wu, T. T.; Xie, Y. P.; Yin, L. C.; Liu, G.; Cheng, H. M. Switching Photocatalytic H₂ and O₂ Generation Preferences of Rutile TiO₂ Microspheres with Dominant Reactive Facets by Boron Doping. *J. Phys. Chem. C* **2015**, 119 (1), 84–89.
- (160) Quesada-Gonzalez, M.; Williamson, B. A. D.; Sotelo-Vazquez, C.; Kafizas, A.; Boscher, N. D.; Quesada-Cabrera, R.; Scanlon, D. O.; Carmalt, C. J.; Parkin, I. P. Deeper Understanding of Interstitial Boron-Doped Anatase Thin Films as A Multifunctional Layer Through Theory and Experiment. *J. Phys. Chem. C* **2017**, acs.jpcc.7b11142.

-
- (161) Moisan, M.; Zakrzewski, Z.; Pantel, R. The Theory and Characteristics of an Efficient Surface Wave Launcher (Surfatron) Producing Long Plasma Columns. *J. Phys. D. Appl. Phys.* **1979**, *12*, 219–237.
- (162) Dytrych, P.; Kluson, P.; Solcova, O.; Kment, S.; Stranak, V.; Cada, M.; Hubicka, Z. Shape Selective Photoinduced Electrochemical Behavior of Thin ZnO Layers Prepared by Surfatron. *Thin Solid Films* **2015**, *597*, 131–139.
- (163) Luttrell, T.; Halpegamage, S.; Tao, J.; Kramer, A.; Sutter, E.; Batzill, M. Why Is Anatase a Better Photocatalyst than Rutile - Model Studies on Epitaxial TiO₂ Films. *Sci. Rep.* **2015**, *4* (1), 4043.
- (164) Pottier, A.; Cassaignon, S.; Chanéac, C.; Villain, F.; Tronc, E.; Jolivet, J.-P. Size Tailoring of TiO₂ Anatase Nanoparticles in Aqueous Medium and Synthesis of Nanocomposites. Characterization by Raman Spectroscopy. *J. Mater. Chem.* **2003**, *13*, 877–882.
- (165) Massines, F.; Sarra-Bournet, C.; Fanelli, F.; Naudé, N.; Gherardi, N. Atmospheric Pressure Low Temperature Direct Plasma Technology: Status and Challenges for Thin Film Deposition. *Plasma Process. Polym.* **2012**, *9*, 1041–1073.